

New Bound to the Probability of ^{76}Ge $\beta\beta$ Decay to the 0_1^+ ^{76}Se Level

S. I. Vasil'ev, A. A. Klimenko*, S. B. Osetrov, and A. A. Smol'nikov

Institute for Nuclear Research, Russian Academy of Sciences, pr. Shestidesyatiletiya Oktyabrya 7a, Moscow, 117312 Russia

Joint Institute for Nuclear Research, Dubna, Moscow region, 141980 Russia

*e-mail: klimenko@nusun.jinr.ru

Received July 31, 2000

Measurements were carried out at the underground low-background laboratory of the Baksan Neutrino Observatory using a detection system involving four ultrapure germanium detectors made from enriched ^{76}Ge . The sensitivity of the experiment to the detection of a ^{76}Ge double beta decay to the excited levels of the ^{76}Se nucleus was determined. As a result of 228-day measurements, the new bound to the time of ^{76}Ge half-decay to the ^{76}Se 0_1^+ excited level is found to be $T_{1/2}(2\nu 2\beta) \geq 6.2 \times 10^{21}$ years (90% confidence level). © 2000 MAIK “Nauka/Interperiodica”.

PACS numbers: 23.40.-s

Neutrinoless double beta decay ($0\nu\beta\beta$) is a unique process for studying the fundamental properties of neutrinos. Observation of this process would give new insight into elementary particle physics beyond the standard model of electroweak interactions [1]. Very important additional information necessary for the calculation of the nuclear matrix elements for both two-neutrino and neutrinoless double beta decays [2, 3] can be gained from a search for, and analysis of, a two-neutrino mode in double beta decay ($2\nu 2\beta$), which is allowed within the framework of the standard model of electroweak interactions. Among the possible modes of two-neutrino double beta decay there is a decay to the excited 0_1^+ level of a daughter nucleus. The search for $\beta\beta$ decay to the ground state of the daughter nucleus was preferred in the preceding experiments, because the probability W of two-neutrino double beta decay strongly depends on the total transition energy Q ($W \sim Q^{11}$). The experimental study of double beta decay to the excited level of the daughter nucleus became possible only recently, when the sensitivity of the measurements was enhanced substantially. The experimental search for the double beta decay of ^{76}Ge using a system of four HPGe detectors is being carried out at the underground low-background laboratory of the Baksan Neutrino Observatory (BNO), Institute for Nuclear Research, Russian Academy of Sciences, within the framework of IGEX collaboration [4]. The laboratory is situated at a depth of 660 m of water equivalent. Passive and active shields are used for lowering the detector background. The detectors are surrounded by a common shield consisted of a 12-cm copper layer, a

20-cm lead layer, and an 8-cm layer of borinated polyethylene. All passive shield materials have been kept at the underground laboratory for more than 20 years, and, thus, the concentration of cosmogenic radioactive isotopes inside them has been reduced significantly. The setup operates in a low-background measuring chamber made from a 50-cm layer of a low-background concrete, a 50-cm layer of a low-radioactivity basic rock, and an 8-mm layer of steel. In sum, this reduces the detector background by a factor of ≈ 107 compared to the unshielded detectors at the same depth. The detailed description of the low-background chamber and the detecting setup is given in [5, 6]. The total mass of each of the four detectors is ≈ 1 kg. Three are made of germanium isotopically enriched with ^{76}Ge , and the fourth is made of nonenriched germanium. The layout of detectors inside the passive shield in our experiment differs substantially from those in other long-term experiments on the search for, and study of, the ^{76}Ge double beta decay [7, 8]. In these experiments, each germanium detector is surrounded by an individual passive lead shield, in addition to the common passive shield. Hence, the detectors are screened from each other by several centimeters of lead. Such additional shielding markedly reduces the efficiency of the multidetector setup in detecting the double beta decay modes with transition to the excited levels of the daughter nucleus. The background level achieved in our experiment allows one to operate without an individual shield for each detector, making possible the use of the described multidetector system in the search for the $^{76}\text{Ge}(2\nu 2\beta)^{76}\text{Se}(0_1^+)$ process. The corresponding decay

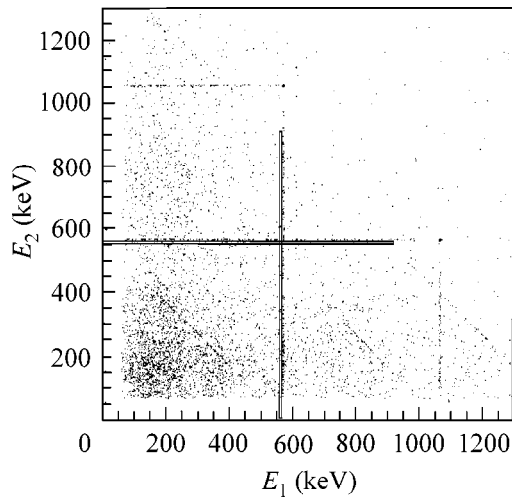


Fig. 1. Experimental two-dimensional distribution of energy release accumulated for the pairs of germanium detectors over 228 days. The domains of maximum signal/background ratio are set off by rectangles.

scheme is given below in Fig. 2. It is seen that the transition to the excited 0_1^+ level of the ^{76}Se nucleus is followed by de-excitation through the sequential emission of two gamma quanta with energies 563.2 and 559.1 keV. Thus, the observation of the two gamma quanta in the final state is a specific signature of the events of the desired process, resulting in additional appreciable lowering of the background. The detector in which the ^{76}Ge double beta decay occurs detects electrons with the total kinetic energy in the range 60–916 keV, while any of the other three detectors can simultaneously detect one or two gamma quanta. The energy resolution averaged over the detectors and the accumulation time was 3.7 keV for energy 1064 keV. The data accumulated over 228 days of “live” time were used in searching for the events with the above signature. To reconstruct the events, the amplitude and temporal information were recorded for each germanium detector. Two events were considered simultaneous and put into a two-dimensional matrix if the time interval between the operations of any two germanium detectors did not exceed 20 μs . The rate of such events was ≈ 25 events per day over the entire energy range measured (from 60 to 4096 keV). A two-dimensional energy distribution of such events accumulated over 228 days is presented in Fig. 1. The domains optimum for searching for the events corresponding to the $^{76}\text{Ge}(2\nu 2\beta)^{76}\text{Se}(0_1^+)$ process are also shown in Fig. 1. These domains cover the energy intervals (556–565) keV \times (60–916) keV along the $X(E_1)$ and $Y(E_2)$ axes, respectively. The “lines of events” observed in the two-dimensional experimental spectrum at energies 570 and 1064 keV perpendicular to the axes are due to the cascade gamma quanta caused by the presence of the ^{207}Bi isotope in the shielding material. A “diagonal

of events” corresponding to the gamma quantum energy 1460 keV due to ^{40}K is also seen in the spectrum.

At the first step of the experiment, special measurement runs were performed without shielding the detectors, with the aim of determining the active detector volume [9] and the detection efficiency for gamma quanta from pointlike calibration sources variously arranged between the detectors. These measurements and the calculations of the detector response functions showed that the active volume of the nonenriched detector corresponds to a mass of 990 g, whereas the volumes of the ^{76}Ge -enriched detectors correspond to masses of 700, 700, and 670 g. The natural abundance of the ^{76}Ge isotope is 7.8%, and the detector material was enriched to 87%. The GEANT 3.21 package was used to develop the program for calculating the detector response functions to different modes of double beta decay. A comparison of the calculated energy spectra with the calibration spectra measured at the first step for different isotopes showed a good reproducibility of the experimental spectra. The calculated two-dimensional distribution of events corresponding to the $^{76}\text{Ge}(2\nu 2\beta)^{76}\text{Se}(0_1^+)$ process in the detection system used is shown in Fig. 2. The domains with maximum signal/background ratios were determined by comparing the experimental and the calculated two-dimensional distributions; they are shown as rectangles in Fig. 1. In these domains, the detection efficiency for the events corresponding to the $^{76}\text{Ge}(2\nu 2\beta)^{76}\text{Se}(0_1^+)$ process was 1.7%. The counting rate for the events in the domains of interest was 0.32 ± 0.04 day $^{-1}$. Inasmuch as no statistically significant increase in the counting rate was observed for the desired events in these domains, one can only determine a new bound to the half-decay time of the process. The limit to the half-decay time is calculated by the formula

$$\lim T_{1/2} = \ln(2)N_0 t \epsilon / N_b^{1/2},$$

where N_0 is the number of ^{76}Ge nuclei, t is the measurement time, ϵ is the detection efficiency, and N_b is the number of counts in the energy range studied. Making use of the background counting rate in the indicated domains and the calculated detection efficiency, one obtains the following lower bound to the half-decay time for ^{76}Ge decay to the 0_1^+ level of the ^{76}Se nucleons:

$$T_{1/2}(2\nu 2\beta, 0_1^+) \geq 6.2 \times 10^{21} \text{ years} \\ (90\% \text{ confidence level}).$$

The best value attained to date was obtained in [10]:

$$T_{1/2}(2\nu 2\beta, 0_1^+) \geq 1.7 \times 10^{21} \text{ years} \\ (90\% \text{ confidence level}).$$

At the first step of the measurements, the prospects for further enhancement of the sensitivity through lower-

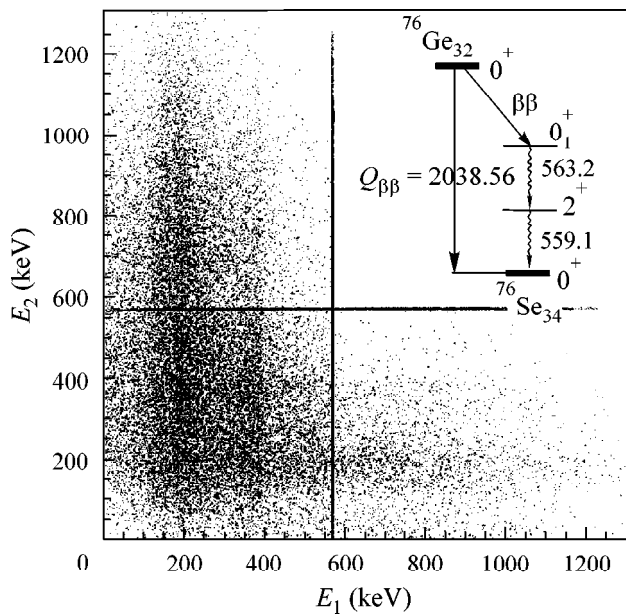


Fig. 2. Calculated two-dimensional distribution as a function of the response of the detecting setup to the $^{76}\text{Ge}(2\nu 2\beta)^{76}\text{Se}(0_1^+)$ process. Scheme of $\beta\beta$ decay for the ^{76}Ge isotope.

ing of the background were outlined. The main background components were found to be caused by the presence of the ^{207}Bi and ^{40}K isotopes in the materials of the setup. The analysis of the relative intensities of the ^{207}Bi and ^{40}K gamma peaks for each of the detectors enabled one to determine their locations in the setup rather accurately. This furnishes an opportunity to com-

pletely eliminate the ^{207}Bi isotope and remove a considerable part of the ^{40}K isotope from the components of detectors and shield.

This work was supported in part by the Russian Foundation for Basic Research, project no. 98-02-17973.

REFERENCES

1. M. Moe and P. Vogel, *Annu. Rev. Part. Sci.* **44**, 247 (1994).
2. H. V. Klapdor-Kleingrothaus and A. Staudt, *Non-Accelerator Particle Physics* (Institute of Physics Publ., Bristol, 1995).
3. J. Suhonen and O. Civaterese, *Phys. Rep.* **300**, 123 (1998).
4. A. A. Klimenko, S. B. Osetrov, A. A. Smolnikov, *et al.*, in *Proceedings of the International School "Particle and Cosmology"* (World Scientific, Singapore, 1996), p. 108.
5. A. A. Klimenko, A. A. Pomansky, and A. A. Smolnikov, *Nucl. Instrum. Methods Phys. Res. B* **17**, 445 (1996).
6. A. A. Klimenko, S. B. Osetrov, A. A. Smolnikov, and S. I. Vasiliev, *Pis'ma Zh. Éksp. Teor. Fiz.* **67**, 835 (1998) [*JETP Lett.* **67**, 875 (1998)].
7. M. Gunter, J. Hellmig, G. Heusser, *et al.*, *Phys. Rev. D* **55**, 54 (1997).
8. C. E. Aalseth, F. T. Avignone, A. Klimenko, *et al.*, *Phys. Rev. C* **59**, 2108 (1999).
9. E. V. Demidova, I. V. Kirpichnikov, and A. A. Vasenko, *Nucl. Phys. B* **70**, 252 (1999).
10. A. S. Barabash, A. V. Derbin, L. A. Popeko, and V. I. Umatov, *Z. Phys.* **252**, 231 (1995).

Translated by I. Roizen

Study of the ρ , ω , $\phi \rightarrow \eta\gamma \rightarrow 7\gamma$ Decays with an SND Detector on a VEPP-2M Collider

M. N. Achasov, S. E. Baru, K. I. Beloborodov, A. V. Berdyugin, A. V. Bozhenok,
A. G. Bogdanchikov, D. A. Bukin, S. V. Burdin, A. V. Vasil'ev, Yu. S. Velikzhanin,
T. V. Dimova, V. P. Druzhinin, M. S. Dubrovin, D. I. Ganyushin, I. A. Gaponenko,
V. B. Golubev, V. N. Ivanchenko, I. A. Koop, A. A. Korol', S. V. Koshuba,
G. A. Kukartsev, E. V. Pakhtusova, A. A. Sal'nikov, S. I. Serebnyakov, V. V. Sharyi,
Yu. M. Shatunov, V. A. Sidorov, and Z. K. Silagadze

*Budker Institute of Nuclear Physics, Siberian Division, Russian Academy of Sciences,
pr. Akademika Lavrent'eva 11, Novosibirsk, 630090 Russia*

Received August 15, 2000

The $e^+e^- \rightarrow \eta\gamma \rightarrow 7\gamma$ process was studied in the energy range $2E = 600\text{--}1060$ MeV with an SND detector on a VEPP-2M e^+e^- collider. The decay branching ratios $B(\phi \rightarrow \eta\gamma) = (1.353 \pm 0.011 \pm 0.052) \times 10^{-2}$, $B(\omega \rightarrow \eta\gamma) = (4.62 \pm 0.71 \pm 0.18) \times 10^{-4}$, and $B(\rho \rightarrow \eta\gamma) = (2.73 \pm 0.31 \pm 0.15) \times 10^{-4}$ were measured.
© 2000 MAIK "Nauka/Interperiodica".

PACS numbers: 13.25.Cq; 14.40.Aq; 13.65.+i

Radiative decays of light vector mesons— ρ , ω , and ϕ —are important for understanding the behavior of the strong interaction at low energies. Although many measurements were carried out for the probabilities of the radiative decays, the achieved accuracy [1] is insufficient for reliable determination of the parameters of phenomenological models [2–4].

We report the results of investigations of the $e^+e^- \rightarrow \eta\gamma$ process followed by the $\eta \rightarrow 3\pi^0 \rightarrow 6\gamma$ decay. Since the final state includes seven photons, the background can be substantially suppressed compared to that in other channels of η -meson decay and, therefore, the systematic error may be reduced.

The experiment [5] was carried out in 1998 at the VEPP-2M e^+e^- collider with the SND detector [6]. Two scans were performed in the energy range $2E_0 = 984\text{--}1060$ MeV (PHI-98 experiment) with an integral luminosity of 8.0 pb^{-1} at 16 energy points and with about 10^7 produced ϕ mesons. In addition, a scan (OME-98 experiment) over 38 points in the energy range $2E_0 = 360\text{--}970$ MeV was carried out with an integral luminosity of 3.5 pb^{-1} and with about 3×10^6 produced ρ and ω mesons.

The events of the process

$$e^+e^- \rightarrow \eta\gamma, \quad \eta \rightarrow 3\pi^0, \quad \pi^0 \rightarrow 2\gamma \quad (1)$$

are characterized by the final state with seven photons, a few of which may not be detected. The extra photons may also appear due to the splitting of a shower in the calorimeter, the emission of the photons by the initial particles at large angles, or the superposition of the

beam background. The main background process in the ϕ -resonance region is the $\phi \rightarrow K_S K_L$ decay, where K_S decays into two neutral pions and K_L , interacting in the calorimeter, produces extra "photons." An additional background is formed by the $e^+e^- \rightarrow \omega\pi^0 + X$ process followed by the $\omega \rightarrow \pi^0\gamma$ decay, where X are extra photons. An analysis of the experimental data has demonstrated that the QED process $e^+e^- \rightarrow 3\gamma$, being superposed with other events, may also result in the required event configuration.

Taking the above-listed background events into account, we selected events in two steps. At the first step, among the events in which six or more photons and no charged particles were detected, we selected those satisfying the following conditions imposed on a total energy release E_{tot} in the calorimeter and the total momentum P_{tot} of photons:

$$E_{tot}/2E_0 < 1.2, \quad P_{tot}/2E_0 < 0.2/c,$$

$$E_{tot}/2E_0 - cP_{tot}/2 > 0.7.$$

For the selected events, we performed a kinematic reconstruction using the measured angles, the energies of the photons, and energy–momentum conservation. As a result, the energies of the photons were determined more accurately and the χ^2 values specifying the degree of certainty of a process were determined:

χ^2 for the assumption of the $e^+e^- \rightarrow n\gamma$ process with $n \geq 6$ or 7;

$\chi_{3\gamma}^2$ for the assumption of the $e^+e^- \rightarrow 2(3)\gamma + X$ process;

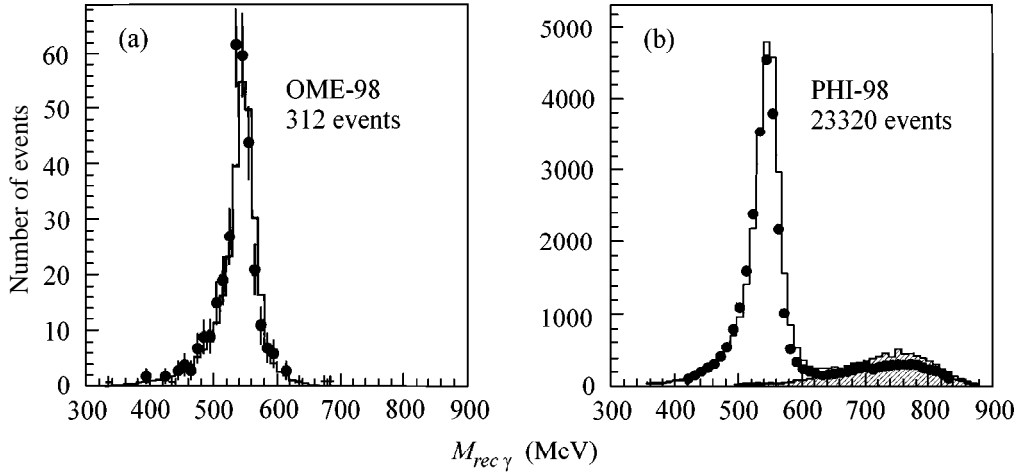


Fig. 1. Recoil mass distribution for the photon with the highest energy in an event. The points are the experimental data, and the histograms are the simulation: (a) OME-98 experiment (312 events) and (b) PHI-98 experiment (23320 events). The shaded histogram is the sum of the simulation of background processes, which reduces to process (2).

$\chi_{\omega\pi^0}^2$ for the assumption of the $e^+e^- \rightarrow \omega\pi^0 + X$ process.

Further selection was carried out with the restrictions

$$\chi^2 < 30, \quad \chi_{3\gamma}^2 > 20, \quad \chi_{\omega\pi^0}^2 > 20.$$

Figure 1 shows the distributions of the selected events in the recoil mass $M_{rec\gamma}$ of the highest energy photon. It is seen that the desired process prevails in all scans. The events with $M_{rec\gamma} > 600$ MeV in Fig. 1b are determined by the process

$$e^+e^- \rightarrow \phi \rightarrow K_S K_L. \quad (2)$$

Finally, we select the events satisfying the condition $400 < M_{rec\gamma} < 600$ MeV.

The number $N(s)$ of the observed events at a given energy is described by the formula

$$N(s) = L(s)[\epsilon(s)\beta(s)\sigma(s) + \sigma_b(s)], \quad s = 4E_0^2, \quad (3)$$

where $L(s)$ is the integral luminosity, ϵ is the detection efficiency determined by a simulation, β is the factor representing the radiative corrections, σ_b is the cross section for background processes, and σ is the cross section for the desired process (1).

When determining the background from process (2), inaccuracy in the simulation of the interaction of the K_L meson with a substance in the calorimeter is possible. Figure 1b demonstrates that the contribution of process (2) dominates for $M_{rec\gamma} > 600$ MeV, while the contribution of the desired process (1) is negligible. For this reason, the number of events of process (2) in the range $400 < M_{rec\gamma} < 600$ MeV was determined from the number of experimental events in the interval $600 < M_{rec\gamma} < 800$ MeV by taking into account the simulated

ratio of the numbers of the $K_S K_L$ events that fall into the mass ranges $400 < M_{rec\gamma} < 600$ MeV and $600 < M_{rec\gamma} < 800$ MeV.

The energy dependence of the resulting cross section (Fig. 2) was parametrized by the vector-dominance formulas [7] including the contributions of the $\rho, \omega,$ and ϕ resonances:

$$\sigma(s) = \frac{F(s)}{s^{3/2}} \left| \sum_{V=\rho, \omega, \phi} \sqrt{12\pi \prod_{B_{VP}} \frac{m_V^3 \Gamma_V e^{i\phi_V}}{F(m_V^2) D_V(s)}} \right|^2, \quad (4)$$

where $F(s) = [(s - m_\eta^2)/2\sqrt{s}]^3$, $D(s) = m_V^2 - s - i\sqrt{s}\Gamma_V(s)$, and the products

$$\prod_{B_{VP}} = Br_{V \rightarrow e^+e^-} Br_{V \rightarrow \eta\gamma} Br_{\eta \rightarrow 3\pi^0} Br_{\pi^0 \rightarrow 2\gamma}$$

are the free parameters of the approximations. The relative phase shifts of the resonances were fixed at $\phi_\rho = \phi_\omega = 0, \phi_\phi = \pi$. The approximation gives the following results:

$$\begin{aligned} & Br_{\phi \rightarrow e^+e^-} Br_{\phi \rightarrow \eta\gamma} Br_{\eta \rightarrow 3\pi^0} \\ &= (1.249 \pm 0.011 \pm 0.035) \times 10^{-6}, \\ & Br_{\omega \rightarrow e^+e^-} Br_{\omega \rightarrow \eta\gamma} Br_{\eta \rightarrow 3\pi^0} \\ &= (1.01 \pm 0.16 \pm 0.03) \times 10^{-8}, \\ & Br_{\rho \rightarrow e^+e^-} Br_{\rho \rightarrow \eta\gamma} Br_{\eta \rightarrow 3\pi^0} \\ &= (3.77 \pm 0.45 \pm 0.11) \times 10^{-9}, \end{aligned} \quad (5)$$

where the first error is statistical and the second, systematic, error is due to the contributions of errors in the

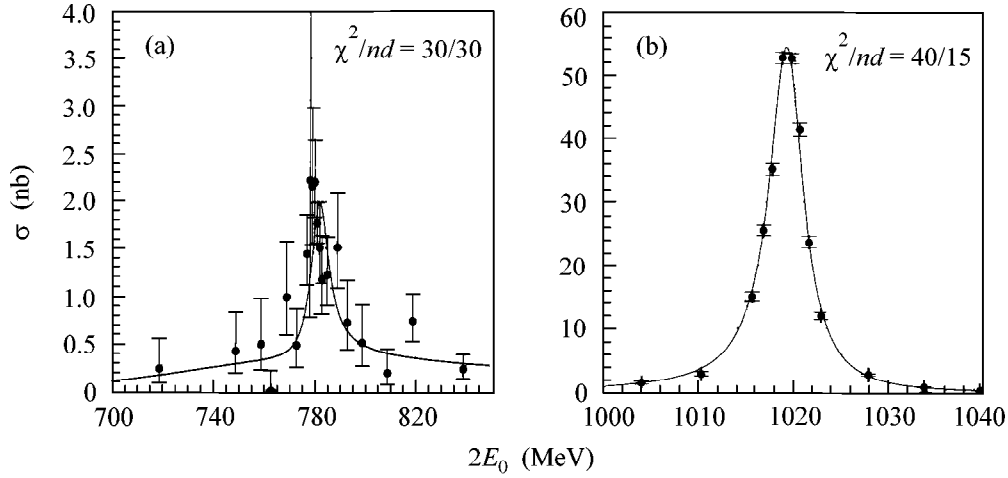


Fig. 2. Measured total cross section for the $e^+e^- \rightarrow \eta\gamma$ process in the region of (a) ρ and ω mesons ($\chi^2/nd = 30/30$) and (b) ϕ mesons ($\chi^2/nd = 40/15$).

determination of the detection efficiency and the error in the measurement of the luminosity. The luminosity was measured from elastic electron–positron scattering at large angles and from the process of two-quantum annihilation. The difference in the results of the two methods does not exceed 1%. The accuracy of the theoretical formulas used for the simulation of elastic scattering and experimental conditions provides an estimate of about 2% for the accuracy of the luminosity in the case under consideration. In order to estimate the systematic errors in the detection efficiency, the stability of the results to a change in the selection conditions was examined: we added restrictions on the polar angle of the photons and on the number ($N_\gamma = 7$) of particles and used only the completely reconstructed $e^+e^- \rightarrow \eta\gamma \rightarrow 7\gamma$ events. As was discussed above, due to the emission of the initial particles at large angles and superposition of preceding events, extra spurious photons appear in the SND calorimeter. For this reason, one of the tests of the kinematic reconstruction was carried out with the exclusion of photons with energies lower than 50 MeV and with a polar angle less than 36° . In addition, two scans of the ϕ meson were independently processed. All tests demonstrated the stability of the results, and the total systematic error in the efficiency, with the inclusion of all effects, was estimated at 2%. This estimate is treated as independent of the systematic error in luminosity.

Using the tabular values of $Br_{V \rightarrow e^+e^-}$, $Br_{\eta \rightarrow 3\pi^0}$, and $Br_{\pi^0 \rightarrow 2\gamma}$ from [1], we obtain from Eqs. (5) the values

$$Br_{\phi \rightarrow e^+e^-} Br_{\phi \rightarrow \eta\gamma} = (4.049 \pm 0.033 \pm 0.153) \times 10^{-6},$$

$$Br_{\omega \rightarrow e^+e^-} Br_{\omega \rightarrow \eta\gamma} = (3.29 \pm 0.50 \pm 0.12) \times 10^{-8},$$

$$Br_{\rho \rightarrow e^+e^-} Br_{\rho \rightarrow \eta\gamma} = (1.22 \pm 0.14 \pm 0.07) \times 10^{-8},$$

$$Br_{\phi \rightarrow \eta\gamma} = (1.353 \pm 0.011 \pm 0.052) \times 10^{-2},$$

$$Br_{\omega \rightarrow \eta\gamma} = (4.62 \pm 0.71 \pm 0.18) \times 10^{-4}, \quad (6)$$

$$Br_{\rho \rightarrow \eta\gamma} = (2.73 \pm 0.31 \pm 0.15) \times 10^{-4},$$

$$\sigma_{\phi \rightarrow \eta\gamma} = (57.16 \pm 0.46 \pm 1.64) \text{nb},$$

$$\sigma_{\omega \rightarrow \eta\gamma} = (0.79 \pm 0.12 \pm 0.02) \text{nb},$$

$$\sigma_{\rho \rightarrow \eta\gamma} = (0.303 \pm 0.035 \pm 0.009) \text{nb},$$

where $\sigma_{V\eta\gamma} = 12\pi Br_{V \rightarrow e^+e^-} Br_{V \rightarrow \eta\gamma} / m_V^2$ and the errors of the tabular values are included in the systematic errors. Using data (5) obtained above, the results of previous measurements with the SND detector [8, 9], and the data on the widths of the ρ and ω mesons [1], we derive the ratios

$$\frac{B(\eta \rightarrow \pi^+\pi^-\pi^0)}{B(\eta \rightarrow \gamma\gamma) + B(\eta \rightarrow 3\pi^0)} = 0.309 \pm 0.012, \quad (7)$$

$$B(\eta \rightarrow 3\pi^0) / B(\eta \rightarrow \gamma\gamma) = 0.796 \pm 0.026,$$

$$\Gamma_{\rho \rightarrow \eta\gamma} / \Gamma_{\omega \rightarrow \eta\gamma} = 10.6 \pm 2.2.$$

Our results (5)–(7) are in agreement with the data of other experiments [8–12]. The branching ratios for the ϕ , $\omega \rightarrow \eta\gamma$ decays are measured with an accuracy close to the tabular one [1], and the branching ratio for the $\rho \rightarrow \eta\gamma$ decay is determined with the doubly improved accuracy. Note that the quantity $Br_{\phi \rightarrow e^+e^-} Br_{\phi \rightarrow \eta\gamma} Br_{\eta \rightarrow 3\pi^0}$ (5) was measured with noticeably higher accuracy than the branching ratio $Br_{\phi \rightarrow \eta\gamma}$ (6), because the leptonic width of the ϕ meson

is known with an accuracy of 2.7%, which is noticeably worse than the statistical accuracy of our measurement.

This work was supported by the "Russian Universities" Foundation (project no. 3N-339-00) and the Russian Foundation for Basic Research (project nos. 99-02-16813, 00-02-17478, and 00-02-17481).

REFERENCES

1. A. Caso *et al.* (Particle Data Group), Eur. Phys. J. C **3** (1998).
2. P. O'Donnell, Rev. Mod. Phys. **53**, 673 (1981).
3. G. Morpurgo, Phys. Rev. D **42**, 1497 (1990).
4. M. Benayoun *et al.*, Phys. Rev. D **59**, 114027 (1999).
5. M. N. Achasov *et al.*, Preprint No. 98-65, IYaf (Budker Institute of Nuclear Physics, Novosibirsk, 1998).
6. M. N. Achasov *et al.*, Nucl. Instrum. Methods Phys. Res. A **449**, 125 (2000).
7. N. N. Achasov *et al.*, J. Mod. Phys. A **7**, 3187 (1992).
8. N. N. Achasov *et al.*, Eur. Phys. J. C **12**, 25 (2000).
9. N. N. Achasov, K. I. Beloborodov, A. V. Berdyugin, *et al.*, Zh. Éksp. Teor. Fiz. **117**, 22 (2000) [JETP **90**, 17 (2000)].
10. M. N. Achasov *et al.*, Pis'ma Zh. Éksp. Teor. Fiz. **68**, 599 (1998) [JETP Lett. **68**, 573 (1998)].
11. R. R. Akhmetshin *et al.*, Phys. Lett. B **460**, 242 (1999); hep-ex/9907003.
12. T. Case *et al.*, Phys. Rev. D **61**, 32002 (2000).

Translated by R. Tyapaev

Triple Correlation in the $^{10}\text{B}(n, \alpha\gamma)^7\text{Li}$ Reaction

A. M. Gagarski, G. V. Val'ski, G. A. Petrov, Yu. E. Loginov, V. E. Bunakov, I. S. Guseva*,
V. I. Petrova, and T. A. Zavarukhina

St. Petersburg Nuclear Physics Institute, Russian Academy of Sciences, Gatchina, St. Petersburg, 188350 Russia

* e-mail: guseva@hep486.pnpi.spb.ru

Received August 22, 2000

The formally T -odd triple correlation between the directions of the momenta of α particle and γ quantum and the polarization pseudovector of a thermal neutron was examined for the $^{10}\text{B} + n = ^7\text{Li} + ^4\text{He} + \gamma$ reaction. Such T -odd correlations can be directly used for checking time reversal invariance in the elastic scattering of particles. In more complex reactions, this correlation can occur as a result of particle interactions in the entrance and exit channels of the reaction and, being a background effect, requires correct theoretical or direct experimental estimation. Our experiments gave an upper limit of 3.2×10^{-4} (90% confidence level) for the possible T -odd asymmetry parameter in the reaction under study. © 2000 MAIK "Nauka/Interperiodica".

PACS numbers: 24.80.+y; 25.40.Fq; 24.70.+s; 11.30.Er

In a recent investigation of the correlation between the directions of the momenta of fission fragments and long-range α particles and the longitudinal polarization of cold neutrons inducing triple fission of ^{235}U [1], a surprisingly large value was found for the average asymmetry parameter $\langle D \rangle$ in the correlation

$$W(\theta, \varphi) = 1 + \langle D \rangle \boldsymbol{\sigma}_n \cdot [\mathbf{P}_\alpha \times \mathbf{P}_f], \quad (1)$$
$$\langle D \rangle = (2.35 \pm 0.05) \times 10^{-3},$$

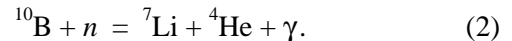
where \mathbf{P}_f , \mathbf{P}_α , and $\boldsymbol{\sigma}_n$ are the unit vectors in the respective directions.

The original idea of such investigations [2, 3] was to improve the upper limit on the possible violation of time reversal invariance by using the fact that the correlation (1) formally changes its sign with time reversal. However, a closer analysis [4] indicates that T -odd correlations may be directly used for testing T invariance only in elastic scattering. The nonzero T -odd correlation in inelastic processes can be associated with T -noninvariance only if the amplitudes of these processes can be calculated in the first Born approximation. However, even in this case the inclusion of the next orders of perturbation theory, (i.e., interactions in the initial and final states) may lead to effects simulating T noninvariance. For this reason, the asymmetry effect observed in [1] is likely caused by the triple fission mechanism and is not directly related to the possible violation of T invariance. Nevertheless, further investigation of the effect observed in [1] is of considerable interest from at least two points of view: first, the determination of a mechanism responsible for correlation (1) in triple fission may provide important information on the dynamics of this reaction, and, second, the study of the mechanisms of various T -odd correlations masking the effects of possible violation of time reversal invariance in nuclear

reactions may be useful if there is a need to introduce corrections.

Because of the complexity of the fission reaction, the correct calculation of these corrections is hardly probable even with a full understanding of the mechanism responsible for T -odd correlation (1). For this reason, it is worthwhile to find and examine such correlations in simpler reactions, which, as may be hoped, admit correct theoretical treatment.

In this work, an attempt is made to reveal and analyze the formally T -odd correlation in one of the simplest nuclear reaction of neutrons:



Since the first Born approximation can hardly apply even to this simpler (compared to fission) nuclear reaction, theoretically, one can expect the appearance of the T -odd correlation in this reaction as well.

After the absorption of a thermal polarized neutron, the ^{11}B nucleus becomes polarized along or opposite the neutron spin for two possible values of the total angular momentum $J = (I + 1/2) = 7/2$ or $J = (I - 1/2) = 5/2$, respectively. For 100% polarization of thermal neutrons, the ^{11}B nucleus turns out to be polarized by 50%. The most probable energy of an α particle is about 1.4 MeV, and the energy of an $M1$ gamma quantum with a lifetime of 7.7×10^{-14} s is 480 keV. The well-known neutron ^{11}B resonances closest to the thermal point have the following characteristics: -947 keV ($J = 7/2^+$, $l = 0$); 170.3 keV ($J = 5/2^+$, $l = 0$); 370 keV ($J = 7/2^+$, $l = 0$); and 530 keV ($J = 5/2^-$, $l = 1$). An attempt at revealing parity violation in this reaction was

made in [5]. The resulting P -odd asymmetry parameter for α -particle emission was found to be very small:

$$\alpha_{n\alpha} = -(1.5 \pm 1.0) \times 10^{-6}.$$

At the same time, the parameter of left–right asymmetry

$$W(\theta, \varphi) = 1 + \alpha_{lr} \boldsymbol{\sigma}_n \cdot [\mathbf{P}_n \times \mathbf{P}_\alpha], \quad (3)$$

which arises due to p -wave mixing in neutron capture by ^{10}B , turned out to be $\alpha_{lr} = (0.77 \pm 0.06) \times 10^{-4}$ [6]. In concluding a brief sketch of the characteristics of reaction (2), it should be emphasized that there is a pronounced cluster nuclear structure at the input and output.

In this work, a T -odd correlation of the following form was studied:

$$W(\theta, \varphi) = 1 + D_{\alpha\gamma} \boldsymbol{\sigma}_n \cdot [\mathbf{P}_\alpha \times \mathbf{P}_\gamma]. \quad (4)$$

In the experiment, gamma quanta and α particles were detected by two scintillation spectrometers with NaI(Tl) crystals and two surface barrier silicon detectors, respectively. The directions of the longitudinally polarized ($\sim 90\%$) beam of thermal neutrons and the symmetry axes of the detectors of α particles and gamma quanta were mutually orthogonal. The use of four spectrometric radiation detectors in the orthogonal geometry ensured the optimum conditions for measuring the $D_{\alpha\gamma}$ coefficient and correctly taking into account the possible effects of instrumental asymmetry. Experimental values of asymmetry parameters were calculated by the simple expression

$$D_{\text{exp}}(i, k) = [N^\uparrow(i, k) - N^\downarrow(i, k)] / [N^\uparrow(i, k) + N^\downarrow(i, k)], \quad (5)$$

where $N^{\uparrow\downarrow}(i, k)$ is the counting rate of α - γ coincidence in the (i, k) detectors for the two mutually opposite directions of the longitudinal polarization of the thermal neutrons inducing reaction (2). The resulting experimental values of the parameters were averaged taking the sign correlation into account, so that the same experimental quantities $D_{\text{exp}}(i, k)$ could be used for obtaining the average values of the T -odd asymmetry parameter and for estimating the possible instrumental asymmetry. In most measurement runs, instrumental asymmetry was not observed within the statistical accuracy.

The first results of the experiments with a polarized beam ($\langle \lambda_n \rangle \sim 2 \text{ \AA}$, $\Phi_n \sim 5 \times 10^6 \text{ n/cm}^2 \text{ s}$) from the WWR-M reactor at the St. Petersburg Nuclear Physics Institute, Russian Academy of Sciences, were reported in [7]. After completing the measurements and introducing all necessary corrections, no statistically significant value was found for the T -odd asymmetry parameter (4):

$$D_{\alpha\gamma} = -(0.09 \pm 1.9) \times 10^{-4}.$$

At a 90% confidence level, the possible value of the $D_{\alpha\gamma}$ parameter does not exceed 3.2×10^{-4} . This value is approximately one-tenth of that observed for triple fission of the ^{233}U nucleus [1] and is the lowest up-to-date experimental limit to the possible magnitude of T -odd asymmetry in nuclear reactions with neutrons.

In principle, this result is not surprising because of the radical distinctions in the mechanisms of the reactions under investigation. Below are listed some of the distinctions that are most substantial for discussion.

First, in this work we examine the correlation between the directions of divergence of a charged particle and a gamma quantum, as distinct from triple fission, where the same correlation was analyzed for two charged particles.

Second, according to the modern concepts, excited massive fragments and long-range α particles are produced in a triple fission near the scission point of the fissioning nucleus (in 10^{-23} – 10^{-20} s), whereas the gamma quanta in the $^{10}\text{B}(n, \alpha\gamma)^7\text{Li}$ reaction are emitted in $\sim 8 \times 10^{-14}$ s.

Third, due to the focusing of two divergent fragments in a Coulomb field (final-state interaction), the α particle in the triple decay mostly escapes near the equatorial plane, while the angular α - γ correlation in reaction (2) is less pronounced.

Fourth, in contrast to reaction (2), the fission is characterized by a wealth of (up to 10^{10}) final states with widely diversified properties.

If the T -odd asymmetry in triple fission arises due to the Coulomb interaction, the first and second items concerning the distinctions in the correlations of interest will be highly important. Therefore, a search for the T -odd correlations in a fission involving a neutron or gamma quantum as a third particle is of considerable interest. The relevant experiments were proposed in our work [7] and are now underway.

On the whole, an analysis of the presently available information leads one to the general assumption that the large T -odd asymmetry observed in [1] is caused by the complicated character of the fission reaction and its pronounced collective nature [8]. To corroborate this conclusion, the T -odd asymmetry in the escape of light particles in triple fission [7, 8] should be further investigated in detail and the T -odd correlations in the simplest neutron reactions should be examined with higher accuracy.

In conclusion, we are deeply grateful to V.P. Plakhtii and his collaborators, who allowed us to work with the beam of polarized neutrons from the WWR-M reactor; to B.G. Peskov for preparation of the thin ^{10}B targets; and to N.P. Afanas'eva for manufacture of the semiconductor detectors of charged particles.

This work was supported by the Russian Foundation for Basic Research (project no. 99-02-17275) and the INTAS (grant no. 99-00229).

REFERENCES

1. P. Jesinger, A. Kotzle, A. M. Gagarski, *et al.*, in *Proceedings of the International Workshop "Nuclear Fission and Fission Product Spectroscopy," Seyssins, France, 1998*, AIP Conf. Proc. **447**, 395 (1998).
2. Schreckenbach *et al.*, in *Proceedings of the Second International Workshop on Time Reversal Invariance and Parity Violation in Neutron Reactions, Dubna, 1993* (World Scientific, Singapore, 1994), p. 187.
3. G. V. Danilyan, ILL Proposal 3-07-76 (Grenoble, France, 1996).
4. R. M. Ryndin, in *Proceedings of the III Winter School of the Physicotechnical Institute on Theory of Nuclei and Physics of High Energy, Leningrad, 1968*, Part 2, p. 39; E. M. Henley and B. A. Jacobsohn, Phys. Rev. Lett. **16**, 716 (1966); V. Bunakov and L. Pikelner, Prog. Part. Nucl. Phys. **39**, 337 (1997).
5. V. A. Vesna, Yu. M. Gledenov, I. S. Okunev, *et al.*, Yad. Fiz. **59**, 23 (1996) [Phys. At. Nucl. **59**, 19 (1996)].
6. N. V. Borovikova, V. A. Vesna, A. I. Egorov, *et al.*, Pis'ma Zh. Éksp. Teor. Fiz. **30**, 527 (1979) [JETP Lett. **30**, 495 (1979)].
7. G. A. Petrov, V. E. Bunakov, A. M. Gagarski, *et al.*, in *Proceedings of the 8th International Seminar on Interaction of Neutrons with Nuclei, ISINN-8, Dubna, 2000*, p. 51; F. Goennenwein, V. E. Bunakov, G. A. Petrov, *et al.*, Project INTAS 99-00229 (2000–2002).
8. V. E. Bunakov and G. A. Petrov, in *Proceedings of the 8th International Seminar on Interaction of Neutrons with Nuclei, ISINN-8, Dubna, 2000*, p. 53.

Translated by R. Tyapaev

Atomic Recoil Effects in Slow Light Propagation¹

I. Carusotto^{1,4}, M. Artoni², and G. C. La Rocca^{3,4}

¹ Scuola Normale Superiore, 56126 Pisa, Italy

e-mail: Iacopo.Carusotto@sns.it

² INFN, European Laboratory for Non-linear Spectroscopy, 50125 Florence, Italy

³ Dipartimento di Fisica, Università di Salerno, 84081 Baronissi (Sa), Italy

⁴ INFN, Scuola Normale Superiore, 56126 Pisa, Italy

Received July 17, 2000; in final form, August 21, 2000

We theoretically investigate the effect of atomic recoil on the propagation of ultraslow light pulses through a coherently driven Bose–Einstein condensed gas. For a sample at rest, the group velocity of the light pulse is the sum of the group velocity that one would observe in the absence of mechanical effects (infinite mass limit) and the velocity of the recoiling atoms (light-dragging effect). We predict that atomic recoil may give rise to a lower bound for the observable group velocities, as well as to pulse propagation at negative group velocities without appreciable absorption. © 2000 MAIK “Nauka/Interperiodica”.

PACS numbers: 42.50.Vk; 32.80.Qk; 03.75.Fi

Recent experiments [1, 2] have demonstrated a reduction in the group velocity of light down to values as low as 17 m/s in coherently driven atomic samples. This was achieved by tuning the pulse frequency in the electromagnetically induced transparency (EIT) window of an optically dressed three-level atomic gas, where quantum coherence between two lower levels gives rise to a vanishing absorption along with a very steep dispersion [3]. Further improvements to the experimental setup are expected [1] to enable one to reach group velocities as small as the atomic recoil velocity. In this regime, recoil is expected to play an important role in the propagation of the pulse.

In this letter, we provide a detailed derivation of the group velocity of light pulses in a coherently driven Bose–Einstein condensed (BEC) atomic sample [4] when the effect of atomic recoil is taken into account. Apart from the well-known light-dragging effect in uniformly moving dielectrics [5], we show that the group velocity of slow light in a sample at rest under appropriate EIT conditions is given by the group velocity in the infinite mass approximation plus the velocity of the atoms which recoil following the optical process itself. Such a dragging effect imposes a lower bound to the group velocity that can be observed in typical configurations of experimental interest. For a specific level scheme and a geometry in which atoms recoil in the direction opposite to the probe wavevector, light propagation at negative group velocities without appreciable absorption is also possible. Finally, we show that the group velocity of a light pulse is not affected by atom–atom interactions at the mean-field level.

We consider a cloud of BEC atoms [4] in a three-level Λ -type configuration, as shown in Fig. 1. All atoms

are initially in the ground state $|g\rangle$, and the optical transition between the metastable $|m\rangle$ and excited state $|e\rangle$ is dressed by a nearly resonant *coupling* cw laser beam of amplitude $E_c(\mathbf{x})$ and frequency $\omega_c = \omega_e - \omega_m$. A weak *probe* pulse at frequency ω_p nearly resonant with the other optical transition between the ground state $|g\rangle$ and the excited state $|e\rangle$ also propagates through the system. When the decay rate of the metastable level m is much smaller than the decay rate of the level e , the probe field experiences EIT with a narrow absorption dip and a very steep dispersion at frequencies around $\omega_p = \omega_c + \omega_m - \omega_g$ [3]. In a second-quantized formalism, the Hamiltonian of the system can be written as

$$\mathcal{H} = \sum_{i=\{g,e,b\}} \int d^3\mathbf{x} \hat{\psi}_i^\dagger(\mathbf{x}) \left(\hbar\omega_i + V_i(\mathbf{x}) - \frac{\hbar^2}{2m} \nabla^2 \right) \hat{\psi}_i(\mathbf{x}) - (d_p E_p(\mathbf{x}, t) \hat{\psi}_e^\dagger(\mathbf{x}) \hat{\psi}_g(\mathbf{x}) + d_c E_c(\mathbf{x}, t) \hat{\psi}_e^\dagger(\mathbf{x}) \hat{\psi}_m(\mathbf{x}) + \text{h.c.}). \quad (1)$$

The first two terms describe the internal structure of the atoms and their kinetic and potential energy, while the last terms describe the coupling of the two laser beams to the atoms. The effects of the atom–atom interactions will be discussed later. Both the spontaneous emission from the excited state $|e\rangle$ and the decoherence of the two lower $|m\rangle$ and $|g\rangle$ states are responsible for a loss of atoms from the condensate and can, therefore, be modeled by loss terms in the equations of motion for the three-component macroscopic wavefunction Ψ_i of the Bose condensate:

$$i\hbar \frac{\partial}{\partial t} \Psi_g(\mathbf{x}, t) = \left[-\frac{\hbar^2 \nabla^2}{2m} + V_g(\mathbf{x}) + \hbar\omega_g \right] \Psi_g(\mathbf{x}, t) - d_p^* E_p^*(\mathbf{x}, t) \Psi_e(\mathbf{x}, t), \quad (2)$$

¹ This article was submitted by the authors in English.

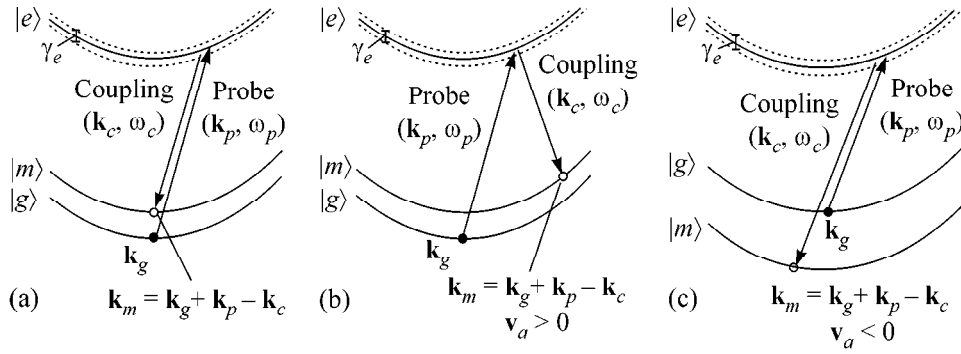


Fig. 1. Level scheme and optical processes for (a) copropagating and (b) counterpropagating probe and coupling beams. (c) Proposed arrangement for obtaining negative group velocities.

$$\begin{aligned}
 i\hbar \frac{\partial}{\partial t} \Psi_e(\mathbf{x}, t) &= \left[-\frac{\hbar^2 \nabla^2}{2m} + V_e(\mathbf{x}) + \hbar(\omega_e - i\gamma_e) \right] \Psi_e(\mathbf{x}, t) \\
 &\quad - d_p E_p(\mathbf{x}, t) \Psi_g(\mathbf{x}, t) - d_c E_c(\mathbf{x}, t) \Psi_m(\mathbf{x}, t), \quad (3) \\
 i\hbar \frac{\partial}{\partial t} \Psi_m(\mathbf{x}, t) &= \left[-\frac{\hbar^2 \nabla^2}{2m} + V_m(\mathbf{x}) + \hbar(\omega_m - i\gamma_m) \right] \Psi_m(\mathbf{x}, t) \\
 &\quad - d_c^* E_c^*(\mathbf{x}, t) \Psi_e(\mathbf{x}, t). \quad (4)
 \end{aligned}$$

In the following, we will assume that all atoms are initially condensed in the ground state and that the probe pulse is very weak; in this case, the probe will not essentially affect the (macroscopic) condensate, so that the optical polarization caused by the noncondensed atoms generated by incoherent processes can be safely neglected. The effect of the coupling beam on the condensed atoms alone is, in fact, negligible for any value of its intensity, since its frequency is off-resonance from any optical transition starting from the ground level. For small atomic densities $N_o(N_o/|\mathbf{k}_p|^3 \ll 1)$, we can also assume that the photonic mode structure inside the condensed cloud is not strongly modified, compared to the free space one, so that the excited-state spontaneous emission rate γ_e can be taken to be the same as in free space [6]. In the spirit of a semiclassical local density approximation [4, 7], we will also neglect the effect of the external trapping potential and consider the probe and coupling beams as monochromatic plane waves of the form $E_{p,c}(\mathbf{x}, t) = \bar{E}_{p,c} e^{i[\mathbf{k}_{p,c}\mathbf{x} - \omega_{p,c}t]}$ illuminating a locally homogeneous condensate described by the field $\Psi_g(\mathbf{x}, t) = \bar{\Psi}_g e^{i[\mathbf{k}_g\mathbf{x} - (\omega_g + \mathbf{k}_g^2/2m)t]}$, where $|\bar{\Psi}_g|^2 = N_o$. For a cloud at rest, $\mathbf{k}_g = 0$ and $\Psi_g(\mathbf{x}, t) = \bar{\Psi}_g e^{-i\omega_g t}$, while for a cloud that uniformly and homogeneously moves with a velocity \mathbf{v} , $\mathbf{k}_g = m\mathbf{v}/\hbar$. Due to the energy and momentum conservation, the amplitudes of the excited and metastable components

of the atomic field have the same plane-wave structure as for the ground state; i.e.,

$$\Psi_e(\mathbf{x}, t) = \bar{\Psi}_e \exp\{i[(\mathbf{k}_p + \mathbf{k}_g)\mathbf{x} - (\omega_p + \omega_g^{(\text{eff})})t]\}, \quad (5)$$

$$\Psi_m(\mathbf{x}, t) = \bar{\Psi}_m \exp\{i[\mathbf{k}_p - \mathbf{k}_c + \mathbf{k}_g)\mathbf{x} - (\omega_p - \omega_c + \omega_g^{(\text{eff})})t]\}. \quad (6)$$

Inserting these forms into Eq. (4) and then into Eq. (3) yields

$$\bar{\Psi}_m = \frac{-d_c^* \bar{E}_c^*}{\hbar(\Delta_m(\mathbf{k}_p, \omega_p) + i\gamma_m)} \bar{\Psi}_e \quad (7)$$

and

$$\bar{\Psi}_e = \frac{-d_p \bar{E}_p}{\hbar(\Delta_e(\mathbf{k}_p, \omega_p) + i\gamma_e - |d_c E_c|^2/(\Delta_m(\mathbf{k}_p, \omega_p) + i\gamma_m))} \bar{\Psi}_g, \quad (8)$$

which generalizes the expression used for describing EIT in the Λ -type three-level atomic configuration by including kinetic-energy corrections associated with the atomic recoil. These appear in the detuning from the excited level

$$\Delta_e(\mathbf{k}_p, \omega_p) = \omega_g^{(\text{eff})} + \omega_p - \omega_e^{(\text{eff})}(\mathbf{k}_p) \quad (9)$$

and from the metastable level

$$\Delta_m(\mathbf{k}_p, \omega_p) = \omega_g^{(\text{eff})} + \omega_p - \omega_c - \omega_m^{(\text{eff})}(\mathbf{k}_p), \quad (10)$$

where $\omega_g^{(\text{eff})} = \omega_g^{(\text{eff})}(\mathbf{k}_g) = \omega_g + \hbar\mathbf{k}_g^2/2m$, $\omega_e^{(\text{eff})}(\mathbf{k}_p) = \omega_e + \hbar(\mathbf{k}_p + \mathbf{k}_g)^2/2m$, and $\omega_m^{(\text{eff})}(\mathbf{k}_p) = \omega_m + \hbar(\mathbf{k}_p - \mathbf{k}_c + \mathbf{k}_g)^2/2m$. Only the dependence on \mathbf{k}_p and ω_p , which will be needed in the following, is explicitly indicated, whereas the dependence on the other setup parameters ω_c , \mathbf{k}_c , and \mathbf{k}_g is left implicit. Since the dipole moment per unit volume at the probe frequency is given by $d_p^* \bar{\Psi}_g^* \bar{\Psi}_e$, Eq. (8) leads to a simple expression for the

dielectric function $\epsilon(\omega_p, \mathbf{k}_p)$ of the dressed atomic cloud,

$$\epsilon(\omega_p, \mathbf{k}_p) = 1 + \frac{4\pi N_o |d_p|^2}{\hbar(|\Omega_c|^2 / (\Delta_m + i\gamma_m) - \Delta_e - i\gamma_e)}, \quad (11)$$

where $\Omega_c = |d_c E_c|/\hbar$ is the Rabi frequency of the coupling beam. If the spontaneous decay rate γ_e is much larger than all other frequency scales and, in particular, if $\gamma_e \gg \Delta_e$, then the detuning Δ_e of the excited state can be neglected in Eq. (11). If we further assume that the decoherence rate γ_m is much smaller than $\Gamma = \Omega_c^2/\gamma_e$, then Eq. (11) simplifies to

$$\epsilon(\omega_p, \mathbf{k}_p) = 1 + \frac{4\pi N_o |d_p|^2}{\hbar\gamma_e} \left\{ i + \frac{\Gamma}{\Delta_m(\mathbf{k}_p, \omega_p) + i\Gamma} \right\}. \quad (12)$$

Providing the Rabi frequency Ω_c of the coupling beam is smaller than the excited state linewidth γ_e , nearly total transmission occurs within a small bandwidth Γ of frequencies around $\omega_p^{(o)} = \omega_m^{(\text{eff})}(\mathbf{k}_p^{(o)}) + \omega_c - \omega_g^{(\text{eff})}$, for which $\Delta_m(\mathbf{k}_p^{(o)}, \omega_p^{(o)}) = 0$; in the same frequency window, the refractive index, which is unity ($\omega_p^{(o)} = c|\mathbf{k}_p^{(o)}|$) at line center, has a very steep dispersion. This implies that a narrow-band pulse would propagate with a very small group velocity without being appreciably absorbed [1, 2, 8]. Approximating the atomic dispersion of the metastable $|m\rangle$ state after the absorption of a photon from the probe beam and its immediate reemission into the coupling beam as a linear one with the group velocity

$$\mathbf{v}_a = \mathbf{v} + \frac{\hbar}{m}(\mathbf{k}_p^{(o)} - \mathbf{k}_c), \quad (13)$$

the detuning in the denominator of Eq. (12) can be approximated by $\Delta_m(\mathbf{k}_p, \omega_p) \simeq (\omega_p - \omega_p^{(o)}) - (\mathbf{k}_p - \mathbf{k}_p^{(o)})\mathbf{v}_a$, so that $\epsilon(\omega_p, \mathbf{k}_p)$ acquires the new form

$$\epsilon(\omega_p, \mathbf{k}_p) \simeq 1 + \frac{4\pi N_o |d_p|^2}{\hbar\gamma_e\Gamma} [(\omega_p - \omega_p^{(o)}) - (\mathbf{k}_p - \mathbf{k}_p^{(o)})\mathbf{v}_a]. \quad (14)$$

The dispersion law for a probe propagating in the direction of the unit vector $\hat{\mathbf{k}}_p = \mathbf{k}_p/|\mathbf{k}_p|$ with a frequency centered on the EIT transparency window can be obtained by inserting Eq. (14) into $\epsilon(\omega, \mathbf{k})\omega^2 = c^2\mathbf{k}^2$ and then linearizing around $\omega_p = \omega_p^{(o)}$ and $\mathbf{k}_p = \mathbf{k}_p^{(o)}$:

$$(\omega_p - \omega_p^{(o)}) = (\mathbf{k}_p - \mathbf{k}_p^{(o)}) \frac{\eta \mathbf{v}_a + c\hat{\mathbf{k}}_p}{1 + \eta}, \quad (15)$$

where $\eta = 2\pi N_o |d_p|^2 \omega_p^{(o)} / \hbar \Omega_c^2$. The relevant group velocity $\mathbf{v}_g = \nabla_{\mathbf{k}_p} \omega_p$ at two-photon resonance can finally be written as

$$\mathbf{v}_g = \frac{c}{1 + \eta} \hat{\mathbf{k}}_p + \frac{\eta}{1 + \eta} \mathbf{v}_a. \quad (16)$$

For a sample at rest, in the infinite mass limit, \mathbf{v}_a is negligible and the group velocity has the usual expression $\mathbf{v}_g = c\hat{\mathbf{k}}_p/(1 + \eta)$ [8]. In this case, for values of η much larger than unity, light speeds much less than c can be observed as, e.g., in [1], where $\eta \sim 10^7$. However, we cannot neglect atomic recoil when η is much larger than unity and is of the order of $c/|\mathbf{v}_a|$, since \mathbf{v}_g becomes comparable in magnitude to \mathbf{v}_a . In this case, the group velocity can be written as

$$\mathbf{v}_g \simeq \frac{c}{\eta} \hat{\mathbf{k}}_p + \mathbf{v}_a. \quad (17)$$

While the first term $c\hat{\mathbf{k}}_p/\eta$ recovers Eq. (1) in [1], the other term seems to suggest that light is dragged by the metastable atoms, which recoil at a velocity of \mathbf{v}_a ; however, we stress that, under our conditions, $|\bar{\Psi}_e|^2 + |\bar{\Psi}_m|^2 \ll |\bar{\Psi}_g|^2 = N_o$ and, therefore, the center-of-mass motion of the atomic cloud is weakly affected by light.

We now proceed to discuss novel and interesting effects associated with result (17). For an atomic sample at rest, in which $|g\rangle$ and $|m\rangle$ are hyperfine sublevels of the same ground state with energies very close to each other, $\mathbf{k}_g = 0$ and \mathbf{v}_a turns out to be a negligibly small quantity for copropagating probe and coupling beams (Fig. 1a). Such a situation was examined in [7], e.g., where recoil is explicitly omitted. On the other hand, for counterpropagating beams (Fig. 1b), \mathbf{v}_a is nearly twice the recoil velocity of the $|g\rangle \rightarrow |e\rangle$ optical transition and it is directed as the probe wavevector; in such a geometry, the group velocities are then restricted by the lower bound $|\mathbf{v}_a|$. In the case of sodium atoms (D_2 line), this quantity is approximately 6 cm/s, i.e., 300 times smaller than the lowest group velocity of 17 m/s so far reported in sodium [1]. Since the most stringent upper bound to η is actually set by the lower bound to the coupling intensities $\Omega_c^2 > \gamma_m\gamma_e$, which have to be applied in order for the EIT to be fully developed, a substantial reduction of γ_m [1] will lead to much larger values of η , so that the effect of atomic recoil, as predicted by Eq. (17), could possibly be observed.

For a sample moving with the uniform velocity \mathbf{v} , our theory recovers the well-known Fresnel–Fizeau light-drag [5] effect; in the slow-light case, all velocities involved are nonrelativistic and the Galilean composition of velocities is obtained as in Eq. (17). Unlike the effect of atomic recoil, Fresnel–Fizeau drag occurs even in the infinite atomic mass limit. Recently, a related effect was shown to lead to exotic features of

light propagation in the more complex situation of non-uniformly moving media [9], but this is beyond the scope of this paper.

With copropagating coupling and probe beams and the appropriate choice of the atomic levels, i.e., the Λ configuration, in which the level m has an energy lower than g (see Fig.1c), the recoil velocity \mathbf{v}_a is directed oppositely with respect to the probe beam even for a sample initially at rest. In this case, for sufficiently small values of c/η , the probe wavevector and the group velocity turn out to be oppositely directed. From a phenomenological point of view, the possibility of attaining such *negative* group velocities may be exploited to investigate rather novel effects in the domain of geometrical optics, such as, e.g., negative refraction angles at the boundary with free space [10]. Recent developments in coherently prepared atomic media have revived the interest in the issue of negative group velocities. With respect to the previous works on the subject [11, 12], our proposal is characterized by the fact that both absorption and group velocity dispersion almost vanish in the frequency range of interest, so that the shape of the light pulse remains essentially unchanged. Negative group velocities were also predicted to occur in an EIT configuration for coupling and probe beams copropagating in a *hot* atomic gas [13]: because of the Doppler effect, light interacts only with a narrow class of atomic velocities and the sample behaves as an effectively moving one. If the selected atoms move in the opposite direction with respect to the probe wavevector, negative group velocities may occur for sufficiently dense samples, as is also predicted by the present treatment when a nonzero atomic velocity is explicitly included in Eq. (13).

In actual experiments, a nonzero temperature and the finite size of the sample may cause a finite velocity spread for the ground-state atoms. This can be taken into account by integrating dielectric susceptibility (12) over the velocity distribution of ground-state atoms. For a Lorentzian velocity distribution [13], a straightforward calculation leads to the same form of susceptibility, where Γ in the denominator is replaced by $(\Gamma + \Gamma_D)$, $\Gamma_D = |\mathbf{k}_p - \mathbf{k}_c|v_D$ being the Doppler width expressed in terms of the velocity spread v_D . In physical terms, the effect of a Doppler width Γ_D comparable to the subnatural linewidth Γ is similar to the effect of having a lower level decoherence γ_m of the order of Γ , i.e., a broadened absorption dip and a reduced contrast of the transparency feature, which is no longer complete. From a quantitative point of view, the broadening due to the finite size of a zero-temperature BEC is generally smaller than the recoil velocity and thus can be safely neglected with respect to Γ . For hot samples, Γ_D is negligible only if $\mathbf{k}_p \approx \mathbf{k}_c$, i.e., for copropagating coupling and probe beams and small lower state energy splitting. In addition, if the Doppler broadening $|\mathbf{k}_p|v_D$

of the excited state is comparable to its linewidth γ_e , the detuning Δ_e can no longer be neglected in Eq. (11) and a more detailed treatment has to be carried out [13].

The theory described up to now neglected the atom–atom interactions (collisions). These are commonly modeled [4] by adding quartic terms to Hamiltonian (1) and give rise to additional cubic terms of the form $\sum_j G_{i,j} |\psi_j|^2 \psi_i$ in the mean-field wave Eqs. (2)–(4). The coupling coefficients $G_{i,j}$ are proportional to the s -wave scattering length for collisions between atoms in the i and j states ($i, j = \{e, g, m\}$), respectively. To the lowest order in the probe intensity, only the $G_{i,g} |\psi_g|^2 \psi_i$ terms contribute to the sum causing a mean-field shift of the e and m level frequencies in Eqs. (9) and (10). The excited level e is adiabatically eliminated in the present treatment, while the collisional frequency shift of the metastable level m gives rise to a small shift of the two-photon resonance condition in Eq. (12). This means that the photon dragging effects of interest originate from the independent recoil of each atom and, thus, Bogoliubov’s sound velocity $v_s = \sqrt{G_{g,g} N_o/m}$ does not appear to be relevant to the linear propagation of light pulses in condensed media under EIT. The dispersion of Bogoliubov’s phonons [4] may, on the other hand, be crucial in more complex optical processes which involve the excitation of phonons in the condensate, such as, e.g., Brillouin scattering by density fluctuations [14].

In conclusion, we have shown that even in a sample at rest, under appropriate EIT conditions, light can be dragged by the atoms which recoil after the absorption of a photon from the probe beam and the subsequent emission into the coupling beam. We hope that a feasible upgrade of the experimental setup commonly used to study light propagation in EIT configurations [1] will soon allow the detection of such atomic recoil effects.

REFERENCES

1. L. V. Hau, S. E. Harris, and Z. Dutton, *Nature* **397**, 597 (1999).
2. A. Kasapi, M. Jain, and G. Y. Yin, *Phys. Rev. Lett.* **74**, 2447 (1995); O. Schmidt, R. Wynands, Z. Hussein, *et al.*, *Phys. Rev. A* **53**, R27 (1996); M. M. Kash, V. A. Sautenko, and A. S. Zibrov, *Phys. Rev. Lett.* **82**, 5229 (1999); D. Budker, D. F. Kimball, and S. M. Rochester, *Phys. Rev. Lett.* **83**, 1767 (1999).
3. S. Harris, *Phys. Today* **50**, 36 (1997); E. Arimondo, *Prog. Opt.* **35**, 257 (1996).
4. F. Dalfovo, S. Giorgini, L. P. Pitaevskii, and S. Stringari, *Rev. Mod. Phys.* **71**, 463 (1999).
5. L. D. Landau and E. M. Lifshitz, *Course of Theoretical Physics, Vol. 8: Electrodynamics of Continuous Media* (Nauka, Moscow, 1982; Pergamon, New York, 1984), Chap. X.

6. O. Morice *et al.*, Phys. Rev. A **51**, 3896 (1995); L. You, M. Lewenstein, R. J. Glauber, and J. Cooper, Phys. Rev. A **53**, 329 (1996).
7. G. Morigi and G. S. Agarwal, Phys. Rev. A **62**, 13801 (2000).
8. S. E. Harris, J. E. Field, and A. Kasapi, Phys. Rev. A **46**, R29 (1992).
9. U. Leonhardt and P. Piwnicki, Phys. Rev. A **60**, 4301 (1999); Phys. Rev. Lett. **84**, 822 (2000).
10. I. M. Frank, Pis'ma Zh. Éksp. Teor. Fiz. **28**, 482 (1978) [JETP Lett. **28**, 446 (1978)].
11. G. B. Garrett and D. E. McCumber, Phys. Rev. A **1**, 305 (1970); S. Chu and S. Wong, Phys. Rev. Lett. **48**, 738 (1982); E. L. Bolda, J. C. Garrison, and R. Y. Chiao, Phys. Rev. A **49**, 2938 (1994).
12. M. Artoni *et al.*, submitted to Phys. Rev. A.
13. Y. Rostovtsev, O. Kocharovskaja, and M. O. Scully, quant-ph/0001058.
14. A. B. Matsko, Yu. V. Rostovtsev, and H. Z. Cummins, Phys. Rev. Lett. **84**, 5752 (2000).

Stabilization of Bound State Decay in an Intense Monochromatic High-Frequency Field

N. L. Manakov*, M. V. Frolov*, B. Borca**,¹ and A. F. Starace**

* Voronezh State University, Universitetskaya pl. 1, Voronezh, 394893 Russia

** Department of Physics and Astronomy, The University of Nebraska, Lincoln, NE 68588-0111, USA

Received August 8, 2000

The formalism of complex quasienergies is used for exact calculation of the field-dependent decay rate for a weakly bound particle (in the model of a three-dimensional zero-range potential) in a strong monochromatic laser field. It is shown that the adiabatic (quasistationary) stabilization regime in this model occurs at frequencies ω exceeding the binding energy and only in a limited intensity range. A simple estimate is obtained for the critical field of stabilization breakdown. The effect may be observed for the decay of H^- ions in the field of a neodymium laser of femtosecond duration. © 2000 MAIK “Nauka/Interperiodica”.

PACS numbers: 32.80.-t

In spite of the fact that the possibility of the atomic decay rate decreasing with an increase in laser intensity at frequencies higher than the ionization potential was pointed out more than ten years ago [1, 2], the physical nature of this interesting nonlinear effect and its dependence on the type of atomic potential and field parameters still remain to be clarified. Essentially, the case in point is a radical modification of the conventional pattern of the photoeffect in a strong field. In [1], the onset of stabilization was associated with a peculiar kind of modification of the atomic potential in an intense high-frequency field, as a result of which the level width Γ (imaginary part of the complex quasienergy $\epsilon = \text{Re}\epsilon - i\Gamma/2$) decreases infinitely as the intensity increases, to arrive at the adiabatic (or quasistationary) stabilization (QS). An alternative interference mechanism of QS was proposed for the Rydberg states, where the decrease in Γ is caused by destructive interference of the ionization amplitudes of closely spaced levels mixed by a strong field and populated via Raman transitions from the initial state [2]. In recent years, the idea of “dynamic stabilization” (DS) [3] due to the pulsed character of the field has also been actively discussed. Numerical calculations indicate that the “stabilization breakdown” may also occur in ultrastrong pulsed fields [4]. However, the authors of a recent work [5] used the quasistationary quasienergy states (QQESs) as an adiabatic basis in a strong field (see also [6]) to demonstrate that the DS and QS have the same origin. Finally, it was asserted in some works that stabilization is in principle impossible, in particular, QS upon ionization from a short-range potential [7] and DS in pulsed fields [8]. Clearly, these

problems arise because the numerical solution of the initial value problem for the Schrödinger equation in a strong field is a challenge, while analysis of the problem is lacking for exactly solvable analytical models. In this letter, the exactly solvable short-range potential model is taken as an example to analyze the questions of whether the QS regime may occur in the decay of a weakly bound level and, if it does, how large the intensity range for the stabilization is.

We consider quasistationary decay of a bound state in the field of a strong monochromatic wave with electric vector

$$\mathbf{F}(t) = \frac{F}{\sqrt{1+\eta^2}} \{ \cos \omega t, \eta \sin \omega t, 0 \},$$
$$-1 \leq \eta \leq +1$$

and intensity $I = cF^2/8\pi$ by applying the QQES formalism [9] to the exactly solvable 3D model of a short-range (δ -) potential having a single bound state with energy E_0 [10]. The exact equation for the complex quasienergy ϵ contains the degree of linear polarization $l = (1 - \eta^2)/(1 + \eta^2)$ and the characteristic dimensionless parameters of the problem: $\hbar\omega/|E_0|$ and the ratio of the mean energy of electron oscillations in a field $(eF)^2/4m\omega^2$ to the photon energy $\Delta = (eF)^2/4m\hbar\omega^3$ or to the binding energy $\mathcal{E}_F = (eF)^2/4m\omega^2|E_0| = \Delta(\hbar\omega/|E_0|)$. Below, the following dimensionless units are used: energy and $\hbar\omega$ is in units of $|E_0|$, and field intensity is in

units of $F_0 = \sqrt{4m|E_0|^3}/|e|\hbar$, so that $\mathcal{E}_F = F^2/\omega^2$ and $\Delta =$

¹ On leave from Institute for Space Sciences, Bucharest, Romania.

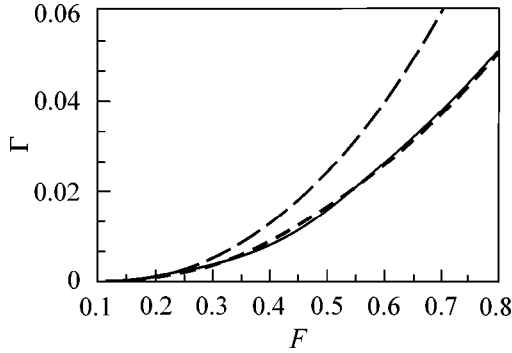


Fig. 1. Γ as a function of F for $\omega = 0.74$ and circular polarization of laser field. Solid line corresponds to the exact (numerical) calculation according to Eq. (1); dotted line is the result of perturbation theory (3) for ω ; dashed line is weak-field approximation (5).

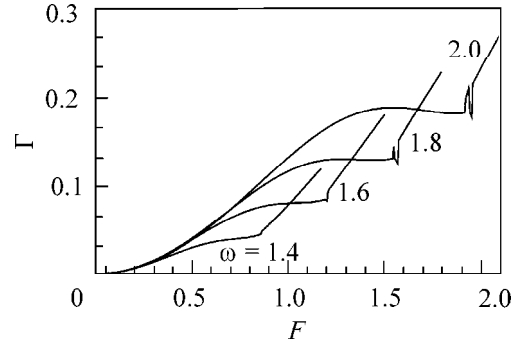


Fig. 2. Γ as a function of F for above-threshold frequencies (circular polarization). The ω values are indicated near the corresponding curves.

F^2/ω^2 (note that the Keldysh parameter $\gamma = \sqrt{2m|E_0|} \omega/eF$ in these units is $\gamma = \omega/\sqrt{2}F$).

The equation for ϵ has the simplest form in the case of circularly polarized $\mathbf{F}(t)$ with $\eta = \pm 1$ [11]:

$$\sqrt{\mathcal{E}_F - \epsilon} = 1 \quad (1)$$

$$+ \sqrt{\frac{\omega}{4\pi i}} \int_0^\infty \frac{d\tau}{\tau^{3/2}} \exp\left\{\frac{-i(\mathcal{E}_F - \epsilon)\tau}{\omega}\right\} \left\{ \exp\left[4i\Delta \frac{\sin^2 \tau/2}{\tau}\right] - 1 \right\}.$$

For elliptic polarization ($0 \leq |\eta| < 1$), ϵ is the eigenvalue of a 1D integral equation for a periodic function $\varphi_\epsilon(t)$ [which determines the asymptotic behavior of the exact QUES function $\Phi_\epsilon(\mathbf{r}, t)$ at $r \rightarrow 0$], with a kernel structurally similar to the integrand in Eq. (1) [10]. Insofar as $\text{Im} \epsilon < 0$, the integrals of type (1) formally diverge at the upper limit and thus should be considered in the sense of analytical continuation from the upper ϵ half-plane. We use the following relation for this analytical continuation:

$$\int_0^\infty \frac{d\tau}{\tau^{1/2}} e^{-i\alpha\tau} f(\tau) = \frac{1}{\sqrt{4\pi i}} \int_{-\infty}^\infty \frac{dk}{\sqrt{\alpha + k}} \int_{-\infty}^\infty d\tau e^{ik\tau} f(\tau), \quad (2)$$

where the double integral converges for any $\alpha = (\mathcal{E}_F - \epsilon)/\omega$. Note that in some works, where the QUES method was applied to the δ -well model [10], the divergence of the integrals of type (1) was eliminated by substituting $\epsilon \approx E_0 = -1$, which, clearly, is unjustified for strong fields. In particular, this led the authors of [7] to the erroneous results in their Fig. 5 and to the erroneous conclusion about the absence of QS for short-range potentials.

The numerical results obtained for $\Gamma(F)$ (Figs. 1–3) clearly demonstrate the presence of the QS regime for above-threshold frequencies and abrupt stabilization breakdown, i.e., a sharp increase in $\Gamma(F)$ starting at some critical value $F = F_{cr}$. The width (in F) of the QS

region increases with ω . One can see from Fig. 3 that the F_{cr} value does not depend on the polarization type [see Eq. (7) below], while the $\Gamma(F)$ decrease in the QS region is more pronounced for linear polarization.

Since the problem of stabilization breakdown (and critical field value F_{cr}) is of crucial importance (in particular, it argues against the existence of the so-called “Death Valley,” i.e., a broad and deep minimum in the F -dependent lifetime of a quasistationary atomic level [1]), let us make some analytical estimates confirming the numerical results and allowing their physical interpretation. For circular polarization, ϵ is defined as a (complex) eigenvalue of the stationary Hamiltonian in a coordinate frame rotating with frequency ω [9],

$$\mathcal{H}_{rot}(\mathbf{r}) = -\nabla_{\mathbf{r}}^2 + U(\mathbf{r}) + Fx \pm \omega \hat{L}_z,$$

where \hat{L} is the orbital angular momentum operator. We will treat the operator $\omega \hat{L}_z$ perturbatively and use perturbation theory (PT) in the basis of quasistationary states of a particle in the δ -potential $U(\mathbf{r}) = 4\pi\delta(\mathbf{r})(\partial/\partial r)$ and a constant field of strength \mathbf{F} . The PT for the quasistationary states is developed, e.g., in [12]. A convenient expression for the Green’s function of our problem can be found in [13], where it is expressed through the regular and irregular Airy functions $\text{Ai}(x)$ and $\text{Bi}(x)$ and where the computational technique is also presented for second-order PT. With the $\sim \omega^2$ correction, the expression for ϵ is

$$\epsilon = E - \frac{\omega^2}{360F^{2/3}} \frac{I^{(4)}(\xi)}{I(\xi)}, \quad \xi = -\frac{E}{F^{2/3}}, \quad (3)$$

where the complex energy E of a quasistationary state in a field \mathbf{F} is a root of the transcendent equation {the $E = E(F)$ function is analyzed in [13]}

$$1 + \pi F^{1/3} J(-EF^{-2/3}) = 0, \quad (4)$$

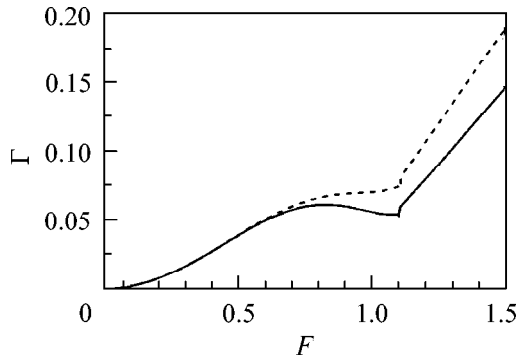


Fig. 3. Γ as a function of F for (solid line) linear and (dotted line) circular polarization of a laser field with $\omega = 1.55$.

where $J(x) = \text{Ai}'(x)\text{Ci}'(x) - x\text{Ai}(x)\text{Ci}(x)$, $\text{Ci}(x) = \text{Bi}(x) + i\text{Ai}(x)$, $I(x) = \text{Ai}(x)\text{Ci}(x)$, and $I^{(4)}(x) = d^4I(x)/dx^4$. The F value in Eqs. (3) and (4) is not assumed to be small. Using the properties of the Airy functions and Eqs. (3) and (4), one can easily determine the conditions for applicability of PT to the $\omega\hat{L}_z$ operator [i.e., for the smallness of a correction $\sim\omega^2$ to the energy E in Eq. (3)].

In the weak-field limit ($F \ll 1$), one has

$$\epsilon = -1 - \frac{1}{16}F^2 \left[1 + \frac{3}{2}F^2 + \frac{7}{24}(1 + 13F^2)\omega^2 \right] - \frac{i}{4}F \left[1 + \frac{4}{45}\frac{\omega^2}{F^3} \right] e^{-4/3F}. \quad (5)$$

One can see from Eq. (5) that the perturbative treatment of $\omega\hat{L}_z$ is only justified if ω is small enough ($\omega^2 < F^3 \ll 1$) that the frequency-dependent correction to the tunneling preexponential factor is small. Note that the corresponding Stark shift $\text{Re}\epsilon + 1$ exactly coincides with the two leading terms in the power series expansion of the known expressions for the dynamic polarizability and hyperpolarizability of a weakly bound particle [14]. The inapplicability of expansion (5) at $\omega > 1$ is evident, e.g., from the fact that the F dependence of the level width follows a power law. In particular, to the lowest order in F , one has $\Gamma_0^{(1)} = (8F^2/3\omega^4)(\omega - 1)^{3/2}$ for any polarization of $\mathbf{F}(t)$.

In the $F \gg 1$ limit, Eq. (3) takes the form

$$\epsilon = 0.44133122e^{-i(\pi/3)}F^{2/3} - F^{1/3} \left[0.86328690e^{-i(\pi/6)} - 0.02548960e^{i(\pi/3)}\frac{\omega^2}{F^3} \right] \quad (6)$$

and demonstrates that the perturbative treatment of $\omega\hat{L}_z$ in ultrastrong fields is justified for any frequencies $\omega^2 < F^3$ (curiously, this inequality is the inverse of the condition for applicability of the PT in F to the complex

quasienergy [15]: $\Delta \equiv F^2/\omega^3 < 1$). Although Eq. (6) was derived using the two-term asymptotic expression for energy E obtained in [13] for ultrastrong static fields, result (6) has a fundamental character and confirms (together with the results of direct numerical computations) stabilization breakdown, at least in ultrastrong fields. Note that at $\omega < 1$, Eq. (3) agrees well with the exact result even in the region where the PT series in F diverges: starting at $F \sim 0.5$, the exact $\Gamma(F)$ curve for $\omega = 0.74$ (Fig. 1) virtually coincides with the curve calculated from Eq. (3). In other words, the action of a strong circularly polarized field at $\omega < 1$ is equivalent to the action of a strong static field of strength \mathbf{F} . At $\omega > 1$, the PT in $\omega\hat{L}_z$ applies only to ultrastrong fields, so that in the QS region and at $F \geq F_{cr}$ the results can only be obtained by numerical methods.

The results of numerical and analytical calculations allow one to determine the main regularities of quasi-stationary level decay in the light field for different ratios between $|E_0|$, ω , and F . At $\Delta \ll 1$, multiphoton decay prevails; i.e., $\Gamma \sim F^{2N}$ with $N = \lfloor |E_0|/\omega \rfloor$ for any F and ω , including $\omega \ll 1$. As F increases, the situation qualitatively depends on the frequency: for small ω , the value $\Delta \sim 1$ is attained in a relatively weak field F and the perturbative decay regime is smoothly replaced by tunneling (according to Keldysh). This mechanism is operative in fields much weaker than the intraatomic fields [see Eq. (5) and the dashed line in Fig. 1]. It was considered in detail in [16] for arbitrary values of the Keldysh parameter γ . At $\omega > 1$, the multiphoton ionization mechanism prevails even in fields for which the lowest order PT ($\Gamma_0^{(1)}$) does not apply and the higher order corrections to $\Gamma_0^{(1)}$, caused by reemission and direct above-threshold photon absorption, should be taken into account. However, for these F values, the linear dependence of Γ on the intensity is replaced by a smoother dependence (the $\sim F^2$ correction to the width $\Gamma_0^{(1)}$ is negative [14]) and tunneling is replaced by the QS regime starting at fields $F < \omega$ for which the high-order PT corrections become significant. Evidently, the standard PT, with F as a small parameter, does not apply in the range of “developed” stabilization.

Turning to the stabilization breakdown point F_{cr} , note that it is preceded by a (rather narrow) range of fields $F \leq F_{cr}$ where the width Γ suffers irregular jumps with relatively small amplitudes (Fig. 2; the exact numerical calculation of Γ in this region presents considerable difficulty). To perform a more detailed analysis of the level width in the breakdown region, we calculated nonperturbatively the partial widths $\Gamma^{(n)}(F)$ corresponding to the absorption of a fixed number n of photons. Having no room for a detailed discussion, we merely point out that the “one-photon” width $\Gamma^{(1)}$ (corresponding to the photoelectron energy $E_p = \text{Re}\epsilon - \mathcal{E}_F + \omega$ and almost completely determining the total width Γ up

to the middle of the QS interval) has a deep minimum in the breakdown region, so that the contribution to Γ in the breakdown region comes from a large number of (interfering) above-threshold n -photon decay channels. We assume that the irregular $\Gamma(F)$ dependence in this narrow range of F values is a quantum manifestation of the well-known chaotic behavior typical of classical systems with strong nonlinearity at a certain ratio of relevant parameters (for the application of the ideas of dynamic chaos to the stabilization problem, see, e.g., [17]). Assuming that the minimum in the one-photon width $\Gamma^{(1)}$ is caused by closing the direct photoionization channel, one can estimate F_{cr} from the equality $\text{Re}\epsilon - \mathcal{E}_F + \omega = 0$. Neglecting the Stark shift $\text{Re}\epsilon + 1$, which is small at $\omega \sim 1$, one has

$$F_{cr} \approx \omega \sqrt{\omega - 1}. \quad (7)$$

This estimate agrees nicely with the F_{cr} value obtained by numerical calculations for frequencies up to $\omega \leq 3$; a slight decrease [compared to Eq. (7)] in F_{cr} with increasing ω is due to the neglect of the Stark shift. Therefore, both the specific behavior of $\Gamma(F)$ in the QS region and the occurrence of this region and its breakdown are caused by a profound modification of the threshold phenomena for the photoeffect in a strong monochromatic field.

Note in conclusion that the analysis carried out in this work gives evidence for the presence, in a limited intensity range, of the QS regime in the quasistationary decay of a weakly bound state in a strong field with frequency higher than the binding energy and also provides a simple estimate for the QS breakdown point F_{cr} . The δ -potential model adequately describes photoprocesses in negative ions, in particular, H^- (with $|E_0| \approx 0.752$ eV). For H^- , the frequency of the neodymium laser equals $\omega_{\text{Nd}} \approx 1.55$ and stabilization is possible (Fig. 3) in fields $F \sim 1$ ($I \approx 3 \times 10^{12}$ W/cm²). Since the lifetime of H^- in this field is rather short, $\tau \sim 1/\Gamma \sim 10$ fs, stabilization can be observed only in experiments with femtosecond laser pulses.

We are grateful to M.V. Fedorov for helpful discussions. This work was supported in part by the INTAS-RFFI (grant no. 97-673), the Russian Foundation for Basic Research (project no. 00-02-17843), and the NSF (grant no. PHY-0070980).

REFERENCES

1. M. Pont and M. Gavrilă, Phys. Rev. Lett. **65**, 2362 (1990); M. Gavrilă, in *Photon and Electron Collisions*

with Atoms and Molecules, Ed. by P. G. Burke and C. J. Joachain (Plenum, New York, 1997), p. 47.

2. M. V. Fedorov and A. M. Movsesian, J. Phys. B **21**, L155 (1988); M. V. Fedorov, Laser Phys. **9**, 209 (1999).

3. Q. Su, Laser Phys. **2**, 241 (1993); Q. Su, B. P. Irving, C. W. Johnson, and J. H. Eberly, J. Phys. B **29**, 5755 (1996).

4. Q. Su, B. P. Irving, and J. H. Eberly, Laser Phys. **7**, 1 (1997); A. Patel, N. J. Kylstra, and P. L. Knight, J. Phys. B **32**, 5759 (1999); A. M. Popov, O. V. Tikhonova, and E. A. Volkova, Laser Phys. **10**, 779 (2000).

5. M. Dorr and R. M. Potvliege, J. Phys. B **33**, L233 (2000).

6. H. C. Day, B. Piraux, and R. M. Potvliege, Phys. Rev. A **61**, 031402 (2000).

7. V. P. Kraĭnov and M. A. Preobrazhenskii, Zh. Ėksp. Teor. Fiz. **103**, 1142 (1993) [JETP **76**, 559 (1993)].

8. S. Geltman, J. Phys. B **32**, 853 (1999); T. Mercouris and C. Nicolaides, J. Phys. B **32**, 2371 (1999); C. Figueira, A. Fring, and R. Schrader, Laser Phys. **9**, 379 (1999).

9. N. L. Manakov, V. D. Ovsianikov, and L. P. Rapoport, Phys. Rep. **141**, 319 (1986).

10. N. L. Manakov and A. G. Faĭnshteĭn, Dokl. Akad. Nauk SSSR **244**, 567 (1979) [Sov. Phys. Dokl. **24**, 41 (1979)]; Zh. Ėksp. Teor. Fiz. **79**, 751 (1980) [Sov. Phys. JETP **52**, 382 (1980)].

11. N. L. Manakov and L. P. Rapoport, Zh. Ėksp. Teor. Fiz. **69**, 842 (1975) [Sov. Phys. JETP **42**, 430 (1975)]; I. J. Berson, J. Phys. B **8**, 3078 (1975).

12. Ya. B. Zel'dovich, Zh. Ėksp. Teor. Fiz. **39**, 776 (1961) [Sov. Phys. JETP **12**, 542 (1961)].

13. N. L. Manakov, M. V. Frolov, A. F. Starace, and I. I. Fabrikant, J. Phys. B **33**, R141 (2000).

14. N. L. Manakov, M. A. Preobrazhenskii, L. P. Rapoport, and A. G. Faĭnshteĭn, Zh. Ėksp. Teor. Fiz. **75**, 1243 (1978) [Sov. Phys. JETP **48**, 626 (1978)].

15. N. L. Manakov and A. G. Faĭnshteĭn, Teor. Mat. Fiz. **48**, 375 (1981); R. M. Potvliege and R. Shakeshaft, Phys. Rev. A **41**, 1609 (1990).

16. L. V. Keldysh, Zh. Ėksp. Teor. Fiz. **47**, 1945 (1964) [Sov. Phys. JETP **20**, 1307 (1964)]; A. I. Nikishov and V. I. Ritus, Zh. Ėksp. Teor. Fiz. **50**, 255 (1966) [Sov. Phys. JETP **23**, 168 (1966)]; A. M. Perelomov, V. S. Popov, and M. V. Terent'ev, Zh. Ėksp. Teor. Fiz. **50**, 1393 (1966) [Sov. Phys. JETP **23**, 924 (1966)]; Zh. Ėksp. Teor. Fiz. **51**, 309 (1966) [Sov. Phys. JETP **24**, 207 (1967)].

17. W. Chism, D. I. Choi, and L. E. Reichl, Phys. Rev. A **61**, 054702 (2000).

Note added in proof: We have recently become aware of a related paper by P.S. Krstic *et al.*, Phys. Rev. A **44**, 3089 (1991).

Translated by V. Sakun

The Ion Cyclotron Resonator in the Magnetosphere¹

A. V. Guglielmi*, A. S. Potapov**, and C. T. Russell***

* Schmidt Joint Institute of Physics of the Earth, Russian Academy of Sciences,
Bol'shaya Gruzinskaya ul. 10, Moscow, 123810 Russia

e-mail: gugi@uipe-ras.scgis.ru

** Institute of Solar–Terrestrial Physics, Russian Academy of Sciences, Irkutsk, 664033 Russia

e-mail: potapov@iszf.irk.ru

*** Institute of Geophysics and Planetary Physics UCLA, Los Angeles, CA 90095-1567, USA

Received August 7, 2000

Our concern here is to present the idea of the ion cyclotron resonator in the planetary magnetosphere and to discuss briefly the experimental status of the corresponding theory. The resonator confines the ion cyclotron waves to a thin equatorial zone, so that it keeps the wave field from coming into contact with the ionosphere, resulting in a decrease in energy losses. The properties of the resonator are illustrated by adopting a plausible distribution of the magnetic field in the equatorial zone, which yields an expression for the discrete spectrum of the waves just above the gyrofrequency of heavy ions. We show that the resonator is remarkable for many reasons, including the frequency dependence of its size and specific structure of the spectrum. © 2000 MAIK “Nauka/Interperiodica”.

PACS numbers: 94.30.Tz

Important and very much discussed problems center around the electromagnetic ion cyclotron waves in the Earth's magnetosphere. The literature on this subject is quite voluminous (see [1–3] for references). Considerable recent attention has also been focused on the ion cyclotron waves in the magnetospheres of other planets [4]. It is generally agreed that the study of ion cyclotron waves allows us to broaden our conceptions of space plasma physics [5]. The observation of these waves provides the basis for useful practical applications [1].

Up to now, attention has been paid only to traveling ion cyclotron waves (e.g., [6–8]). In this paper, we would like to discuss standing ion cyclotron waves as the discrete eigenmodes of the ion cyclotron resonator (ICR). Our main concern here is to present the idea of the possible existence of such resonators “suspended” in the equatorial zones of planetary magnetospheres. We will show that the physical properties of the ICR are remarkable for many reasons, including the specific structure of the spectrum and the frequency dependence of ICR size. One point generates particular interest; namely, the resonator holds the ion cyclotron waves in the magnetosphere. This keeps the wave field from coming into contact with the ionosphere, resulting in a decrease in energy losses. In this regard, the ICR differs from the familiar Alfvén resonator [5], and it resembles the toroidal magnetosonic waveguide which exists in the equatorial zone of the Earth's magnetosphere [9, 10].

Let us consider the wave equation

$$\frac{d^2 E_{\pm}}{dz^2} + \left[\frac{\omega}{c} n_{\pm}(z, \omega) \right]^2 E_{\pm} = 0, \quad (1)$$

where $n_{\pm}^2 = 1 + \sum \Omega_i^2 / \omega_{Bi}(\omega_{Bi} \mp \omega)$, describing the left-hand ($E_+ = E_x + iE_y$) and right-hand ($E_- = E_x - iE_y$) circularly polarized, low-frequency ($\omega \ll \omega_{Be}$) electromagnetic waves in the framework of the 1D slab plasma model with an external magnetic field \mathbf{B} which points in the z direction. Here, $\omega_{Be} = eB/m_e c$ is the electron gyrofrequency, e is the elementary charge, m_e is the mass of the electron, c is the velocity of light, $\omega_{Bi} = e_i B/m_i c$ is the ion gyrofrequency, e_i and m_i are the charge and mass of the ion, $\Omega_i = (4\pi e_i^2 N_i/m_i)^{1/2}$ is the ion plasma frequency, and N_i is the number density of ions; the summation is made over the ion species; the upper sign in Eq. (1) refers to the ion cyclotron waves, and the bottom sign refers to the helicon waves (or whistlers) [11].

The multicomponent composition of the plasma is essential to the formation of the ICR. We have restricted ourselves to the simplest case of a binary mixture of light ($i = 1$) and heavy ($i = 2$) positive ions for better visualization of the idea. Let us introduce the designations

$$\begin{aligned} \omega_x &= \omega_{B2} [(1 + \eta/\mu)/(1 + \eta\mu)]^{1/2}, \\ \omega_0 &= \omega_{B2} (1 + \eta)/(1 + \eta\mu), \quad \omega_{\infty} = \omega_{B2}, \end{aligned} \quad (2)$$

¹ This article was submitted by the authors in English.

where $\mu = m_1 e_2 / m_2 e_1$, $\eta = \rho_2 / \rho_1$, and $\rho_i = m_i N_i$. It can be shown that the function $n_+^2(\omega)$ has a pole at frequency ω_∞ , and a zero at frequency ω_0 . The opaqueness band ($n_+^2 < 0$) is situated between these two singularities. The crossover frequency ω_x is determined by the relation $n_+^2(\omega_x) = n_-^2(\omega_x)$. It is easy to check that $\omega_\infty < \omega_0 < \omega_x$ for $\mu < 1$. Note that the formulas for ω_x and ω_0 in Eqs. (2) are appropriate only in the case of dense plasma in which $\rho \gg B^2/4\pi c^2$, where $\rho = \rho_1 + \rho_2$.

Suppose that the opaqueness band $\omega_0 - \omega_\infty$ is thick enough. (The physical meaning of this condition will be discussed below.) In addition, let us assume that $\omega_\infty < \omega < \omega_x$ and, furthermore, that the frequencies ω and ω_0 are close together; i.e., $\omega \sim \omega_0$. In such an event, the square of the refractive index for the ion cyclotron waves can be approximated by the equation

$$n_+^2(\omega) = \alpha(\omega - \omega_0), \quad (3)$$

where $\alpha = (\partial n_+^2 / \partial \omega)_0$. The function $\omega_0(z)$ will be assumed to be smoothly slowly varying with a minimum at the point $z = 0$. For example, this takes place in the equatorial zone of the Earth's magnetosphere, since $B(z)$ has a minimum at the equator. In this case, there exist the frequencies $\omega > \omega_0(0)$ and the points $z_- < 0$, $z_+ > 0$ such that $n_+^2(\omega, z_\pm) = 0$ and $n_+^2(\omega, z) > 0$ for $z_- < z < z_+$. Then, over the interval $z_- < z < z_+$, the nontrivial solutions of Eq. (1) exist if and only if the frequencies ω belong to the discrete spectrum ω_s with $s = 0, 1, 2, \dots$. The wave field $E_+(s, z)\exp(-i\omega_s t)$ has the form of a standing ion cyclotron wave with s nodes. In other words, we are concerned with an ICR "suspended" in the magnetosphere.

To simplify the treatment, let us use a parabolic model to approximate the geomagnetic field in the equatorial zone:

$$B(z) = \frac{B_E}{L^3} \left[1 + \frac{9}{2} \left(\frac{z}{R_E L} \right)^2 \right]. \quad (4)$$

Here, B_E is the magnetic field at the Earth's surface, R_E is the Earth's radius, and L is the McIlwain parameter. Rewriting Eq. (1) in view of Eqs. (3) and (4), we obtain

$$\frac{d^2 E_+}{d\zeta^2} + \xi(\omega) [\zeta_0^2(\omega) - \zeta^2] E_+ = 0, \quad (5)$$

where

$$\xi = \frac{2}{\eta} \left[\frac{R_E L \omega (1 + \eta \mu)}{3 c_A (1 - \mu)} \right]^2, \quad (6)$$

$$\zeta_0 = \left[\frac{\omega (1 + \eta \mu)}{\omega_{B2} (1 + \eta)} - 1 \right]^{1/2},$$

and $\zeta = 3z/\sqrt{2} R_E L$. The values η , ω_{B2} , and $c_A = B/(4\pi\rho)^{1/2}$ in Eqs. (6) are taken at the point $\zeta = 0$. The solutions of Eq. (5) are $D_s[(4\xi)^{1/4} \zeta]$ with $\zeta_0^2 \sqrt{\xi} = 2s + 1$, where $D_s(z) = H_s(z/\sqrt{2}) \exp(-z^2/4)$ are the functions of a parabolic cylinder and $H_s(z)$ are the Hermite polynomials. It is natural that $E_+(s, \zeta) \rightarrow 0$ at $\zeta \rightarrow \pm\infty$ in our parabolic model of ICR. This leads to the quantization condition $s = 0, 1, 2, \dots$, so that the equation

$$[\xi(\omega_s)]^{1/2} [\zeta_0(\omega_s)]^2 = 2s + 1 \quad (7)$$

describes the discrete spectrum of ion cyclotron oscillations in the equatorial zone of the magnetosphere.

If $\eta\mu \ll 1$, the roots of Eq. (7) are

$$\omega_s = (1 + \eta)\omega_{B2} + 3\sqrt{2\eta}(c_A/R_E L)(s + 1/2), \quad (8)$$

on the condition that the second term on the right-hand side of Eq. (8) is small in comparison with the first one. This condition holds in the oxyhydrogen magnetospheric plasma, at least at low values of s . We can see that the spectrum is equidistant, but the intervals $\Delta\omega = \omega_{s+1} - \omega_s$ between the adjacent spectral lines

$$\Delta\omega = 3\sqrt{2\eta}c_A/R_E L \quad (9)$$

are much smaller than the frequency $\omega_{s=0}$ of the fundamental harmonic. It is well to bear in mind that this result has been obtained in the dissipation-free limit. There can be little doubt that a natural broadening of the spectral lines in a real plasma causes a flattening of the ICR spectrum. This has led us to believe that the gap

$$\delta\omega = \eta\omega_{B2} + 3\sqrt{\eta/2}c_A/R_E L \quad (10)$$

between the gyrofrequency of heavy ions ω_{B2} and the fundamental frequency $\omega_{s=0}$ is of greater interest for the experimental study of ICR than $\Delta\omega$. Likewise, the ICR size

$$\Delta z = 2\eta^{1/4} [(c_A R_E L / \omega_{B2})(s + 1/2)]^{1/2} \quad (11)$$

is of immediate interest to the experimentalist. Here, $\Delta z = z_+ - z_-$, $z_\pm = \pm(\sqrt{2}/3)\zeta_0 R_E L$, $\eta \ll 1$. We notice that the size of the resonant region is minimal for the fundamental harmonic.

The small size of the ICR is noteworthy. By way of illustration, let us assume that $L = 7.48$, $\rho_{O^+} = 0.21\rho$, $c_A = 2 \times 10^7$ cm s⁻¹, as measured by the ISEE-1 satellite [12]. Then $(\Delta z)_{\min} = 4.6 \times 10^8$ cm, which corresponds to the interval of geomagnetic latitudes between $\pm 2.3^\circ$ (see Eq. (11) for $s = 0$). The ISEE-1 satellite recorded the ion cyclotron waves in the frequency band from 0.1 to 0.2 Hz just above the O⁺ cyclotron frequency at a distance of 6.5° from the geomagnetic equator. According to Eq. (11), this means that the satellite was liable to detect the standing waves in ICR if and only if $s \geq 3$. The corresponding gap between the gyrofrequency of

oxygen ions at the equator and the lower boundary of the wave spectrum equals 28 mHz. It is reasonable to say that this estimate does not contradict the ISEE-1 observations (see the ion cyclotron wave spectrum in [12], Fig. 10a).

There are a number of spikes in the spectra observed by the ISEE-1 and 2 satellites. However, the interval between adjacent spikes is of the order of 10 mHz, which is several times greater than follows from Eq. (9). We have reanalyzed the satellite data and concluded that, in any case, we could not resolve the predicted line spacing with the 4-mHz spectral resolution of the ISEE-1 and 2. Thus, while we feel that the idea of magnetospheric ICR is plausible, we have not yet confirmed it experimentally in full measure. We urge other researchers to look for the quasi-discrete structure of spectra when examining the ion cyclotron waves near the magnetic equator.

In conclusion, let us take up the applicability of the theory. Generally, this is a widespread problem, but here we restrict the discussion to the elementary aspects, namely, to the foregoing conditions of applicability of Eqs. (3)–(5). It has been assumed that the value $\omega_0 - \omega_\infty$ is large enough, so that the poles and zeros of $n_+^2(z)$ are far apart. Physically, this means that we are in a position to neglect the energy leakage from the ICR due to tunnelling of the ion cyclotron waves through the opaqueness bands disposed bilaterally just beyond the turning points z_- and z_+ . At low latitudes, the tunnel effect is negligibly small when $\Omega_2 \gg c/R_E L$ (e.g., see [2], where the tunnel effect was considered at high latitudes). This sufficient condition holds in the case of the satellite observations cited above.

One possible mechanism of energy leakage from the ICR is associated with linear mode conversion. The essence of this process is that the left-hand ion cyclotron waves may couple to the right-hand whistler waves due to inhomogeneity of the medium [13]. Without going into detail, we simply note that the coupling between the modes is especially strong in vicinity of the crossover points z_x , which are the roots of the equation $n_+(z_x, \omega) = n_-(z_x, \omega)$. Needless to say, the concept

of mode conversion, as applied to ICR, needs further consideration. For our present purposes, it will suffice to mention that n_+ and n_- as functions of z have a maximum and minimum at $z = 0$, respectively, so that in the ICR the crossover points z_x are completely absent if $\omega < \omega_x$, since $n_+(0, \omega) < n_-(0, \omega)$ under this condition. It is easy to check that the spectrum described by Eq. (8) satisfies the condition $\omega_s < \omega_x$ at least at low values of s . The last remark pertains equally to the parabolic model for the geomagnetic field, which is appropriate in the limit of small Δz [see Eqs. (4) and (11)].

This work was supported in part by the Russian Foundations for Basic Research, project no. 00-05-64546.

REFERENCES

1. A. V. Guglielmi, *Usp. Fiz. Nauk* **158**, 605 (1989) [*Sov. Phys. Usp.* **32** (8), 678 (1989)].
2. A. V. Guglielmi and O. A. Pokhotelov, *Geoelectromagnetic Waves* (Institute of Physics Publ., Bristol, 1996).
3. J. Kangas, A. Guglielmi, and O. Pokhotelov, *Space Sci. Rev.* **83**, 435 (1998).
4. C. T. Russell, M. G. Kivelson, K. K. Khuranda, *et al.*, *Planet. Space Sci.* **47**, 143 (1999).
5. M. G. Kivelson and C. T. Russell, *Introduction to Space Physics* (Cambridge Univ. Press, Cambridge, 1995).
6. J. LaBelle and R. A. Treumann, *J. Geophys. Res.* **97**, 13789 (1992).
7. R. M. Thorne and R. B. Horne, *J. Geophys. Res.* **102**, 14155 (1997).
8. A. Guglielmi, K. Hayashi, R. Lundin, and A. Potapov, *Earth, Planets Space* **51**, 1297 (1999).
9. A. V. Guglielmi, *Zh. Éksp. Teor. Fiz.* **12**, 35 (1970) [*JETP Lett.* **12**, 25 (1970)].
10. C. T. Russell, R. E. Holzer, and E. J. Smith, *J. Geophys. Res.* **75**, 755 (1970).
11. V. L. Ginzburg, *Propagation of Electromagnetic Waves in a Plasma* (Nauka, Moscow, 1967; Pergamon, New York, 1971).
12. B. J. Fraser, J. C. Samson, Y. D. Hu, *et al.*, *J. Geophys. Res.* **97**, 3063 (1992).
13. K. G. Budden, *The Propagation of Radio Waves* (Cambridge Univ. Press, Cambridge, 1985).

Structural Transition in Liquid Cobalt

V. I. Lad'yanov*, A. L. Bel'tyukov, K. G. Tronin, and L. V. Kamaeva

Physicotechnical Institute, Ural Division, Russian Academy of Sciences, ul. Kirova 132, Izhevsk, 426000 Russia

Udmurt State University, Krasnoarmeiskaya ul. 71, Izhevsk, 426034 Russia

* e-mail: las@las.fti.udmurtia.su

Received July 27, 2000

The temperature dependence of kinematic viscosity of liquid cobalt in the range 1490–1700°C and the influence of the degree of cobalt overheating on its overcooling were studied by viscometry and differential thermal analysis. It was found that liquid cobalt undergoes a structural transition near 1595°C, which manifests itself as a sharp change in the viscosity and the activation energy for viscous flow at this temperature and is accompanied by a considerable increase in crystallization ability. © 2000 MAIK “Nauka/Interperiodica”.

PACS numbers: 66.20.+d; 64.70.Ja

At present, the problem of possible structural transitions in fluids caused by temperature- or pressure-induced changes in the short-range order is being actively discussed [1, 2]. The presence of thermal structural transitions manifesting themselves as anomalies in the property polyterms and, to a lesser extent, in the diffraction data was demonstrated for liquid metals in works [3–5]. Nevertheless, the mechanism of such transitions still remains to be clarified [1, 5].

In this work, the possibility of structural transition in liquid cobalt was studied by viscometry. It is known that crystalline cobalt undergoes a polymorphic $\beta \longleftrightarrow \alpha$ (fcc \longleftrightarrow hcp) transformation at 417°C. It relates to the first-order transition and is accompanied by the volume $(\Delta V/V)_{\beta \rightarrow \alpha} = 0.36\%$ and thermal $\Delta Q_{\beta \rightarrow \alpha} = 440$ J/mol effects and a jump in physical properties at the transition point [6]. To date, no anomalies have been observed in the property polyterms of liquid cobalt. Nevertheless, the question of its post-melting structure remains an open question. According to [7], the short-range order in liquid cobalt is similar to the high-temperature crystalline state and virtually does not change with a temperature increase. However, the authors of [8] argue that the structure of Co changes upon melting to realize a bcc-like atomic ordering in the liquid state.

The kinematic viscosity of liquid type K1 cobalt was determined by the method of damped torsional vibrations in BeO crucibles in an atmosphere of purified helium after preliminary evacuation of the working volume of the setup to 10^{-2} Pa and heating of the furnace to 1000°C. Measurements were made in the regime of stepped temperature change with a step of 10–15 K after isothermic annealing for 30 min. Temperature was determined by a tungsten–rhenium thermocouple with an accuracy of ± 10 K and maintained at a constant level to within ± 0.5 K using a VRT-3 instrument. In the measurements, the vibration parameters

were detected optically using a ruby laser and a precision photodetector with a time delay no greater than 100 ns. The methodology of the measurements and statistical–probabilistic processing of the experimental data is described in detail in [9]. The error analysis indicated that, at a fiducial probability of 0.95, the most probable error in determining the absolute values of viscosity in an individual experiment did not exceed 1% at a total error no larger than 1.5%.

The experimental viscosity polyterm of liquid cobalt is presented in Fig. 1a. An analysis of the temperature dependence suggests that the Co viscosity undergoes an anomalous sharp decrease (by about 10%) near $t^* = 1595^\circ\text{C}$. The character of the temperature dependence of ν is exponential before and after t^* , but the activation energy for viscous flow changes significantly (from 44.5 to 75.1 kJ/mol):

$$\nu = 3.156 \times 10^{-8} \exp[5360.7/T],$$

at $1492 < t < 1595^\circ\text{C}$;

$$\nu = 0.406 \times 10^{-8} \exp[9034.1/T],$$

at $1595 < t < 1700^\circ\text{C}$.

The reliability of the observed anomaly is also evident from the increased scatter of the experimental points in the vicinity of t^* . The temperature dependence of the parameter ξ , equal to the standard deviation normalized to the mean value (the degree of viscosity instability [10]),

$$\xi = \frac{1}{\bar{\nu}} \left[\sum (v_i - \bar{\nu})^2 / m(m-1) \right]^{1/2}$$

is presented in Fig. 1b. It shows a maximum at 1590°C.

Another feature of the viscosity polyterms of liquid cobalt is that they show hysteresis upon heating above

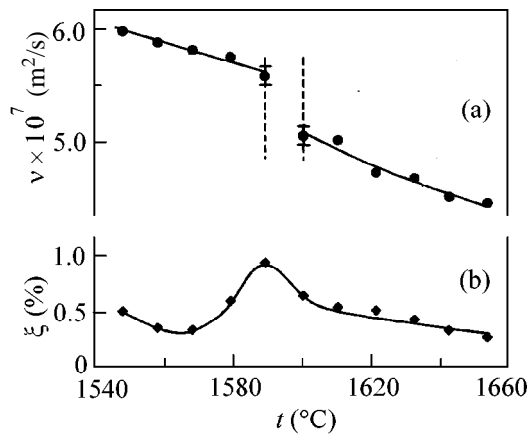


Fig. 1. Temperature dependence of (a) viscosity and (b) degree of its instability in liquid cobalt.

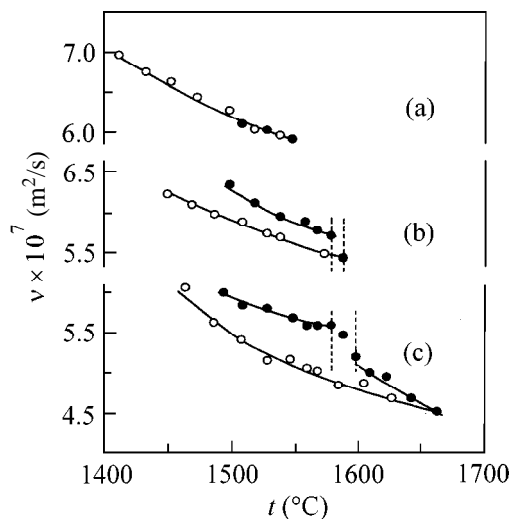


Fig. 2. Influence of temperature on the viscosity of liquid cobalt: (●) heating and (○) cooling.

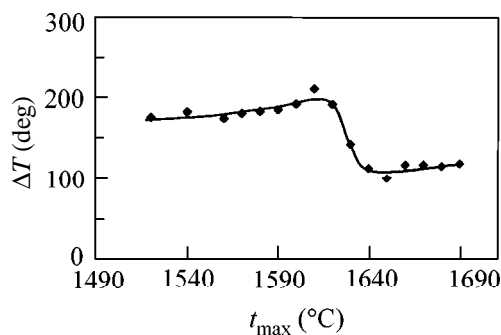


Fig. 3. Overheating of liquid cobalt as a function of maximal heating temperature.

t^* followed by cooling. The $v(t)$ curves obtained for different maximal heating temperatures are shown in Fig. 2. The samples were heated to a certain temperature, annealed for 30 min, and then cooled. The viscosity was measured starting from the melting point of the

sample down to its crystallization. It is seen in Fig. 2 that if the maximum temperature of liquid cobalt does not exceed t^* , the heating and cooling curves coincide (the hysteresis is absent). Heating of the melt above 1595°C (i.e., above the anomaly temperature) gives rise to a sharp change in the viscosity near t^* . This change is not reproduced upon cooling even after a slight overheating above t^* , bringing about hysteresis in the v polyterm for the direct and reverse runs.

Differential thermal analysis showed a significant overcooling (ΔT) of liquid cobalt at a low cooling rate and a decrease in ΔT upon an increase in the maximal heating temperature (Fig. 3). A sample of mass 1 g was heated to a certain temperature, annealed for 20 min, and cooled. The rate of changing the temperature was 100 K/min. The melting and crystallization temperatures of cobalt and its overcooling were determined from the DTA curves. It is seen from Fig. 3 that the ΔT value decreases tangibly upon heating liquid Co higher than 1610°C , in good agreement with the data obtained by measuring viscosity for massive samples (~20 g).

The anomalous change in viscosity near 1595°C , as well as the increased scatter of experimental points and the increase in crystallization ability (Figs. 1, 3), is evidence for a possible structural transition in liquid cobalt near this temperature. In character, it is analogous, e.g., to the transition in liquid copper [5]. According to the X-ray structural data [8, 11], the postmelting short-range order in both cobalt and copper is different from the atom packing in their crystal phases. A further increase in temperature only slightly affects the X-ray pattern, indicating that the basic short-range order persists in the liquid state. One can thus assume that the structural change in liquid cobalt near 1595°C proceeds, as in copper, through the mechanism of one-dimensional cluster polymorphism as a result of an abrupt change in one of the parameters of the lattice of tetragonal-type clusters [12].

A sharp increase in the viscosity instability of the melt near the temperature of structural transition can be explained by the presence of several (at least two) energetically close states that are separated by energy barriers and have different short-range orders at this temperature. When the energy of thermal fluctuations becomes close to the energy barrier, the number of random transition trajectories between these states increases, leading to the increase in the instability of the whole system.

REFERENCES

1. V. Brazhkin, S. Popova, and R. Voloshin, *High-Pressure Res.* **15**, 267 (1997).
2. V. V. Brazhkin, R. N. Voloshin, A. G. Lyapin, and S. V. Popova, *Usp. Fiz. Nauk* **169**, 1035 (1999).
3. B. A. Baum, G. A. Khasin, G. V. Tyagunov, *et al.*, *Liquid Steel* (Metallurgiya, Moscow, 1984).
4. Yu. A. Bazin, V. M. Zamyatin, *et al.*, *Izv. Vyssh. Uchebn. Zaved., Chern. Metall.* **5**, 28 (1985).

5. V. I. Lad'yanov and A. L. Bel'tyukov, *Pis'ma Zh. Éksp. Teor. Fiz.* **71**, 128 (2000) [*JETP Lett.* **71**, 89 (2000)].
6. B. I. Nikolin, *Multilayer Structures and Polytypism of Metal Alloys* (Naukova Dumka, Kiev, 1984).
7. O. I. Slukhovskii and A. V. Romanova, *Metallofizika* **13** (4), 55 (1991).
8. E. A. Klimenkov, P. V. Gel'd, *et al.*, *Dokl. Akad. Nauk SSSR* **230**, 71 (1976) [*Sov. Phys. Dokl.* **21**, 507 (1976)].
9. S. V. Logunov and V. I. Lad'yanov, *Rasplavy* **3**, 63 (1996).
10. V. I. Lad'yanov, S. V. Logunov, and S. V. Pakhomov, *Metally* **5**, 20 (1998).
11. N. A. Vatolin and É. A. Pastukhov, *Diffraction Studies of the Structures of High-Temperature Melts* (Nauka, Moscow, 1980).
12. I. A. Novokhatskii, V. I. Arkharov, and V. I. Lad'yanov, *Dokl. Akad. Nauk SSSR* **267** (2), 367 (1982) [*Sov. Phys. Dokl.* **27**, 963 (1982)].

Translated by V. Sakun

Dimensionality of a System of Exchange-Coupled Grains and Magnetic Properties of Nanocrystalline and Amorphous Ferromagnets

R. S. Iskhakov, S. V. Komogortsev, A. D. Balaev, and L. A. Chekanova

Kirenskiĭ Institute of Physics, Siberian Division, Russian Academy of Sciences, Akademgorodok, Krasnoyarsk, 660036 Russia

Received July 31, 2000

Characteristics of random magnetic anisotropy in ferromagnetic films of amorphous $\text{Co}_{90}\text{P}_{10}$ and nanocrystalline $\text{Ni}_{75}\text{C}_{25}$, $\text{Fe}_{80}\text{B}_4\text{C}_{16}$, and $\text{Co}_{80}\text{C}_{20}$ alloys and also in multilayer films $[\text{Co}_{93}\text{P}_7(x)/\text{Pd}(14 \text{ \AA})]_{20}$ and $[\text{Co}_{90}\text{P}_{10}(x)/\text{Pd}(14 \text{ \AA})]_{20}$ obtained by various technological procedures were studied experimentally. It was found that the spatial dimensionality (d) of the system of ferromagnetically coupled grains ($2R_c$) in the materials under study determined the exponent in the power dependence of the approach of magnetization to saturation in the region of fields $H < 2A/MR_c^2$. The dependence $\Delta M \sim H^{-1/2}$ was observed for nanocrystalline and amorphous films with a three-dimensional grain arrangement. The approach to saturation in multilayer films with a two-dimensional grain arrangement in an individual magnetic layer follows the law $\Delta M \sim H^{-1}$. The main micromagnetic characteristics of random anisotropy, such as the ferromagnetic correlation radius R_f and the average anisotropy $\langle K \rangle$ of a ferromagnetic domain with a size of $2R_f$, were determined for multilayer Co/Pd films. Correlation was found between the coercive field and these characteristics of random anisotropy. © 2000 MAIK “Nauka/Interperiodica”.

PACS numbers: 75.70.Ak; 75.30.Gw; 75.50.Kj

Considerable success in understanding the magnetic structure and soft magnetic properties of amorphous and nanocrystalline ferromagnets has recently been achieved based on the notions of random magnetic anisotropy (RMA). Thus, it was shown experimentally in [1] that soft magnetic properties of materials with a grain size $2R_c$ smaller than the exchange correlation length $\delta = (A/K)^{1/2}$ depend on R_c as follows: the coercive force $H_c \sim R_c^6$, and the initial permeability $\mu \sim R_c^{-6}$. These relationships for soft magnetic properties are conditioned by chaos in the direction of local magnetic anisotropy K and by the possibility of describing the magnetic structure of such materials by a set of weakly coupled magnetic domains with the size $2R_f$ and the average domain anisotropy

$$\langle K \rangle = \frac{K}{\sqrt{N}} = K \left(\frac{R_c}{R_f} \right)^{d/2}. \quad (1)$$

Simple theoretical estimates [1–3] give the following equations for the average anisotropy of a magnetic domain and the ferromagnetic correlation radius:

$$\langle K \rangle \sim K(R_c/\delta)^{2d/(4-d)}, \quad (2)$$

$$R_f \sim \delta(\delta/R_c)^{d/(4-d)} \quad (2')$$

depending on the spatial dimensionality d of the arrangement of the grain system $2R_c$. For a three-

dimensional arrangement of exchange-coupled grains ($d = 3$), according to Eqs. (2) and (2'), we obtain $\langle K \rangle \sim R_c^6$, $R_f \sim R_c^{-3}$.

The main micromagnetic properties of amorphous and nanocrystalline ferromagnets $\langle K \rangle$ and R_f , as well as the local anisotropy characteristics K and R_c , can be directly determined from magnetization curves in the region of approach to saturation. The ideas of these measurements are as follows. The approach of magnetization to saturation in sufficiently high magnetic fields ($H > 2A/MR_c^2$) is described by the Akulov law for a polycrystal [4]

$$\frac{\Delta M}{M_s} = \left(\frac{2D^{1/2}K}{HM_s} \right)^2, \quad (3)$$

independent of the dimensionality d of the grain arrangement. Here, D is a numerical symmetry factor (see [5]), and the condition on the field H is determined by the inequality $R_c > R_H$, where the magnetic correlation radius $R_H = (2A/M_H)^{1/2}$. In fields below the so-called exchange field $H_{ex} = 2A/MR_c^2$, the inequality $R_H > R_c$ is fulfilled. Substituting $\langle K \rangle$ obtained according to Eq. (1) into the Akulov law, with regard to effective averaging over grains within the region $2R_H$, one can

obtain the following dependence of magnetic moment scattering on the field:

$$\frac{\Delta M}{M_s} = \left(\frac{2D^{1/2} \langle K \rangle}{HM_s} \right)^{(4-d)/2} \equiv \left(\frac{R_H}{R_f} \right)^{4-d}. \quad (4)$$

Thus, an analysis of the magnetization curve $M(H)$ throughout the entire range of magnetic fields allows the values of K , R_c , R_f , and $\langle K \rangle$ to be measured and the dimensionality of the system d to be determined.

The law of approach to saturation for isotropic (three-dimensional) inhomogeneities was theoretically derived in [5] based on the canonical expansion of random functions. The approach to saturation in ferromagnets with two-dimensional anisotropy inhomogeneities was theoretically considered in [6, 7], and Eq. (4) for inhomogeneities with an arbitrary dimensionality was actually obtained in [8].

Equations (1), (2), and (4) indicate that the dimensionality of a system of exchange-coupled grains determines the character of the approach of magnetization to saturation in the region $R_H > R_c$. Hence, it also determines the level of soft magnetic properties of amorphous and nanocrystalline ferromagnets through $\langle K \rangle$. This work is devoted to an experimental study of the effects considered above.

Experiment. This work reports the results of studying magnetization curves for films of amorphous $\text{Co}_{90}\text{P}_{10}$ (thickness $t = 2000 \text{ \AA}$) and nanocrystalline $\text{Co}_{80}\text{C}_{20}$ ($t = 1200 \text{ \AA}$), $\text{Fe}_{80}\text{B}_4\text{C}_{16}$ ($t = 500 \text{ \AA}$), and $\text{Ni}_{75}\text{C}_{25}$ ($t = 600 \text{ \AA}$) alloys and also for multilayer films $[\text{Co}_{93}\text{P}_7(x)/\text{Pd}(14 \text{ \AA})]_{20}$ (where $x = 30 \text{ \AA}$, 45 \AA , 55 \AA , and 80 \AA) and $[\text{Co}_{90}\text{P}_{10}(x)/\text{Pd}(14 \text{ \AA})]_{20}$ (where $x = 20 \text{ \AA}$, 45 \AA , 60 \AA , 65 \AA , and 115 \AA) obtained by various technological procedures [5, 9, 10]. Small additions of phosphorus in the cobalt layers of Co/Pd multilayer films were used for obtaining ferromagnetic layers differing in the short-range structure. In Co(P) layers prepared by the chemical deposition technique, an fcc structure is obtained at concentrations of 5–8 at. % P and an amorphous state of Co layers is obtained above 9 at. % P [5].

Magnetic measurements were carried out using a vibrating-coil magnetometer with a superconducting solenoid in fields up to 30 kOe and temperatures from 4.2 to 200 K. The film substrate was measured separately, and its contribution to the total signal ($\sim 1\%$) was subtracted.

Results and discussion. Figure 1 shows high-field regions of magnetization curves $M(H)$ for films of nanocrystalline and amorphous alloys. The thicknesses of the films for which these curves were measured considerably exceeded the sizes of the constituent grains or clusters ($2R_c \sim 100 \text{ \AA}$). Thus, magnetic domains with a size of $2R_f$ were arranged in these films as grains with a size of $2R_c$ in a three-dimensional way. In this case, according to Eq. (4), the approach of magnetization to saturation in these materials must follow the power

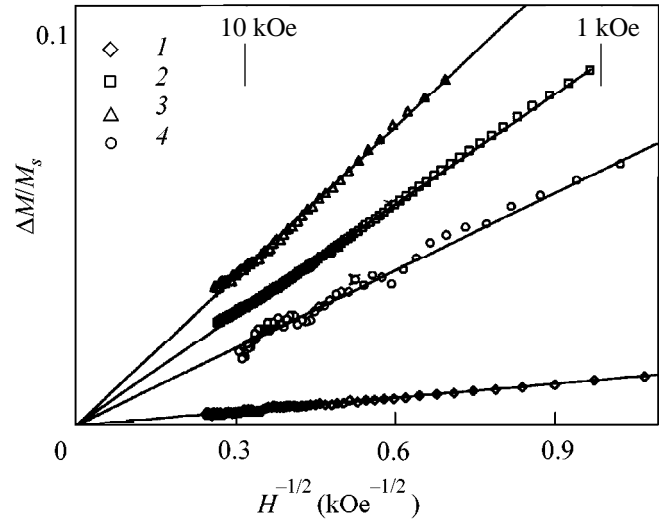


Fig. 1. High-field regions of magnetization curves $M(H)$ for amorphous and nanocrystalline films with $d = 3$: (1) $\text{Co}_{80}\text{C}_{20}$ ($t = 1200 \text{ \AA}$), (2) $\text{Co}_{90}\text{P}_{10}$ ($t = 2000 \text{ \AA}$), (3) $\text{Fe}_{80}\text{B}_4\text{C}_{16}$ ($t = 500 \text{ \AA}$), and (4) $\text{Ni}_{75}\text{C}_{25}$ ($t = 600 \text{ \AA}$).

dependence $\Delta M/M_s \sim H^{-1/2}$. The rectilinear regions on the coordinates $(\Delta M/M_s, H^{-1/2})$ in Fig. 1 actually indicate that this power dependence of the approach of magnetization to saturation is actually fulfilled in these samples within the range of fields of 1–10 kOe. According to Eq. (4), this fact points to a three-dimensional arrangement of exchange-coupled grains.

Figure 2 displays magnetization curves for multilayer Co(P)/Pd films. The sizes of the grains or clusters that compose individual magnetic layers of these films are of the order of the thickness of such layers. The filling of an individual layer along the height of one grain leads to the formation of a two-dimensional system of ferromagnetically coupled grains in these films. An essential point here is the fact that the exchange coupling between grains within an individual layer considerably exceeds the coupling between neighboring individual layers (by at least an order of magnitude) studied in [10]. For the tasks of this work, the multilayer arrangement was only a way of accumulating the experimental signal for studying the small effect of magnetic moment scattering in the vicinity of saturation in ultrathin layers by the induction method. According to Eq. (4), the approach of magnetization to saturation in a two-dimensional arrangement of grains corresponds to the law $\Delta M/M_s \sim H^{-1}$. The rectilinear regions in the high-field magnetization curves of multilayer Co(P)/Pd films with both amorphous and nanocrystalline Co layers on the coordinates $(\Delta M/M_s H^{-2}, H)$ point to the fulfillment of the dependence $\Delta M/M_s \sim H^{-1}$ in the range of fields up to 20–25 kOe.

As was indicated above, the region of fields used for determining the system dimensionality d from the

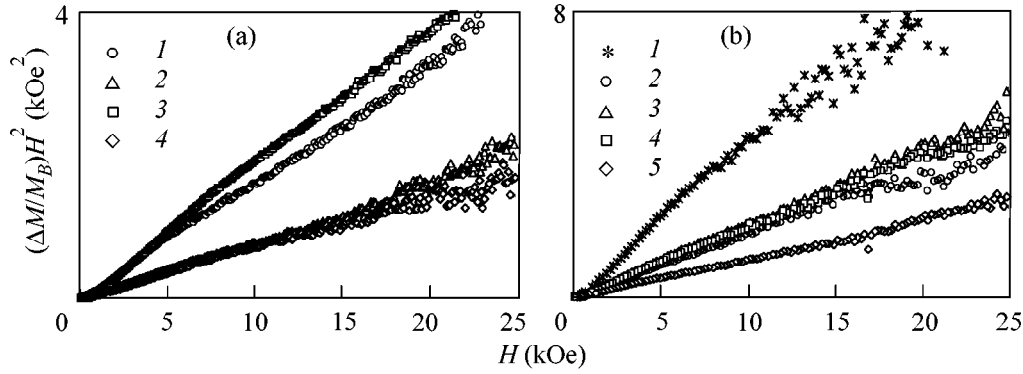


Fig. 2. High-field regions of magnetization curves $M(H)$ for multilayer Co/Pd films: (a) $[\text{Co}_{93}\text{P}_7(x)/\text{Pd}(14 \text{ \AA})]_{20}$, $x = (1) 30$, (2) 45, (3) 55, and (4) 80 \AA ; (b) $[\text{Co}_{90}\text{P}_{10}(x)/\text{Pd}(14 \text{ \AA})]_{20}$, $x = (1) 20$, (2) 45, (3) 60, (4) 65, and (5) 115 \AA .

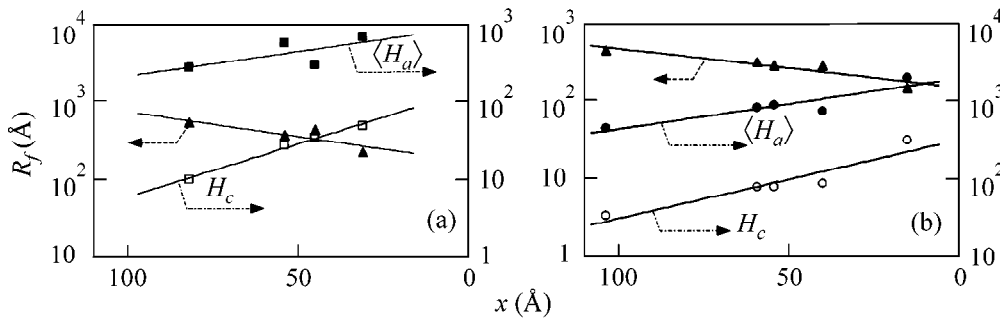


Fig. 3. Micromagnetic parameters $\langle H_a \rangle$ and R_f and coercive force H_c for multilayer Co/Pd films: (a) $[\text{Co}_{93}\text{P}_7(x)/\text{Pd}(14 \text{ \AA})]_{20}$ and (b) $[\text{Co}_{90}\text{P}_{10}(x)/\text{Pd}(14 \text{ \AA})]_{20}$.

observed dependence of the moment on the external field has an upper limit equal to the exchange field $H_{ex} = 2A/MR_c^2$. In order to estimate the value of H_{ex} , it is necessary to find the exchange interaction constant A . This constant, for the films studied in this work, was calculated from the measured low-temperature thermomagnetic curves (the Bloch law $T^{3/2}$ [9]). For the amorphous and nanocrystalline films studied in this work, the values of H_{ex} were found to be ~ 10 – 20 kOe. Therefore, the dependence of ΔM on H for these films also exhibited a crossover (transition from $\Delta M \sim H^{-1/2}$ to $\Delta M \sim H^{-2}$). This allowed us to measure H_{ex} directly, to calculate R_c , and to measure the value of K . For multilayer films, we estimated $H_{ex} \sim 20$ – 30 kOe, which is close to the value of the maximal fields used in our experiment.

Note that the law of approach to saturation $\Delta M/M_s \sim H^{-1/2}$ predicted in [5] is well known to magnetologists and is widely used for interpreting data on the approach of magnetization to saturation in amorphous and nanocrystalline alloys [11–15]. Here, a change of the exponent in the power dependence of the approach to saturation in nanocrystalline and amorphous materials with the dimensionality $d = 2$ was found experimentally. The results presented in Figs. 1 and 2 are

described by Eq. (4). They demonstrate that the exponent in the power dependence of curves describing the approach of magnetization to saturation is not associated with the short-range order in the ferromagnetic material. It is determined only by such a substructure parameter as the dimensionality d of the arrangement of exchange-coupled grains. The fundamental possibility of experimentally determining the spatial dimensionality of the arrangement of a system of ferromagnetically coupled grains (in the general case, this dimensionality can be a noninteger number) is of great importance for the physics and technology of magnetic materials.

The slopes of the rectilinear regions in Figs. 1 and 2 characterize the mean-square fluctuations of the field of anisotropy $\langle K \rangle$ averaged over the region within which the magnetic moments of the grains are exchange-correlated: $D^{1/2}\langle H_a \rangle = 2D^{1/2}\langle K \rangle/M = D^{1/2}H_a/N^{1/2}$, where N is the number of structural units $2R_c$ incorporated into a magnetic domain. The magnetic correlation radius R_f can be estimated from Eq. (2) or from the following equation: $R_f = (AD^{1/2}\langle K \rangle)^{1/2}$. The values of $\langle H_a \rangle$ and R_f calculated in such a way for multilayer Co/Pd films differing in thickness of the ferromagnetic layer are given in Fig. 3 (the coefficient D was set equal to $1/15$ [5]). The coercive forces H_c of these films are also given

here. A detailed analysis of the dependence of the micromagnetic parameters $\langle H_a \rangle$ and R_f in these films on the magnetic layer thickness is a subject of a separate comprehensive investigation [the observed variations of these quantities within a given thickness range are due to variations of both the magnetic constants (A , K) and structural parameters (R_c , d), which nonlinearly enter into Eqs. (1) and (2)]. It is important to emphasize here the correlation of the coercive force H_c and the average anisotropy of the magnetic domain $\langle H_a \rangle$. Because there is no strong interaction between magnetic domains, the latter value represents the effective anisotropy of these materials. The correlation observed between the effective anisotropy and the coercivity of nanocrystalline and amorphous ferromagnets with a two-dimensional arrangement of magnetically coupled grains indicates that magnetic anisotropy fluctuations play the main role in the formation of soft magnetic properties in such systems.

The authors are grateful to V.S. Zhigalov for the samples of nanocrystalline alloys presented for this study, to V.A. Ignatchenko for useful discussions and interest in this work, and to S.A. Karpenko for help with the work.

REFERENCES

1. G. Herzer, IEEE Trans. Magn. **26**, 1397 (1990).
2. R. Alben, J. J. Becker, and M. C. Chi, J. Appl. Phys. **49**, 1653 (1978).
3. R. S. Iskhakov, S. V. Komogortsev, A. D. Balaev, *et al.*, in *Proceedings of XVII International School and Workshop on New Magnetic Materials for Microelectronics, Moscow, Russia, 2000* (Moscow, 2000), p. 540.
4. N. S. Akulov, Z. Phys. **69**, 278 (1931).
5. V. A. Ignatchenko, R. S. Iskhakov, and G. V. Popov, Zh. Éksp. Teor. Fiz. **82**, 1518 (1982) [Sov. Phys. JETP **55**, 878 (1982)].
6. E. M. Chudnovsky, J. Magn. Magn. Mater. **40**, 21 (1983).
7. A. G. Chernykh, P. P. D'yachuk, and V. B. Kruglov, Izv. Akad. Nauk SSSR, Ser. Fiz. **53**, 622 (1989).
8. V. A. Ignatchenko and R. S. Iskhakov, Fiz. Met. Metall-oved., No. 6, 75 (1992).
9. R. S. Iskhakov, S. V. Komogortsev, S. V. Stolyar, *et al.*, Pis'ma Zh. Éksp. Teor. Fiz. **70**, 727 (1999) [JETP Lett. **70**, 736 (1999)].
10. R. S. Iskhakov, Zh. M. Moroz, E. E. Shalygina, *et al.*, Pis'ma Zh. Éksp. Teor. Fiz. **66**, 487 (1997) [JETP Lett. **66**, 517 (1997)].
11. J. F. Löffler, J. P. Meier, B. Doudin, *et al.*, Phys. Rev. B **57**, 2915 (1998).
12. L. Thomas, J. Tuaillon, J. P. Perez, *et al.*, J. Magn. Magn. Mater. **140–144**, 437 (1995).
13. M. W. Grinstaff, M. B. Salamon, and K. S. Suslick, Phys. Rev. B **48**, 269 (1993).
14. J. Tejada, B. Martínez, A. Labarta, *et al.*, Phys. Rev. B **42**, 898 (1990).
15. M. J. O'Shea, K. M. Lee, and A. Fert, J. Appl. Phys. **67**, 5769 (1990).

Translated by A. Bagatur'yants

Depolarization of a Neutron Beam in Laue Diffraction by a Noncentrosymmetric Crystal

V. V. Voronin, E. G. Lapin, S. Yu. Semenikhin, and V. V. Fedorov*

Konstantinov Institute of Nuclear Physics, Russian Academy of Sciences, Gatchina, Leningrad region, 188350 Russia

* e-mail: vfedorov@hep486.pnpi.spb.ru

Received August 1, 2000

The depolarization of a neutron beam executing Laue diffraction in a thick (~3.5 cm) noncentrosymmetric α -quartz crystal is observed. This effect was predicted by us earlier and suggested for measuring the electric dipole moment (EDM) of a neutron. The effect is due to an interaction of the magnetic moment of a moving neutron with a strong crystal electric field, as a result of which the neutron spin rotates in opposite directions for waves of two types excited in the crystal. The effect is studied for neutron diffraction by a system of crystallographic (110) planes at Bragg angles close to $\pi/2$, up to 87° . It is shown that, for a crystal of thickness $L = 3.5$ cm, a direct beam initially polarized along the reciprocal lattice vector becomes depolarized upon diffraction, irrespective of the value of Bragg angle, whereas the beam polarized perpendicular to the diffraction plane retains its polarization. The $E\tau$ value determining the sensitivity of the method to EDM is experimentally estimated. © 2000 MAIK "Nauka/Interperiodica".

PACS numbers: 14.20.Dh; 13.40.Em; 61.12.Ex

1. In [1], a new method of determining the electric dipole moment (EDM) of a neutron was proposed. It is based on the fact that the phase of pendellosung fringes depends on the orientation of a neutron spin diffracted by a crystal without a symmetry center. This dependence arises because the diffracted neutron, when passing a distance of several centimeters in a noncentrosymmetric crystal, is subjected to a strong crystal electric field \mathbf{E}_g (higher than 10^8 V/cm), which was predicted and measured in [2, 3]. The value of $(2.1 \pm 0.2) \times 10^8$ V/cm [2, 3] experimentally obtained for the crystal field of α -quartz for the (110) plane coincides, to within experimental error, with its calculated value. Such fields are more than four orders of magnitude higher than the fields presently used in the most sensitive magnetic resonance method of determining EDM using ultracold neutrons (the UCN method) [4–6]. However, fields as high as these are still insufficient for enhancing the accuracy of EDM measurements. It is essential that the suggested method allows the neutron residence time τ in the crystal electric field to be increased for Bragg angles θ_B close to $\pi/2$.¹ The use of such angles may increase sensitivity by more than an order of magnitude [1]. The reason is that the EDM effect in Laue diffraction (e.g., the pendellosung phase shift upon \mathbf{E}_g -oriented spin flip) is determined by [1]

$$\Delta\varphi^D = \frac{4DE_gL}{\hbar v_{\parallel}} = \frac{4DE_gL}{v \cos\theta_B} \approx \frac{1}{\pi/2 - \theta_B}. \quad (1)$$

¹ The neutron residence time in the crystal was directly measured in [7].

Here, D is the EDM of a neutron, $v_{\parallel} = v \cos\theta_B$ is the mean velocity of neutron propagation along the crystallographic planes, and v is the neutron velocity. For $\theta_B \rightarrow \pi/2$, $\cos\theta_B \approx \pi/2 - \theta_B$. It is also essential that the interfering effect of Schwinger interaction be independent of the Bragg angle:

$$\Delta\varphi^S = \frac{4\mu H_g^S L}{\hbar v_{\parallel}} = 2\mu_n \frac{eE_g L}{m_p c^2}. \quad (2)$$

Here, $\mathbf{H}_g^S = [\mathbf{E}_g \times \mathbf{v}_{\parallel}]/c$, $\mu_n = -1.9$ is the neutron magnetic moment in nuclear magnetons, L is the crystal thickness, m_p is the proton mass, and c is the speed of light.

However, as the Bragg angle increases and approaches a right angle, the frequency of pendellosung beats increases, so that at a certain value of the Bragg angle the angular period of pendellosung oscillations becomes smaller than the Bragg diffraction width. In this situation, the experimental scheme used in [2, 3] for measuring electric fields becomes inapplicable because of the too high frequency of the pendellosung oscillations around the Bragg angle. For this reason, it was first suggested to measure the pendellosung phase shifts on a two-crystal setup [1] by a dispersionless method without averaging over the pendellosung oscillations and, later [8–10], another nonaveraging method was proposed for the observation of the effects associated with the presence of crystal electric fields. This is the polarization method, which can be used for measurements at Bragg angles close to a right angle. The polarization experiments are particularly

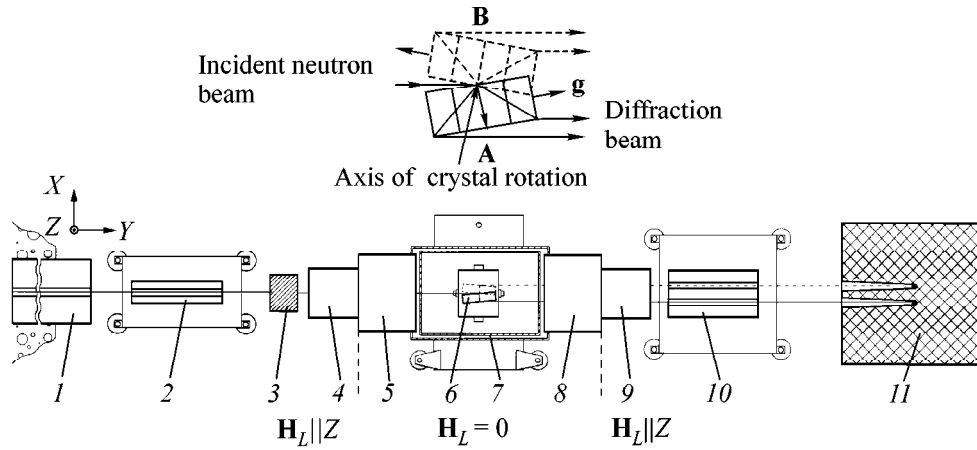


Fig. 1. Scheme of the experimental setup. (1) Intrachannel neutron guide; (2) multislit polarizing neutron guide; (3) 120-mm thick BeO filter; (4 and 9) spin-orienting coils; (5 and 8) three-coordinate rotating coils; (6) single crystal of α -quartz of size $14 \times 14 \times 3.47$ cm; (7) magnetic screen; (10) paired multislit analyzing neutron guide; and (11) neutron detector. **A** and **B** are crystal positions corresponding to the same Bragg angle; **g** is the reciprocal lattice vector for the (110) plane; and H_L is the driving magnetic field.

important, because they are less sensitive to the crystal perfection, allowing one to sizably extend the range of crystals suitable for experiments and to greatly simplify the setup.

The essence of the method is that the wave packets for the $\psi^{(1)}$ and $\psi^{(2)}$ states, in which a neutron “feels” the fields equal in magnitude but opposite in sign (and which are excited with the same amplitude), spatially overlap if the Bragg conditions for Laue diffraction are exactly fulfilled. In this case, the neutron spin in the $\psi^{(1)}$ and equally probable $\psi^{(2)}$ states rotates in opposite directions, so that the average angle of neutron spin rotation (in a transparent crystal) caused by the Schwinger interaction (or EDM) is zero.² Nevertheless, the polarization will decrease; i.e., the beam will depolarize. The depolarization measurements may be used for estimating, e.g., the magnitude of the electric field acting on the neutron.

The rotation angles of a spin initially oriented perpendicular to the “Schwinger” magnetic field in the $\psi^{(1)}$ and $\psi^{(2)}$ states are related to shift (2) as $\Delta\phi_0^S = \pm\Delta\phi^S/2$. As a result, the polarization P of a beam passed through the crystal depends on the $\Delta\phi_0^S$ angle as

$$P = P_0 \cos \Delta\phi_0^S = P_0 \cos(\mu_n e E_g L / m_p c^2), \quad (3)$$

where P_0 is the polarization of the incident beam. In particular, for a spin rotation of $\pi/2$ ($\Delta\phi_0^S = \pm\pi/2$), the neutron beam becomes completely unpolarized upon

² The neutron spin rotation caused by the EDM or the spin-orbit interaction was considered in [11–13] for the diffraction in a non-centrosymmetric crystal. The spin-orbit-induced rotation of a neutron spin near the Bragg direction in the Bragg diffraction scheme was observed in [14]. However, the possibility of enhancing the effects was lacking in these works.

passing through the crystal. The calculations for the (110) plane of α -quartz show that the spin rotates at an angle of $\pi/2$ for a crystal of thickness $L_0 = 3.6$ cm. If the polarization of the incident neutron beam changes by $\pi/2$, i.e., if it is directed perpendicular to the scattering plane, the polarization of the diffracted beam does not change, because the neutron magnetic moment is directed either along or opposite to the Schwinger magnetic field, so that the spin does not rotate.

2. The scheme of the experimental setup for the observation of the above-mentioned effects is shown in Fig. 1. Measurements were made for the (110) plane of an α -quartz crystal of sizes $14.0 \times 14.0 \times 3.47$ cm. After passing through polarizer 2 and filter 3, the polarization vector of the neutron beam was adiabatically aligned with field H_g^S in a coil 4, whereupon it was rotated through angle α in a three-coordinate coil 5. If the crystal did not influence the spin orientation, the polarization vector, after passing through the crystal, would be restored in coil 8 to its initial direction along the H_g^S axis. The rotation through angle α can be accomplished about any axis perpendicular to the H_g^S vector. For clearness, Fig. 2 illustrates the behavior of the polariza-

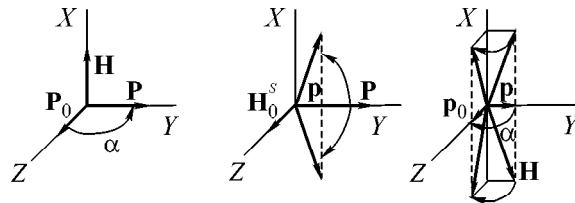


Fig. 2. Schematic representation of the behavior of a neutron polarization vector upon passing through the experimental setup for $\alpha = 90^\circ$.

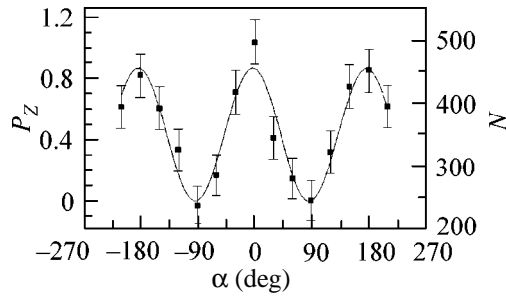


Fig. 3. An example of the intensity (after the analyzer) of neutrons diffracted by the (110) plane of α -quartz vs. the α° angle between the Schwinger magnetic field \mathbf{H}_g^S and the polarization vector of neutrons incident at a Bragg angle of $\theta_B = 84^\circ$.

tion vector for $\alpha = 90^\circ$. The coordinate system (X, Y, Z) in Figs. 1 and 2 is the same. To observe the effect of depolarization of a diffracted neutron beam, the dependence of counting rate on the angle α was measured in detectors *II* located after analyzer *IO*, which transmits only the neutrons polarized along \mathbf{H}_g^S . The described measurement procedure is analogous to the spin echo method.

It is known from previous measurements of the time-of-flight spectrum of a diffracted beam (see [7]) that not only the neutrons diffracted by the system of planes of interest contribute to the direct diffracted beam but also the neutrons diffracted by some other systems with zero average interplanar electric field (i.e., for which the depolarization effect is absent). To reduce the corresponding contribution from the background reflections to the neutron beam, a polycrystalline 120-mm-thick BeO filter (3) transmitting only neutrons with wavelengths $\lambda > 4.7 \text{ \AA}$ was placed before the crystal. With this filter, the contribution of the background reflections to the direct neutron beam was estimated at $\approx (20 \pm 10)\%$ of the intensity of the beam diffracted by a working plane. The uncertainty of this contribution gives rise to a systematic error of the measured quantities.

If the neutron spin in the $\psi^{(1)}$ and $\psi^{(2)}$ states in a crystal rotates by angles $\pm \Delta\phi_0^S$, respectively, the counting rate N in the detector placed after the polarization analyzer depends on the angle α as

$$N = N_0(1 + P_Z), \quad (4)$$

where

$$P_Z = P_0(\cos\Delta\phi_0^S \sin^2 \alpha + \cos^2 \alpha) \quad (5)$$

is the projection of the neutron polarization onto the \mathbf{H}_g^S direction after passing through the crystal. One can see that if the effect is absent, i.e., $\Delta\phi_0^S = 0$, then $P_Z \equiv P_0$ and N is independent of α .

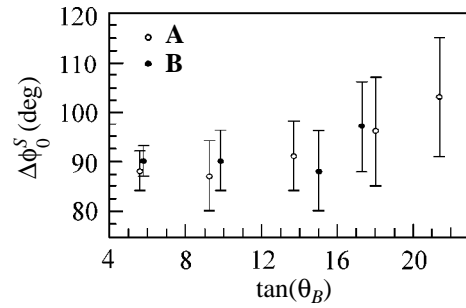


Fig. 4. The angle $\Delta\phi_0^S$ of neutron spin rotation due to the Schwinger interaction vs. the tangent of the Bragg angle. **A** and **B** correspond to two crystal positions (see Fig. 1).

It was found from the preliminary measurements that the initial polarization of the direct beam was $P_0 = (87 \pm 3)\%$.

Therefore, the $\Delta\phi_0^S$ value can be determined from the N dependence on α . An example of such a dependence is presented in Fig. 3. The polarization P_Z is indicated on the left ordinate axis. The curve in Fig. 3 is the experimental fit to Eqs. (4) and (5).

It follows from Eq. (2) that the effect of the Schwinger interaction does not depend on the Bragg angle, which was indeed observed in the experiment (Fig. 4).

Using the experimental value of rotation angle $\Delta\phi_0^S$, one can determine the crystal electric field acting on a diffracting neutron:

$$E_{(110)} = (2.24 \pm 0.05(0.20)) \times 10^8 \text{ V/cm}, \quad (6)$$

where a systematic error introduced by the uncertainty of background reflections is indicated in the inner brackets.

3. The indicated value of the electric field is in agreement, within the experimental error, with the value measured from the pendellosung phase shift caused by the spin flip of a neutron incident at Bragg angle $\theta_B \approx 25^\circ$ [3], thereby confirming that the electric field does not change, at least up to $\theta_B \approx 87^\circ$, i.e., to $1/(\pi/2 - \theta_B) \approx 20$. For this diffraction angle, the sensitivity of the method to the neutron EDM increases (compared to $\theta_B \approx 45^\circ$) by approximately a factor of 20. Using the experimentally measured neutron residence time τ in the crystal for Bragg angle $\theta_B = 87^\circ$ [7], one obtains the value of $\sim 0.2 \times 10^6 \text{ V s/cm}$ for the $E\tau$ quantity determining the sensitivity of the method.³ This value is comparable with the corresponding value for the UCN method ($\sim 10^6 \text{ V s/cm}$ [4]) and is appreciably higher than the

³ Note that the absolute error of measuring EDM is $\sigma(D) \approx 1/E\tau\sqrt{N}$, where E is the electric field acting on a neutron and N is the total number of accumulated events.

value of $\sim 0.2 \times 10^3$ V s/cm obtained in the well-known Shull–Nathans diffraction experiment [15].⁴

In summary, the effect of depolarization of a neutron beam upon the Laue diffraction in a noncentrosymmetric α -quartz crystal was experimentally observed. The magnitude of the effect (and of the crystal field acting on a neutron) is independent of the Bragg angle up to $\theta_B = 87^\circ$ and coincides, within the experimental error, with the theoretical predictions. This confirms our proposal that the neutron EDM effect can be enhanced by more than an order of magnitude for diffraction angles close to 90° .

We are grateful to O.I. Sumbaev, V.L. Alekseev, and V.L. Rumyantsev for interest in the work and numerous helpful discussions; to N.G. Kolyvanova and A.A. Zavediya for assistance in providing software and electronic support to the experiment; to the personnel of the WWR-M reactor for the experiment; and to P.L. Sokolova for assistance in manuscript preparation.

This work was supported by the Russian Foundation for Basic Research, project nos. 96-02-18927 and 00-02-16854.

REFERENCES

1. V. V. Fedorov, V. V. Voronin, and E. G. Lapin, Preprint LNPI-1644 (Leningrad, 1990), p. 36; *J. Phys. G* **18**, 1133 (1992).
2. V. L. Alexeev, V. V. Fedorov, E. G. Lapin, *et al.*, Preprint LNPI-1502 (Leningrad, 1989), p. 14; *Nucl. Instrum. Methods Phys. Res. A* **284**, 181 (1989).
3. V. L. Alekseev, V. V. Voronin, E. G. Lapin, *et al.*, *Zh. Éksp. Teor. Fiz.* **96**, 1921 (1989) [*Sov. Phys. JETP* **69**, 1083 (1989)].
4. I. S. Altarev, Yu. V. Borisov, N. V. Borovikova, *et al.*, *Yad. Fiz.* **59**, 1204 (1996) [*Phys. At. Nucl.* **59**, 1152 (1996)].
5. K. F. Smith, N. Crampin, J. M. Pendlebury, *et al.*, *Phys. Lett. B* **234**, 191 (1990).
6. P. G. Harris, C. A. Baker, K. Green, *et al.*, *Phys. Rev. Lett.* **82**, 904 (1999).
7. V. V. Voronin, E. G. Lapin, S. Yu. Semenikhin, and V. V. Fedorov, *Pis'ma Zh. Éksp. Teor. Fiz.* **71**, 110 (2000) [*JETP Lett.* **71**, 76 (2000)].
8. V. V. Voronin, E. G. Lapin, and V. V. Fedorov, Preprint PIYaF-NP-2-1994 (Gatchina, 1994).
9. V. V. Fedorov, V. V. Voronin, E. G. Lapin, and O. I. Sumbaev, *Pis'ma Zh. Tekh. Fiz.* **21** (21), 50 (1995) [*Tech. Phys. Lett.* **21**, 884 (1995)].
10. V. V. Fedorov, V. V. Voronin, E. G. Lapin, and O. I. Sumbaev, *Physica B (Amsterdam)* **234–236**, 8 (1997).
11. M. Forte, *J. Phys. G* **9**, 745 (1983).
12. V. G. Baryshevskii and S. V. Cherepitsa, *Phys. Status Solidi B* **128**, 379 (1985).
13. V. G. Baryshevskii and S. V. Cherepitsa, *Izv. Vyssh. Uchebn. Zaved., Fiz.* **8**, 110 (1985).
14. M. Forte and C. M. E. Zeyen, *Nucl. Instrum. Methods Phys. Res. A* **284**, 147 (1989).
15. C. G. Shull and R. Nathans, *Phys. Rev. Lett.* **19**, 384 (1967).

⁴ Note that the measurements carried out for two crystal positions **A** and **B** give the estimate $D \leq 10^{-22}$ e cm for the neutron EDM, which is even better than the result obtained in experiment [15].

Translated by V. Sakun

Charge-Carrier Separation in Rolled Heterostructures

V. M. Osadchiĭ and V. Ya. Prinz

*Institute of Semiconductor Physics, Siberian Division, Russian Academy of Sciences,
pr. Akademika Lavrent'eva 13, Novosibirsk, 630090 Russia*

Received May 22, 2000; in final form, August 10, 2000

The strains in rolled InAs/GaAs heterostructures of nanometer sizes are calculated. It is shown that the strain distributions in nanotubes (structures with coherently bounded rolls) and nanoscrolls are essentially different, resulting in different energy spectra of the charge carriers. Photogenerated electrons and holes in nanotubes can be spatially separated across the wall width. © 2000 MAIK "Nauka/Interperiodica".

PACS numbers: 73.20.Dx

The influence of purely geometrical factors on the properties of a two-dimensional electron gas confined to a cylindrical surface was studied in a series of works [1–4]. A method of preparing micro- and nano- tubes and scrolls was recently demonstrated in [5, 6]. They were prepared from thin strained double-layer InGaAs/GaAs films grown on an InP or GaAs substrate. In the constituent layers, the GaAs layer is stretched, while the InGaAs layer is compressed because of a lattice mismatch. After such a strained double-layer film is detached from the substrate, it rolls up into a scroll as a result of the elastic relaxation of mechanical strains. The layers are grown together in a scroll to form a tube with single-crystal walls. The walls of such a tube are subjected to tangible elastic strains. It is known [7] that the strains affect the band structure of semiconductors and greatly influence the energy spectrum of charge carriers in quantum-dimensional structures. In this work, we use a simple model to calculate the strains in the walls of GaAs/InAs nanotubes and the energy levels and wave functions of charge carriers in this structure.

The structure of interest is displayed in Fig. 1. To simplify the calculations, the following approximations were adopted. The tube was assumed to be axially symmetric; the original film was grown on a (100) substrate; and the tube axis was aligned with the crystallographic [010] direction. Under these conditions, only the diagonal strain tensor components are nonzero, i.e., the axial component ε_z , the azimuthal component ε_θ , and the radial component ε_r . The following parameters were taken for the material: lattice constant $a = 0.5653$ nm, Young's modulus $E = 85.5$ GPa, and Poisson's ratio $\nu = 0.31$ for GaAs and $a = 0.6058$ nm, $E = 51.4$ GPa, and $\nu = 0.35$ for InAs. The calculations were carried out for a four-turn tube formed from a double-layer film consisting of InAs and GaAs layers each three monolayers thick. The inner radius R of the tube was equal to the radius of curvature of the double layer [8], $R = 16.5$ nm.

To calculate the strains in the layers forming the tube walls, let us determine the lattice constants for the layers. The lattice constant a_z along the tube axis does not change upon rolling up and is equal to the lattice constant in the plane of a free superlattice [7]:

$$a_z = \frac{a_1 G_1 h_1 + a_2 G_2 h_2}{G_1 h_1 + G_2 h_2},$$

where h_1 and h_2 are the layer thicknesses and $G_{1(2)} = E_{1(2)}/(1 - \nu_{1(2)})$. The difference between the lattice constants in the unstrained and strained materials determines the strain $\varepsilon_z = (a - a_z)/a_z$ (Fig. 2a, curve 1).

In a bent monolayer film, the neutral surface (boundary between the stretched and the compressed layers) is situated almost in the middle of the film [9]. In a two-layer film, the bending strain is appended by the lattice-mismatch strain. When calculating the azimuthal strain in a multiturn tube, we assumed that the neutral surface is situated in the middle of the tube wall. At this surface, the azimuthal lattice constant a_θ is equal to the lattice constant a_z along the tube axis. This follows from the fact that, according to our calculations, the strain energy of the tube is close to minimum at $a_\theta = a_z$. Evidently, a_θ in a single-crystal tube changes linearly with radius, so that the dependence of the azimuthal strain on the radius can easily be determined (Fig. 2a, curve 2). The radial strain is found from the Poisson relation $\varepsilon_r = -\nu(1 - \nu)^{-1}(\varepsilon_\theta + \varepsilon_z)$, which is valid even for monolayer films [10].

Knowing the strain distribution, one can determine the band-edge shifts [7]: $\Delta E_c = a_c \text{Tr}(\varepsilon)$ for the conduction band and

$$\Delta E_{hh(lh)} = a_v \text{Tr}(\varepsilon) \mp b \left(\varepsilon_r - \frac{\varepsilon_\theta + \varepsilon_z}{2} \right)$$

for the valence band (the upper sign refers to the heavy-hole band and the lower sign to the light-hole band), where $\text{Tr}(\varepsilon) = \varepsilon_r + \varepsilon_\theta + \varepsilon_z$ and a_c, a_v , and b are the defor-

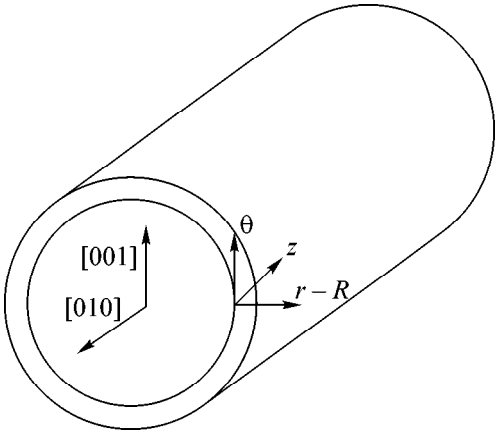


Fig. 1. Schematic representation of a nanotube. The crystallographic directions and the axes for calculating the strain tensor components are shown.

mation potentials. In GaAs, $a_c = -7.17$ eV, $a_v = 1.16$ eV, and $b = -1.6$ eV; in InAs, $a_c = -5.08$ eV, $a_v = 1$ eV, and $b = -1.6$ eV. Since the off-diagonal strain tensor components are zero, a piezoelectric field is absent [11]. The calculated band-edge profiles across the tube width are shown in Fig. 3a for the conduction and heavy-hole valence bands in an undoped structure (solid lines). It is taken into account that, in GaAs, the band gap $E_g = 1.424$ eV and the electron affinity $\chi = 4.07$ eV and, in InAs, $E_g = 0.355$ eV and $\chi = 4.9$ eV. One can see that the band gap changes jumpwise at the layer boundaries; the band gap in each layer decreases, and the edges of both bands lower as the outer wall of the tube is approached. This picture is obtained under the assumption that the near-surface band is not curved and the Coulomb interaction between the charge carriers is small, which seems to be justified. Indeed, the near-surface band is only slightly curved in the undoped struc-

tures and besides, it may disappear at low temperatures upon the photogeneration of charge carriers [12], i.e., in the situation where electrons and holes can simultaneously be present. As for the Coulomb interaction between the photogenerated charge carriers, estimations show that, even for very high electron and hole charge densities (10^{12} cm $^{-2}$) at the opposite surfaces of the tube, its contribution to the potential is only ~ 0.1 eV for the wall thickness considered, which is considerably smaller than the strain-induced contribution.

The energy spectrum and the wave functions of charge carriers in the structure of interest can be calculated based on the lineup of band edges. In the effective mass approximation for the radial part of the ground-state wave function Ψ (with zero azimuthal quantum number), the Schrödinger equation has the form

$$-\frac{\hbar^2}{2m^*} \frac{1}{r} \frac{d}{dr} \left(r \frac{d\Psi}{dr} \right) + U\Psi = E_0\Psi.$$

Here, m^* is the electron effective mass and U is the potential energy (the corresponding band edge). It was assumed that the electron mass $m^* = 0.067m_0$ in GaAs and $m^* = 0.023m_0$ in InAs, where m_0 is the free electron mass, and the hole mass is $0.4m_0$ for both materials. A one-band effective-mass approximation gives proper levels for the electrons and the hole ground state [13]. For the excited hole states, mixing of the heavy- and light-hole bands should be taken into account, because it reduces the effective hole mass, e.g., in quantum wires by 30% on decreasing the wire radius from 10 to 2.5 nm [14]. Such mass changes do not appreciably affect our results. The boundary conditions for the wave function are that it is zero at the tube walls and the Ψ and $(1/m^*)(d\Psi/dr)$ values are continuous at the interfaces.

The potential energy in the Schrödinger equation for our structure is a piecewise linear function of the radius. In such a situation, the solution to the equation

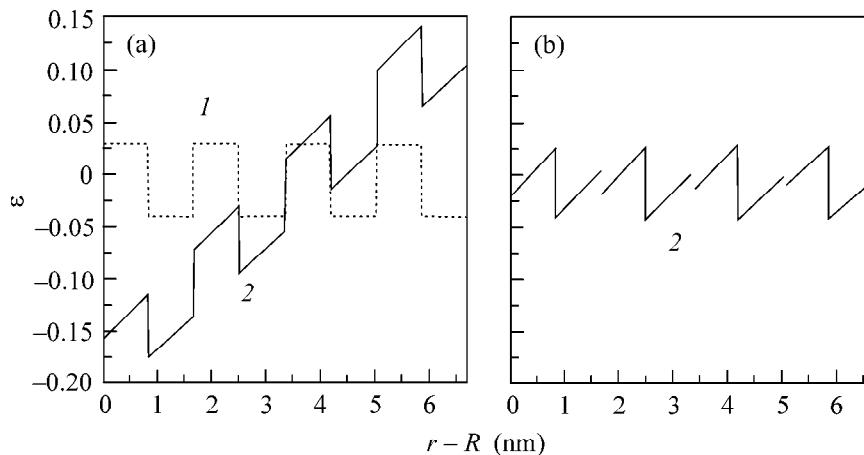


Fig. 2. Distributions of (1) axial and (2) azimuthal strain components across the width of (a) nanotube and (b) nanoscroll.

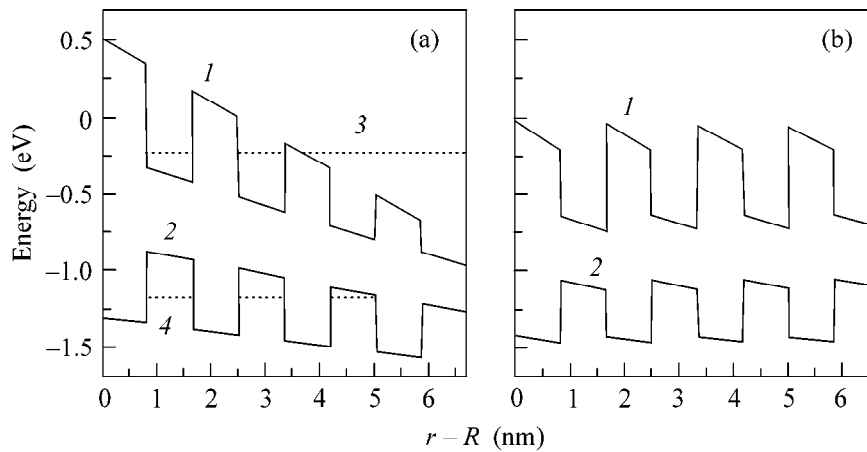


Fig. 3. (1) Conduction and (2) valence band edges in (a) nanotube and (b) nanoscroll. (3) Electronic and (4) hole energy levels in the nanotube.

cannot be expressed in terms of known functions and can only be obtained by numerical methods. The calculated electronic and hole energy levels are shown in Fig. 3a by dotted lines. The electronic level is shown for the Γ minimum of the conduction band. For the side minima (L and X), the effective mass is greater than in the Γ minimum and the respective size-quantization levels are raised more slowly with decreasing well sizes; however, calculations show that the electronic state in the Γ valley remains the lowest for a tube with an InAs thickness of more than one monolayer, as in the free GaAs/InAs superlattices [15].

The calculated electron and hole wave functions are shown in Fig. 4. One can see that the charge carriers of opposite signs are spatially separated, as can be

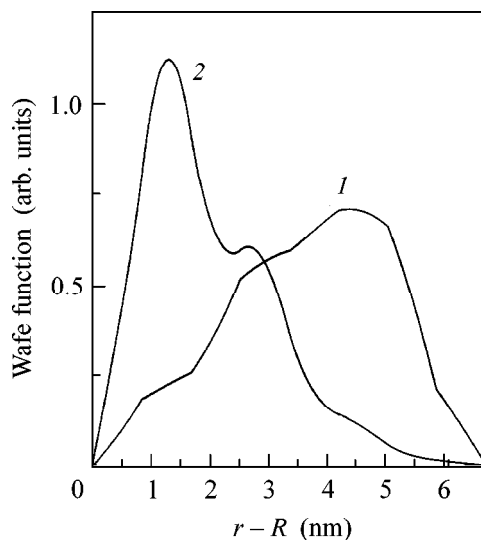


Fig. 4. Wave functions of (1) electrons and (2) holes in the nanotube.

expected from the band-edge lineup (Fig. 3a). The calculations show that charge separation occurs if the number of turns exceeds two and that the degree of separation increases with increasing number of turns.

Let us consider, for comparison, the strain distribution and the lineup of band edges in a nanoscroll, i.e., in a rolled heterostructure in which the turns are not grown together. In this case, the neutral surface is positioned in the middle of each turn; the respective azimuthal lattice constant a_θ is equal to the axial constant a_z , and a_θ changes linearly across the film width. The distribution of azimuthal strain is shown in Fig. 2b. A profound distinction from the strain distribution in a tube is seen. In the scroll, the strain in each turn is mainly determined by its radius, whereas in the tube, all interfaces are strained, so that the strains in the turns are not independent of each other. The axial strain is the same in the tube and the scroll.

The band edge lineup in a scroll is depicted in Fig. 3b. It is seen that it changes slightly from turn to turn. A minimum of the conduction band edge in each turn occurs at the right boundary of the InAs layer. One can show that the part of the conduction band shift depending on the turn radius R_s at this point is equal to

$$a_c \frac{1 - 2\nu}{1 - \nu} \frac{a_z}{a_{\text{InAs}}} \frac{h_{\text{InAs}}}{R_s},$$

i.e., the minimum of conduction band edge (potential well for electrons) slightly increases on passing to the outer turns. The maximum of the valence band edge does not change on going from turn to turn. The calculations show that the charge carriers of opposite signs are not separated in the scroll.

Let us briefly dwell on the maximum strain that is attained in the tube walls (Fig. 2a). It is seen from Fig. 2a that the maximum strain in a four-turn tube is markedly higher than the strain attained in the pseudomorphic layers prepared by molecular beam epitaxy

(MBE). Four-monolayer-thick GaAs and InAs films can be grown with a strain of $\approx 4\%$ on an InP substrate. In Fig. 2a, the strains in two middle bilayers of the tube wall are within this range. As to the outer layers, the strains exceed 10% of the thermodynamical limit for lattice mismatch in pseudomorphic film growth [16]. Although such strains usually generate dislocations, a metastable pseudomorphic state may also arise at low growth temperatures, which are typical for MBE. For instance, pseudomorphic CdTe monolayers were grown on a GaAs substrate with a lattice mismatch of 14% [17] and similar $\text{Si}_{0.48}\text{C}_{0.52}$ monolayers were prepared in silicon with strains greater than 10% [18]. In our case, the original films were pseudomorphic and the process of rolling up into a tube occurred at room temperature, so that dislocations did not form, as was confirmed by electron microscopy of such tubes [6].

This work was supported by the Russian Foundation for Basic Research (project nos. 00-02-16764 and 99-02-16689) and the Russian program "Physics of Solid-State Structures" (project no. 98-2030).

REFERENCES

1. L. I. Magarill, D. A. Romanov, and A. V. Chaplik, Pis'ma Zh. Éksp. Teor. Fiz. **64**, 421 (1996) [JETP Lett. **64**, 460 (1996)].
2. L. I. Magarill, D. A. Romanov, and A. V. Chaplik, Zh. Éksp. Teor. Fiz. **113**, 1411 (1998) [JETP **86**, 771 (1998)].
3. L. I. Magarill and A. V. Chaplik, Zh. Éksp. Teor. Fiz. **115**, 1478 (1999) [JETP **88**, 815 (1999)].
4. A. I. Veretennikov and A. V. Chaplik, Zh. Éksp. Teor. Fiz. **117**, 449 (2000) [JETP **90**, 397 (2000)].
5. V. Ya. Prinz, V. A. Seleznev, and A. K. Gutakovsky, in *Proceedings of the ICPS-24, Jerusalem, 1998* (World Scientific, Singapore, 1999).
6. V. Ya. Prinz, V. A. Seleznev, A. K. Gutakovsky, *et al.*, Physica E (Amsterdam) **6**, 828 (2000).
7. C. G. van de Walle, Phys. Rev. B **39**, 1871 (1989).
8. Y. C. Tsui and T. W. Clyne, Thin Solid Films **306**, 23 (1997).
9. S. Timoshenko and S. Woinowsky-Krieger, *Theory of Plates and Shells* (McGraw-Hill, New York, 1959; Fizmatgiz, Moscow, 1963).
10. J. E. Bernard and A. Zunger, Appl. Phys. Lett. **65**, 165 (1994).
11. J. F. Nye, *Physical Properties of Crystals* (Oxford Univ. Press, New York, 1985).
12. R. B. Darling, Phys. Rev. B **43**, 4071 (1991).
13. H. Jiang and J. Singh, Phys. Rev. B **56**, 4696 (1997).
14. P. C. Sercel and K. J. Vahala, Phys. Rev. B **42**, 3690 (1990).
15. A. Taguchi and T. Ohno, Phys. Rev. B **38**, 2038 (1988).
16. I. Daruka and A. L. Barabasi, Phys. Rev. Lett. **79**, 3708 (1997).
17. H. Sitter and W. Faschinger, Thin Solid Films **225**, 250 (1993).
18. W. Faschinger, S. Zerlauth, J. Stangl, and G. Bauer, Appl. Phys. Lett. **67**, 2630 (1995).

Translated by V. Sakun

High-Pressure Phases in Nanocrystalline Co(C) Films Obtained by Pulsed Plasma Vaporization

R. S. Iskhakov*, S. V. Stolyar**, L. A. Chekanova*,
E. M. Artem'ev***, and V. S. Zhigalov*

* *Kirenskiĭ Institute of Physics, Siberian Division, Russian Academy of Sciences, Akademgorodok, Krasnoyarsk, 660036 Russia*

** *Krasnoyarsk State University, Krasnoyarsk, 660041 Russia*

*** *Krasnoyarsk State Technical University, Krasnoyarsk, 660074 Russia*

Received August 14, 2000

The phase composition of nanocrystalline Co(C) films obtained by a new pulsed plasma vaporization technique was found by studying their atomic structure and magnetic properties. The films deposited at the substrate temperature $T = 50^\circ\text{C}$ were of heterophase structure and consisted of a supersaturated solid Co(C) solution and the metastable Co_3C carbide. The films obtained at $T = 150^\circ\text{C}$ represented a mechanical mixture of the metastable Co_3C and Co_2C carbides. The metastable Co_3C and Co_2C carbides obtained in a nanocrystalline state were high-pressure phases (~ 100 kbar). The thermal stability ranges of these metastable phases were determined. © 2000 MAIK "Nauka/Interperiodica".

PACS numbers: 75.70.-i; 76.50.+g; 81.30.Bx

It is known that nanocrystalline alloys possess a high defect density, an excess volume per atom, and hence an excess Gibbs free energy. This leads to the formation of new metastable phases in the nanostructured state. A new pulsed plasma vaporization technique was developed at the Institute of Physics, Siberian Division, Russian Academy of Sciences (Krasnoyarsk). Nanocrystalline Fe, Co, and Ni films containing from 20 to 30 at. % C can be obtained by this technique [1]. Nanocrystalline Fe(C) alloy films were studied in [2]. It was found that a chain of structural transformations, fcc Fe(C) \rightarrow hcp Fe(C) \rightarrow bcc Fe + C, was carried out in these films as a result of thermal relaxation. It is known that a closely packed modification, hcp Fe, is a high-pressure phase and is stabilized at $P \sim 50$ kbar. The work presented here is devoted to studying nanocrystalline Co(C) films obtained by the pulsed plasma vaporization technique. The aim of this work is to investigate the phase composition of Co(C) films and to determine the thermal stability ranges of the metastable structural states found in this work.

Co(C) alloy films 1000 Å thick were obtained by the pulsed plasma vaporization technique in a vacuum with the residual gas pressure $P_0 = 10^{-6}$ mm Hg. Glass and glass ceramic were used as substrates. The films were synthesized at the following substrate temperatures T_i : $T_1 = 50^\circ\text{C}$, $T_2 = 100^\circ\text{C}$, $T_3 = 150^\circ\text{C}$, and $T_4 = 250^\circ\text{C}$. Stepped annealing of the Co(C) films was performed for an hour in a vacuum chamber with the residual gas pressure $P_0 = 10^{-6}$ mm Hg. The atomic structure of the initial and annealed nanocrystalline Co(C) films was studied by transmission electron microscopy and synchrotron radiation X-ray diffraction (Institute of

Nuclear Physics, Siberian Division, Russian Academy of Sciences, Siberian International Center of Synchrotron Radiation). The synchrotron radiation wavelength was $\lambda = 1.748$ Å.

The dynamic magnetic properties of nanocrystalline Co(C) films were studied on a standard x-band spectrometer. The resonant fields of ferromagnetic resonance were measured at room temperature throughout the entire range of angles between the external field and the film plane with the aim of determining the effective magnetization M_{eff} by the equation

$$H_{\perp}^r - 4\pi M_{\text{eff}} = \sqrt{H_{\parallel}^r(H_{\parallel}^r + 4\pi M_{\text{eff}})},$$

where H_{\perp}^r and H_{\parallel}^r are the fields of ferromagnetic resonance for the corresponding experimental geometry.

Co(C) films obtained at $T_i = 50^\circ\text{C}$. Figure 1 displays X-ray spectra ($\lambda = 1.748$ Å) of Co(C) films obtained at $T_i = 50^\circ\text{C}$. Curve a in Fig. 1 (initial sample) is characterized by two peaks: $d = 2.07$ Å (the region of coherent scattering estimated from the width of this peak equals 40 Å) and $d = 2.20$ Å. The reflection at $d = 2.07$ Å is considerably shifted towards small angles with reference to the reflection from the (111) plane of the fcc Co lattice, which points to an increased value of the lattice constant a . The C content of the fcc Co solid solution can be estimated from this shift. This estimation gives $\sim \text{Co}_{90}\text{C}_{10}$. (Note that the equilibrium solubility of C in Co at $T = 1310^\circ\text{C}$ is only $X_0 \sim 3$ at. %). The peak at $d = 2.20$ Å is due to the reflection from the (120) plane of the metastable Co_3C carbide with an orthorhombic lattice. Annealing at $T = 200^\circ\text{C}$ leads to the for-

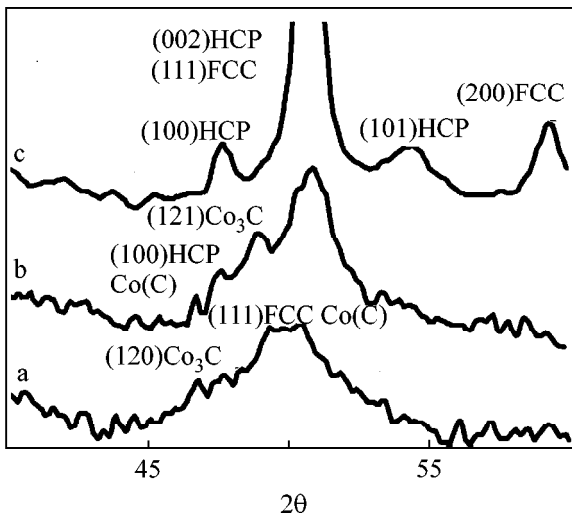


Fig. 1. X-ray diffraction patterns of (a) the initial Co(C) film obtained at $T = 50^\circ\text{C}$, (b) an annealed film at $T = 200^\circ\text{C}$, and (c) a film annealed at $T = 400^\circ\text{C}$.

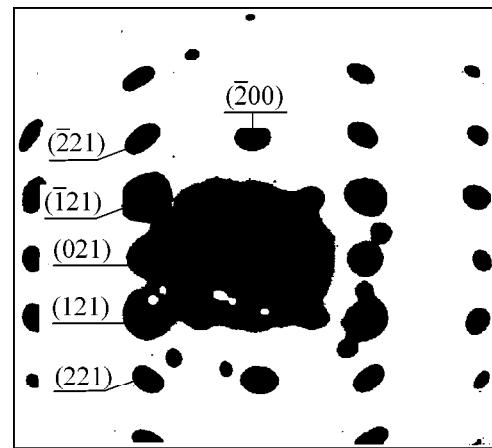


Fig. 2. Microdiffraction pattern obtained from the metastable Co₃C carbide. The axis of the reflection zone is $[01\bar{2}]$.

mation of the carbide (additional reflections appear) and to the appearance of reflections from a solid solution of hcp Co(C). Annealing at $T = 400^\circ\text{C}$ leads to the dissolution of Co₃C (reflections from the carbide disappear in curve c, Fig. 1) and to the formation of a heterophase system (hcp + fcc) Co with lattice constants typical of the phases of pure cobalt.

Electron-diffraction patterns obtained for the initial samples were characterized by three diffuse rings, which indicated that the atomic structure of the Co(C) films was disordered [1]. After annealing for one hour ($T = 140^\circ\text{C}$), discrete-point diffraction patterns were observed. Figure 2 shows this microdiffraction pattern and its interpretation, indicating that a Co₃C phase with an orthorhombic lattice was observed. The lattice parameters of the metastable Co₃C carbide determined from the diffraction pattern ($a = 4.5 \text{ \AA}$, $b = 5.14 \text{ \AA}$, $c = 6.72 \text{ \AA}$) are in agreement with the results of structural investigations performed for metastable carbides by other authors [3].

One ferromagnetic resonance line was observed for the film under study when it was aligned parallel to the magnetic field. We measured the angular dependence of this line throughout the entire range of angles. Using Eq. (1), we determined the effective magnetization of a supersaturated solid Co(C) solution (metastable Co₃C carbide was found to be paramagnetic at room temperature). For the films under study, Table 1 presents M_{eff} of the Co(C) solid solution, the annealing temperatures, and the phase states found by structural methods. An increase in magnetization after annealing at $T = 250^\circ\text{C}$ is associated with the fact that the decomposition of the metastable Co₃C carbide results not only in an increase in the volume fraction of the Co(C) solid solution, but also in a decrease in the concentration of C in this solid solution down to X_0 .

Nanocrystalline Co(C) films obtained at $T_i = 100\text{--}150^\circ\text{C}$. As well as the samples obtained at $T_i = 50^\circ\text{C}$, these films were found to be two-phase systems. However, the metastable Co₃C carbide was the major matrix phase in this case. Another metastable carbide, Co₂C, was present as inclusions dispersed in this matrix. Figure 3 shows a photograph of a Co₂C carbide microdiffraction pattern and its interpretation. The orthorhombic lattice constants of the stoichiometric Co₂C carbide calculated in this work ($a = 2.9 \text{ \AA}$, $b = 4.47 \text{ \AA}$, $c = 4.43 \text{ \AA}$) are in agreement with the results obtained by other authors [3]. The Co₂C carbide has higher thermal stability than the Co₃C phase. It was observed even in Co(C) films annealed at $T = 500^\circ\text{C}$. It was possible to determine the decomposition temperature of metastable carbides by ferromagnetic resonance measurements carried out for the given sets of samples after their thermal annealing. Note that these films in the initial state exhibit no resonance absorption of microwave radiation energy, because the Co₂C carbide, as well as the Co₃C carbide, is paramagnetic at room temperature. After annealing these films for one hour at $T = 250^\circ\text{C}$ (the decomposition temperature of Co₃C), a ferromagnetic resonance signal appears. From measurements of the angular dependence of the resonant fields, it was found that a supersaturated Co(C) solid solution was the ferromagnetic matrix in these

Table 1. Co(C) at $T = 50^\circ\text{C}$

$T_{\text{anneal}}, ^\circ\text{C}$	$M_{\text{eff}}, \text{Hz}$	Composition
Initial	990	–Co ₃ C + Co ₉₀ C ₁₀
150	1000	–Co ₃ C + Co ₉₀ C ₁₀
250	1280	–Co(C)

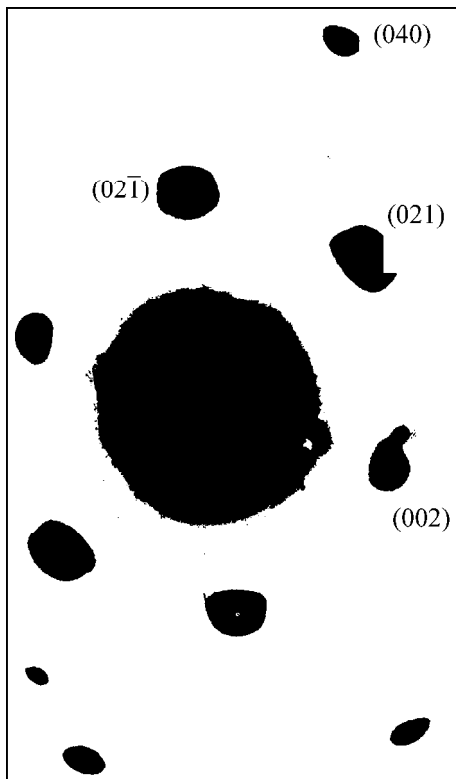


Fig. 3. Microdiffraction pattern obtained from the metastable Co_2C carbide. The axis of the reflection zone is $[100]$. The film was obtained at $T = 500^\circ\text{C}$, and annealing was carried out at a temperature of 300°C .

annealed films. Table 2 gives the values of effective magnetization M_{eff} calculated from the ferromagnetic resonance curves and the annealing temperatures for this series of films. From the data presented in Table 2, it is evident that the metastable Co_2C carbide is decomposed after annealing for one hour at $T = 520^\circ\text{C}$.

Co films obtained at $T_i = 250^\circ\text{C}$ are characterized by (hcp + fcc) Co reflections. The lattice constants calculated from these reflections are typical of the phases of pure cobalt. The measured magnetic characteristics exhibit the same property.

The structural states occurring in metastable Co(C) films were analyzed with the use of a metastable Co–C phase diagram shown in Fig. 4 in the coordinates (G, C) , where $G = H - TS$ (H is enthalpy and S is

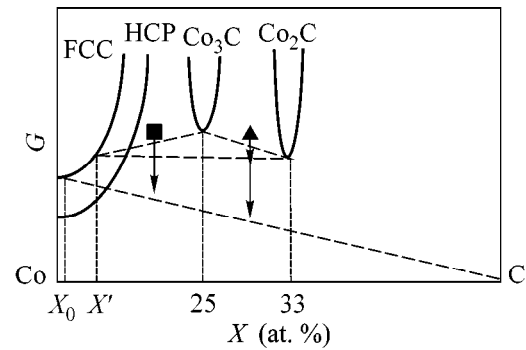


Fig. 4. Qualitative phase diagram of a Co–C system on the (G, X) coordinates.

entropy) is the Gibbs energy. Here, the transition enthalpy $\Delta H^{\text{fcc} \rightarrow \text{hcp}} = 0.22 \text{ kcal/mol}$ [4], and the positive formation enthalpies of the Co_3C and Co_2C carbides are $\sim 6 \text{ kcal/mol}$ and $\sim 4 \text{ kcal/mol}$, respectively [4]. Co(C) solid solutions that are in equilibrium with metastable carbides are supersaturated. The highest concentration of carbon in an equilibrium solid solution is $X_0 \sim 3 \text{ at. \%}$, which is considerably lower than the concentration of carbon in the metastable alloy $X' \sim 10 \text{ at. \%}$. In accordance with the results of studying the structure and magnetic properties, the initial state of the metastable Co–C films obtained by pulsed plasma vaporization at $T_i = 50^\circ\text{C}$ is shown by a square in Fig. 4. An increase in the substrate temperature during deposition to $T_i = 100\text{--}150^\circ\text{C}$ results in the formation of a mechanical mixture of the metastable Co_3C and Co_2C carbides in the initial state. This state is shown by a triangle in Fig. 4. The metastable Co_3C and Co_2C carbides are high-pressure phases and are stabilized in the Co–C alloy at the pressure $P \sim 100 \text{ kbar}$ [5]. The occurrence of the metastable phases in the nanocrystalline films under study was possible for the following reasons. Because of the small grain size ($\sim 40 \text{ \AA}$), the specific area S_n of the nanocrystalline Co(C) alloy is very large. The surface energy density σ_n in the metastable Co(C) films obtained by the pulsed plasma vaporization technique turned out to be so high that the contribution of the surface energy $S_n \times \sigma_n$ to the thermodynamic Gibbs potential ΔG was comparable to the formation enthalpy of the metastable carbides $\Delta G \sim \sigma_n S_n \geq \Delta H^{\text{carbide} \rightarrow \text{Co} + \text{C}}$. Heating a metastable Co(C) film results in an increase in the grain size of the nanocrystalline alloy; therefore, the relationship between ΔG and $\Delta H^{\text{carbide} \rightarrow \text{Co} + \text{C}}$ reverses its sign: $\Delta G < \Delta H^{\text{carbide} \rightarrow \text{Co} + \text{C}}$. Thus, the decomposition of metastable phases occurs.

It may be concluded that high-pressure phases occur in nanocrystalline Co(C) films obtained by the pulsed plasma vaporization technique at certain substrate temperatures. Films synthesized at $T_i = 50^\circ\text{C}$ are heterophase systems and consist of a supersaturated Co(C)

Table 2. Co(C) at $T = 100\text{--}150^\circ\text{C}$

$T_{\text{anneal}}, ^\circ\text{C}$	$M_{\text{eff}}, \text{Hz}$	Composition
Initial	–	$-\text{Co}_3\text{C} + \text{Co}_2\text{C}$
250	820	$-\text{Co}_2\text{C} + \text{Co(C)}$
350	850	$-\text{Co}_2\text{C} + \text{Co(C)}$
520	1250	Co(C)

solid solution and the stoichiometric Co_3C carbide. The following chain of structural transformations is observed upon thermal relaxation in the given systems (see the square in Fig. 4): $\text{Co(C)} + \text{Co}_3\text{C} \longrightarrow \text{Co} + \text{C}$. In the case of nanocrystalline Co(C) films obtained by the pulsed plasma vaporization technique at $T_i = 100\text{--}150^\circ\text{C}$, the initial phase composition and the sequence of structural transformations appear to be different (see Fig. 4, triangle): $\text{Co}_3\text{C} + \text{Co}_2\text{C} \longrightarrow \text{Co(C)} + \text{Co}_2\text{C} \longrightarrow \text{Co(C)} + \text{C}$. The decomposition of the metastable Co_3C and Co_2C carbides proceeds at temperatures of 250°C and 520°C , respectively.

REFERENCES

1. V. S. Zhigalov, G. I. Frolov, L. I. Kveglis, *et al.*, Fiz. Tverd. Tela (St. Petersburg) **40**, 2074 (1998) [Phys. Solid State **40**, 1878 (1998)].
2. R. S. Iskhakov, S. V. Komogortsev, S. V. Stolyar, *et al.*, Pis'ma Zh. Éksp. Teor. Fiz. **70**, 727 (1999) [JETP Lett. **70**, 736 (1999)].
3. S. Nagakura, J. Phys. Soc. Jpn. **16**, 1213 (1961).
4. *Thermal Constants of Materials* (Nauka, Moscow, 1972), Vol. 6.
5. A. A. Vertman, V. K. Grigorovich, N. A. Nedumov, *et al.*, Dokl. Akad. Nauk SSSR **162**, 1304 (1965).

Translated by A. Bagatur'yants

Long-Time Luminescence Kinetics of Localized Excitons and Conduction Band Edge Smearing in $\text{ZnSe}_{(1-c)}\text{Te}_c$ Solid Solutions

A. Klochikhin^{*,**}, S. G. Ogloblin^{*}, S. Permogorov^{**}, A. Reznitsky^{**}, C. Klingshirn^{***}, V. Lyssenko^{****}, and J. M. Hvam^{*****}

^{*} Konstantinov Institute of Nuclear Physics, Russian Academy of Sciences, Gatchina, Leningrad region, 188350 Russia

^{**} Ioffe Physicotechnical Institute, Russian Academy of Sciences, Politekhnikeskaya ul. 26, St. Petersburg, 193021 Russia

^{***} Universität Karlsruhe, Institut für Angewandte Physik, 76128 Karlsruhe, Germany

^{****} Institute of Microelectronic Technology and Ultra-High-Purity Materials, Russian Academy of Sciences, Chernogolovka, Moscow region, 142432 Russia

^{*****} Mikroelektronik Centret, Technical University of Denmark, DK-2800, Lyngby, Denmark

Received August 16, 2000

It is shown that the integrated luminescence intensity of localized excitons in solid solutions $\text{ZnSe}_{(1-c)}\text{Te}_c$ has a component slowly decaying with time. After the excitation above the mobility threshold, the long-time intensity decreases exponentially, with a fractional exponent changing from a value corresponding to the critical index of anomalous diffusion to the index of normal diffusion as the temperature increases from 5 to 80 K. This change allows estimation of the energy scale for the fluctuation tail of the conduction band. © 2000 MAIK "Nauka/Interperiodica".

PACS numbers: 71.23.An; 71.55.Jv

Pulsed optical studies of solid solutions $\text{ZnSe}_{(1-c)}\text{Te}_c$ and $\text{CdS}_{(1-c)}\text{Se}_c$ showed that the luminescence of excitons localized in fluctuation potential wells has a slow component nonexponentially decaying with time [1, 2]. In this work, we demonstrate that the time behavior of luminescence intensity depends on the experimental parameters such as the energy of the exciting photons and the sample temperature.

Compared to perfect crystals, the excitonic spectrum near the band bottom of solid solutions $\text{ZnSe}_{(1-c)}\text{Te}_c$ and $\text{CdS}_{(1-c)}\text{Se}_c$ is strongly modified [1–4]. The composition fluctuations generate random potential with wells capable of localizing a hole or an exciton. A particularly simple picture, allowing one to rationalize the luminescence spectrum of a solid solution, is observed for a $\text{ZnSe}_{(1-c)}\text{Te}_c$ crystal with a low concentration of the narrow-band component [2, 3]. At $c \leq 0.2$, the fluctuations in a system of randomly distributed anions of two types are represented by finite Te clusters in an anionic sublattice. The concentration of not-too-large clusters and their size distribution are known from the lattice percolation theory [5]. The deepest localized states are formed at the isolated clusters, while the shallower states spread over two or several Te clusters to form superclusters. The mobility threshold, below which are only the states localized at the isolated clusters and finite superclusters, corresponds to the energy for which a percolation cluster arise due to the overlap between the wave functions of localized excitons.

However, the regions where the spatially isolated localized excitonic states occur are also present above the percolation threshold, although the number of such states rapidly decreases with a decrease in the localization energy. In particular, the absorption and luminescence data for the $\text{ZnSe}_{(1-c)}\text{Te}_c$ crystal studied in this work suggest that the mobility threshold at $c = 0.13$ lies near the localization energy of a four-atomic Te cluster [2, 3]. Although this scheme adequately describes the absorption and luminescence spectra, some unusual features of luminescence kinetics do not fit in with such a simple picture and call for a closer inspection of the disorder effect on electron motion in the conduction band.

To explain the main features of long-time luminescence decay, we assume that, subsequent to a relatively fast recombination of the majority of excitons that were localized as a whole immediately after the exciting pulse, some of the carriers remain separated. The appearance of the separated carriers may be imagined as a result of electron retardation in the relaxation of excited carriers. The holes in these solid solutions efficiently interact with the lattice and, as a result, rapidly occupy localized levels appearing in the potential relief of the valence band. Electrons lose energy far more slowly and do not always have time to adiabatically follow the holes, provided that the hole localization is deep and fast enough. A detailed picture depends on the

energy of the exciting photons and the character of the states in the conduction band.

1. A power law $t^{-\delta}$ may be considered as the simplest asymptotic form of slow luminescence decay. Such a dependence can be expected for a bimolecular annihilation in the “mean-field” approximation

$$dn_e/dt = dn_h/dt = -kn_en_h, \quad (1)$$

where $n_e \approx n_h$ are the mean electron and hole concentrations. If the reaction rate constant k is independent of time, the intensity will decrease following the Becquerel law $I(t) \sim (1 + t/\tau)^{-2}$, irrespective of whether the electrons are mobile or localized. This dependence was observed in [2] for a $\text{CdS}_{(1-c)}\text{Se}_c$ crystal upon excitation below the exciton mobility threshold.

If the reaction constant slowly decreases with time, $k \sim (1 + t/\tau)^{-1/2}$, the intensity should decay as $I(t) \sim (1 + t/\tau)^{-3/2}$. This dependence was observed for amorphous silicon and theoretically explained in [6] by the diffusion of electrons and holes in the presence of the Coulomb interaction between them. A similar dependence was obtained for $n_e \approx n_h$ in a different approach [7], where it was taken into account that in the course of the annihilation process the particles become nonuniformly distributed in space.

In this work, the asymptotic decay of a transient luminescence excited below the exciton mobility threshold was studied in a ZnSe-Te solid solution. The observed dependence is satisfactorily described by the expression

$$I(t) \sim [(1 + t/\tau)]^{-\delta} \quad (2)$$

over a wide time domain.

The observation of a long-time luminescence component suggests that some of the photons absorbed below the exciton mobility threshold generate spatially separated immobile carriers captured to the fluctuation levels. In such a situation, the localized excitons can radiatively recombine only through tunneling, similar to the donor-acceptor pairs [8].

2. Although the spectroscopic data do not provide direct information on the electronic states, one may assume that anionic substitution disturbs the potential relief in the conduction band as well. The presence of a tail of localized states near the conduction band, even if it is appreciably smaller on the energy scale than the valence band tail, inevitably adds complexity to the kinetics of relaxation of the separated electrons and formation of the localized excitons and, hence, to the character of luminescence decay. If the electronic and hole perturbations differ substantially on the energy scale, the shapes of the absorption and luminescence spectra will be determined by the valence band tail.

If the conduction band has a tail of localized states, then, depending on the electron energy, it may either be trapped by an isolated potential well; occupy one of the states of the complex (supercluster) formed by a finite

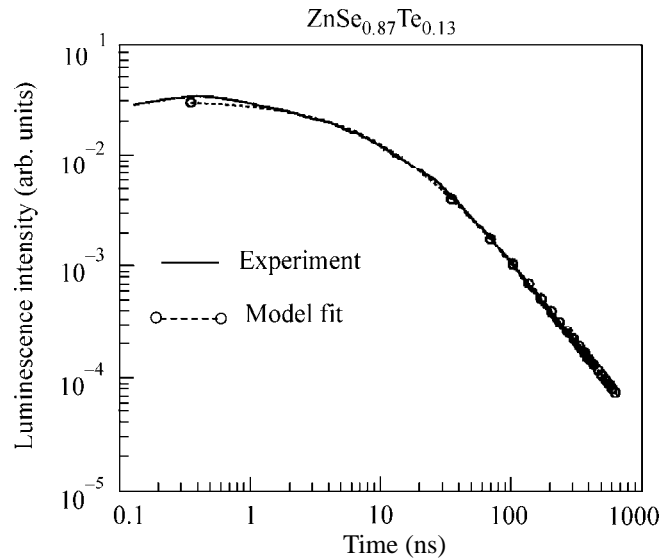


Fig. 1. Decay of integrated luminescence intensity of localized excitons (solid line) in $\text{ZnSe}_{(1-c)}\text{Te}_c$ with $c = 0.13$ after excitation below the mobility threshold. The dashed line is a fit by Eq. (2) with $\tau = 14.1$ ns and $\delta = 3/2$.

number of potential wells; or, finally, occupy one of the states of a percolation cluster in the conduction band. In the first case, the electron may be considered immobile and there is only one possibility for it to form an exciton, namely, through tunneling to the nearest localized hole. In the second case, the electron can move within a supercluster to form an exciton. Finally, in the third case, the electron, in principle, may be considered immobile, but the character of its motion depends on its kinetic energy. For high energies, the density of states is high and the disorder effect amounts to electron scattering. However, if the kinetic energy is low, the electron occupies the states formed by the overlapping wave functions of potential wells. In this energy range, the possible electron trajectories are limited by the geometry of the percolation cluster, whose nonuniform sizes may be characterized by the correlation length ξ , which rapidly decreases on moving away from the mobility threshold.

One can expect that, if the number of localized states in the conduction band tail is large, only a relatively small fraction of electrons will occur in the mobile states after above-threshold excitation. In this case, the long-time luminescence component acquires new features that can be described in terms of the theory of diffusion-controlled annihilation [9–11]. In particular, the luminescence kinetics will follow an exponential law with a fractional power (critical index of “normal” [9–16] or “anomalous” [9, 11] diffusion) of the time exponent.

The solution to the equation of normal diffusion provides the following asymptotic expression for the

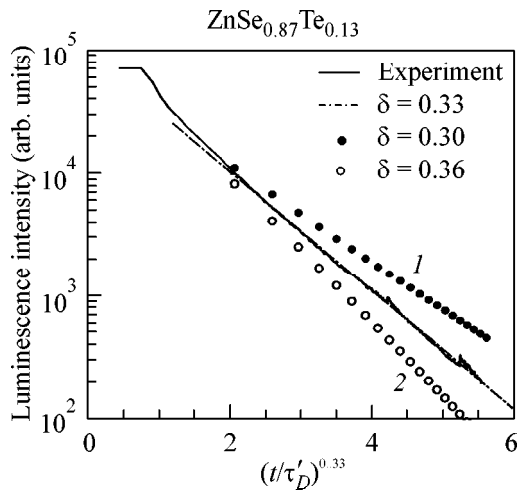


Fig. 2. Integrated luminescence intensity as a function of $t^{0.33}$ for $\text{ZnSe}_{0.87}\text{Te}_{0.13}$ (solid line) after excitation above the mobility threshold. The dashed line is a fit by Eq. (8) with $\tau_D' = 0.74$ ns and $\delta = 0.33$. Curves for $\delta = 0.30$ and 0.36 are labeled 1 and 2, respectively.

probability that a mobile electron will survive for a time t in a sphere of radius R [17]:

$$P(R, t) \sim \exp\left\{-\gamma_d \frac{Dt}{R^2}\right\}, \quad (3)$$

where d is the dimensionality of the space, γ_d is a constant depending on the dimensionality, and D is the diffusion coefficient. Note that if the electron and hole concentrations are different, a function of this type is obtained from Eq. (1).

For a random hole distribution in the crystal, the probability to find a sphere with radius R free of localized holes is

$$P_0(R) = \exp\{-n_h R^d C_d\}, \quad (4)$$

where $C_d = 2\pi^{d/2}/d\Gamma(d/2)$ and $\Gamma(d/2)$ is the gamma function. The averaging of Eq. (4) over all possible domain sizes using the optimization procedure [17] gives the following optimum value R_{opt} for the radius of the survival domain:

$$R_{opt} = \left(\frac{2\gamma_d Dt}{dC_d n_h}\right)^{d/(d+2)}. \quad (5)$$

As a result, the probability for mobile electrons to survive in the above optimum domains and, hence, the time-dependent electron concentration is given by the

expression of the form

$$P_{opt} = \exp\left\{-(1 + 2/d)\gamma_d^{d/(d+2)} \times \left(\frac{dC_d}{2}\right)^{d/(d+2)} n_h^{2/(d+2)} (Dt)^{d/(d+2)}\right\}. \quad (6)$$

It follows from Eq. (6) that the logarithm of the luminescence intensity is proportional to a fractional power of t :

$$-\ln(I(t)) \sim [t/\tau_D']^{d/(d+2)}, \quad (7)$$

giving the normal-diffusion exponent $\delta = 0.6$ for $d = 3$.

If the sizes of the diffusion domains making the optimum contribution to the band intensity are smaller than, or comparable with, the correlation length of the percolation cluster [11], i.e., if $R_{opt} \leq \xi$, the diffusion regime becomes anomalous and the dimensionality d in Eq. (7) should be replaced by the ‘‘hyperuniversal’’ fraction dimensionality [18, 19], i.e., by the spectral dimensionality of the percolation cluster d_s , which is deemed almost independent of the dimensionality of the system [11, 18, 19]:

$$-\ln(I(t)) \sim [t/\tau_D']^{d_s/(d_s+2)} = [t/\tau_D']^\delta, \quad (8)$$

where $d_s = 2d_f/d_w$, d_f is the fraction dimensionality ($d_f \approx 2.51$ for three-dimensional space [20]), and d_w is the index of fraction dimensionality of random walk [11] ($d_w \approx 3.8$ for $d = 3$ and $\delta \approx 0.4$); i.e., the process markedly slows down if, instead of normal diffusion, the motion proceeds over the states of the percolation cluster.

The process may be further decelerated if diffusion proceeds partially over the finite superclusters. In this case, d in Eq. (7) should be replaced by the $2d_f/d_w'$ index, where $d_w' = d_w/(1 - \beta/2\nu)$ [11] (β and ν are the critical indices of the order parameter and the correlation length, respectively [20]) and $d_w' \approx 5.01$ for $d = 3$ [11].

The time-dependent integrated intensity is shown in Fig. 2 for a ZnSe–Te solid solution excited above the exciton mobility threshold. This dependence is described over a wide time interval by an exponential function with diffusion critical index $d_f/(d_f + d_w') \approx 0.33$.

With a rise in temperature, the mobile electrons with thermal kinetic energy become dominant in the diffusion process. As the electron energy increases, ξ should decrease and the ratio between R_{opt} and ξ should change, leading to the acceleration of diffusion and an increase in the critical index.

The temperature-induced changes in the luminescence decay kinetics are shown in Fig. 3. The curve fitting procedure suggests that the experimental data are

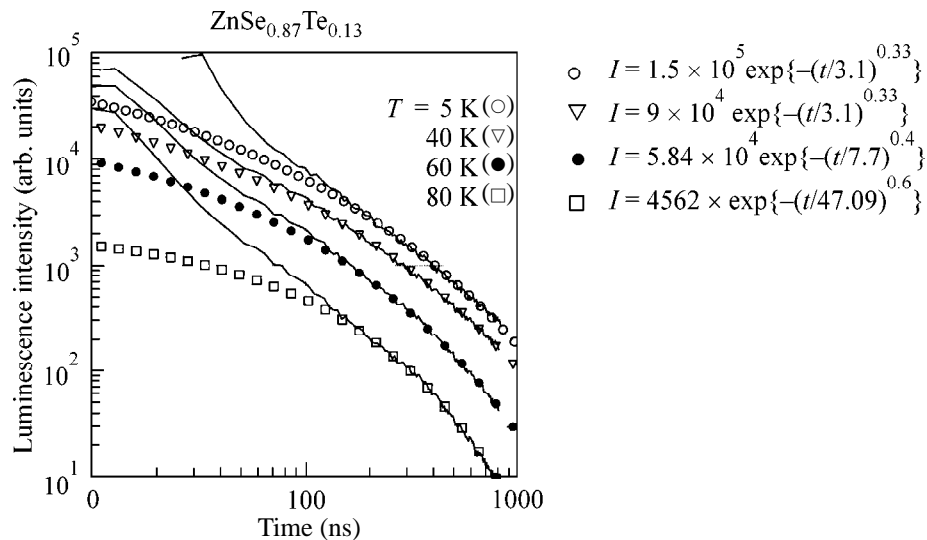


Fig. 3. Temperature-induced changes in the decay rate for the integrated luminescence intensity of the $\text{ZnSe}_{0.87}\text{Te}_{0.13}$ crystal.

described by the function $\exp(-[t/\tau_D']^\delta)$, with the critical index δ changing from 0.33 to 0.6 as the temperature changes from 5 to 80 K. A crossover to normal diffusion at $T = 80$ K indicates that the thermal energy of electron delocalization is about 5 meV. The temperature at which the diffusion becomes normal determines the scale of electron band rearrangement. Considering that the Urbach parameter for $\text{ZnSe}_{(1-c)}\text{Te}_c$ in the concentration range studied is about 25 meV, the scale of conduction band edge smearing is at least five times smaller. For such a ratio between parameters, the influence of the fluctuation potential of the conduction band on the spectrum of localized excitons is negligible, although the long-time luminescence kinetics would be difficult to explain without taking it into account.

This work was supported in part by the Deutsche Forschungsgemeinschaft, the Russian Foundation for Basic Research, and the program "Physics of Solid-State Nanostructures."

REFERENCES

1. A. Reznitsky, A. Naumov, S. Verbin, *et al.*, *J. Lumin.* **47**, 297 (1991).
2. A. Klochikhin, A. Reznitsky, S. Permogorov, *et al.*, *Phys. Rev. B* **59**, 12947 (1999).
3. A. A. Klochikhin, S. A. Permogorov, and A. N. Reznitskii, *Zh. Éksp. Teor. Fiz.* **115**, 1039 (1999) [*JETP* **88**, 574 (1999)].
4. A. A. Klochikhin, S. A. Permogorov, and A. N. Reznitskii, *Fiz. Tverd. Tela (St. Petersburg)* **39**, 1170 (1997) [*Phys. Solid State* **39**, 1035 (1997)].
5. M. F. Sykes, D. S. Gaunt, and M. Glen, *J. Phys. A* **9**, 1705 (1976).
6. J. Noolandi, K. M. Hong, and R. A. Street, *Solid State Commun.* **34**, 45 (1980).
7. V. N. Kuzovkov and E. A. Kotomin, *Chem. Phys.* **81**, 335 (1983).
8. D. G. Thomas, J. J. Hopfield, and W. M. Augustyniak, *Phys. Rev.* **140**, A202 (1965).
9. S. Havlin and D. Ben-Avraham, *Adv. Phys.* **36**, 695 (1987).
10. V. Kuzovkov and E. Kotomin, *Rep. Prog. Phys.* **51**, 1479 (1988).
11. S. Havlin and A. Bunde, *Percolation II in Fractals and Disordered Systems*, Ed. by A. Bunde and S. Havlin (Springer-Verlag, Berlin, 1994), p. 97.
12. B. Ya. Balagurov and V. G. Vaks, *Zh. Éksp. Teor. Fiz.* **65**, 1939 (1973) [*Sov. Phys. JETP* **38**, 968 (1974)].
13. A. A. Ovchinnikov and Ya. B. Zeldovich, *Chem. Phys.* **28**, 215 (1978).
14. P. Meakin and H. E. Stanley, *J. Phys. A* **17**, L173 (1984).
15. K. Kang and S. Redner, *Phys. Rev. Lett.* **52**, 955 (1984).
16. N. D. Donsker and S. R. S. Varadhan, *Commun. Pure Appl. Math.* **32**, 721 (1979).
17. P. Grassberger and I. Procaccia, *J. Chem. Phys.* **77**, 6281 (1982).
18. S. Alexander and R. Orbach, *J. Phys. Lett.* **43**, L625 (1982).
19. T. Nakayama, K. Yakubo, and R. Orbach, *Rev. Mod. Phys.* **66**, 381 (1994).
20. A. Bunde and S. Havlin, *Percolation I in Fractals and Disordered Systems*, Ed. by A. Bunde and S. Havlin (Springer-Verlag, Berlin, 1991), p. 51.

Translated by V. Sakun

Screening of Excitonic States by Low-Density 2D Charge Carriers in GaAs/AlGaAs Quantum Wells

S. I. Gubarev*, I. V. Kukushkin*, S. V. Tovstonog*, M. Yu. Akimov*,
J. Smet**, K. von Klitzing**, and W. Wegscheider***

* *Institute of Solid-State Physics, Russian Academy of Sciences, Chernogolovka, Moscow region, 142432 Russia*
e-mail: gubarev@issp.ac.ru

** *Max-Planck-Institut für Festkörperforschung, 70569 Stuttgart, Germany*

*** *Walter Schottky Institute, Technische Universität München, D-85748 Garching, Germany*

Received August 21, 2000

Screening of excitonic states by a system of 2D electrons (or holes) in GaAs/AlGaAs single quantum wells is studied. With increasing concentration of 2D charge carriers, a threshold-type disappearance of excitonic states is observed in both luminescence and reflectance spectra. The higher the quality of the 2D system, the lower the corresponding threshold concentration. In the best systems, the collapse of excitonic states occurs at unexpectedly low electron densities $n_e = 5 \times 10^9 \text{ cm}^{-2}$, which correspond to the mean dimensionless distance between the particles $r_s = 8$. This value far exceeds the threshold values observed for 3D systems ($r_s \approx 2$), as well as the values obtained for quantum wells in previous studies. The problem of measuring the concentration of low-density 2D charge carriers in photoexcitation conditions is solved by applying the method of optical detection of the dimensional magnetoplasma resonance. This method provides reliable measurements of the density of a 2D system to the values about 10^9 cm^{-2} . © 2000 MAIK “Nauka/Interperiodica”.

PACS numbers: 73.20.Dx; 71.35.Cc

Free charge carriers screen the Coulomb interaction between photoexcited electrons and holes in a semiconductor, so that at a certain concentration of these carriers, the formation of bound excitonic states in the electron (hole) plasma becomes impossible. The collapse of bound excitonic states because of screening of the Coulomb interaction by free charge carriers was studied experimentally on bulk semiconductors with different doping levels, as well as under conditions of optical excitation [1, 2]. From these studies, it followed that the typical concentration at which the excitonic states collapse corresponds to the mean dimensionless distance between the particles (expressed in terms of the Bohr radius of the exciton) $r_s \approx 2$ [2]. This value of the threshold concentration agrees well with the results of the theoretical calculations performed for an electron–hole plasma [3]. Thus, by now it is agreed that, in 3D systems, the screening of excitonic states occurs at concentrations corresponding to the interparticle spacing $r_s \approx 2$. However, it should be noted that, in the aforementioned studies, the screening of excitonic states was caused not by a charged (electron or hole) system, but by a neutral electron–hole plasma, in which the concentrations of electrons and holes are equal.

With the appearance of 2D electron systems, the question about the specific features of the screening of excitonic states by 2D electrons has become topical. In contrast to 3D systems, in single quantum wells, selective doping of the barrier by impurities makes it possi-

ble to spatially separate positively charged impurities from electrons, so that a low-density metallic 2D electron channel can coexist in the well with photoexcited excitons. It is these systems that allow one to experimentally study the screening of excitonic states as a function of increasing concentration of 2D electrons in the quantum well. We note once again that, in this case, we are dealing with the screening of excitons by a charged electron system rather than by a neutral electron–hole plasma, as in the case of 3D objects.

It is common knowledge that in 2D systems the screening of the Coulomb interaction by free carriers is less effective than in the 3D case. Specifically, in the 2D case, the screened Coulomb potential decreases at large distances according to a power law [4], whereas, in a 3D gas, the screened potential exhibits exponential decay. Besides, it is known that, in 2D systems, the formation of localized states occurs at potentials as low as one likes. Based on these considerations, it was believed that, in quasi-two-dimensional systems, the screening of the Coulomb potential is much weaker than in the 3D case, and therefore the collapse of excitonic states in quantum wells should occur at carrier concentrations corresponding to the interparticle spacing $r_s < 2$ [5].

Just these values were obtained for the threshold concentration from the first studies of the screening of excitons by 2D electrons [6]. In the cited experiments, exciton collapse was observed in GaAs/AlGaAs struc-

tures at electron densities of about 10^{11} cm^{-2} , which corresponds to the parameter $r_s = 1.9$. However, the quantum wells used in these studies were characterized by very large fluctuations of the random potential, so that the delocalization of 2D electrons in these structures occurred at the same high concentrations of 2D charge carriers as the disappearance of excitonic states from the spectrum. Thus, it remained unclear whether the appearance of excitonic states observed with decreasing electron density was related to the reduced effect of screening or was a result of the localization of 2D charge carriers in the random potential.

From the results of experiments [7, 8] with CdTe/CdMgTe and ZnSe/ZnMgSe 2D structures, it followed that ionization of free excitons occurs at concentrations corresponding to large values of r_s . However, because of the lack of measurements of the carrier concentrations in these structures, the values obtained in these experiments for the threshold concentrations corresponding to the screening of excitonic states can only be considered as estimates.

The purpose of our study was to experimentally investigate the screening of excitonic states by 2D charge carriers in high-quality GaAs/AlGaAs single quantum wells with simultaneous measurements of the concentration of the 2D system under photoexcitation conditions. We studied the disappearance of the free exciton line from the luminescence spectra and the reflectance spectra; the density of the 2D channel was determined by the method of dimensional magnetoplasma resonance, which was optically detected simultaneously with the measurements of the luminescence and reflectance spectra.

The studies were performed on GaAs/AlGaAs single quantum wells of width 200–300 Å by using both selectively doped (with the carrier concentration $n_e = 1.4 \times 10^{11} \text{ cm}^{-2}$) and undoped structures. The presence of residual impurities in the undoped structures caused the formation of low-density 2D channels of either the electron or hole type (with the charge carrier concentration of about $n_{e(h)} = (1-2) \times 10^{10} \text{ cm}^{-2}$). The carrier concentration in the channel was smoothly varied by illuminating the structure with the combined radiation from two sources of light: a semiconductor laser generating the wavelength $\lambda = 7500 \text{ Å}$ (for intrawell photoexcitation) and a He–Ne laser with $\lambda = 6328 \text{ Å}$ (for barrier photoexcitation). The use of a combined photoexcitation of the barrier and the well provided the possibility to decrease the density of the 2D channel from the maximum one (which was different for different structures) to $2 \times 10^9 \text{ cm}^{-2}$. In some structures, it was even possible to change the type of carriers in the well from n -type ($n_e \approx 10^{10} \text{ cm}^{-2}$) to p -type ($n_h \approx 10^{10} \text{ cm}^{-2}$) by passing through the zero concentration of the majority carriers.

Optical measurements were performed at $T = 1.5 \text{ K}$ by using a three-light-guide technique, which allowed simultaneous measurements of the reflectance and

luminescence spectra under the same optical excitation conditions. The charge carrier concentration in the channel was determined by optical detection of the dimensional magnetoplasma resonance. For this purpose, mesas in the form of disks 0.1 to 1 mm in diameter were fabricated on the structures under study, and the samples were placed in an antinode of the microwave electric field in the waveguide. We studied the dependences of the differential luminescence signal formed as a result of modulation of the microwave excitation power on the magnetic field for different fixed frequencies (within 16–40 GHz).

Figure 1 shows the changes that occur in the luminescence and reflectance spectra of an undoped quantum well with variation of the carrier concentration in the 2D channel. This particular figure illustrates the screening of excitons by a hole channel; for the case of an electron system, the behavior of the spectra was precisely the same. At high concentrations (Fig. 1a), the X^+ line corresponding to a localized charged trion dominates the luminescence and reflectance spectra [9]. As the concentration of 2D carriers (holes in the case of Fig. 1) decreases the intensity of the trion emission line decreases and the X line corresponding to the free exciton emission appears in the spectrum (Figs. 1b, 1c). This line dominates the luminescence spectrum observed for the lowest densities of 2D carriers (Fig. 1d). A similar behavior is observed for the X^- and X^+ lines in the reflectivity spectra. In the case of low concentrations, the latter exhibit only the free exciton line X (Fig. 1d), corresponding to the excitonic state of an electron and a heavy hole. This line abruptly disappears from the reflectance spectra when the concentration of 2D carriers in the well reaches some threshold value. Thus, as one can see from Fig. 1, the collapse of the excitonic state manifests itself as a threshold-type disappearance of the exciton line from both the luminescence spectrum and the reflectance spectrum.

One of the most subtle questions that arises in studies of the optical properties of a 2D electron system is the determination of the concentration of 2D carriers in the presence of optical illumination. In the case of an electron channel with electron concentrations of about $n_s = 3 \times 10^{10} - 3 \times 10^{11} \text{ cm}^{-2}$, the value of n_s can be determined from the magnetoluminescence spectra by the Landau quantization of the electron energy spectrum [10]. In samples with high-mobility charge carriers, the Landau quantization in the luminescence spectra can be observed in magnetic fields of about 0.2 T. From the number of fully occupied Landau levels and from the variation of this number with magnetic field, one can reliably determine the 2D electron density [10]. However, this method does not apply in the case of a 2D hole channel (because of the large hole mass and the complex structure of the valence band) or in the case of a low-density 2D electron gas with $n_e < 2 \times 10^{10} \text{ cm}^{-2}$. For such low concentrations, it is also impossible to use

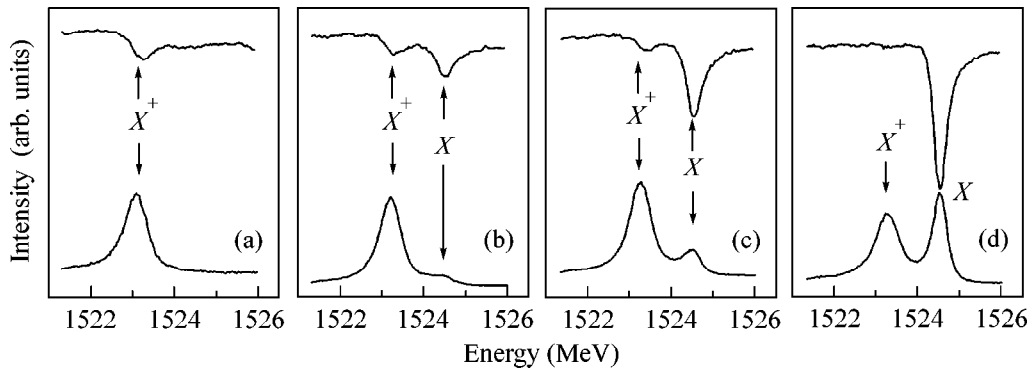


Fig. 1. Luminescence and reflectance spectra measured for a GaAs/AlGaAs quantum well with different carrier concentrations in the 2D channel (the concentration decreases from plot (a) to plot (d)). The arrows indicate the spectral positions of the free exciton X and the positively charged trion localized by impurities in the barrier X^+ .

transport measurements because of the appearance of unsolvable contact problems.

To determine the carrier concentration in low-density 2D systems under photoexcitation conditions, we used the method of dimensional magnetoplasma resonance. In a 2D electron system of finite dimensions, a mixing of cyclotron and plasma modes takes place, which leads to the dependence of the magnetoplasma resonance frequency on both the 2D carrier concentration and the structure dimensions [11, 12]. For a mesa in the form of a disk with diameter d , the frequencies of the upper and lower magnetoplasma modes are described by the expression

$$\omega_{DMR} = \pm \frac{\omega_{CR}}{2} + \sqrt{\omega_p^2 + \left(\frac{\omega_{CR}}{2}\right)^2}, \quad (1)$$

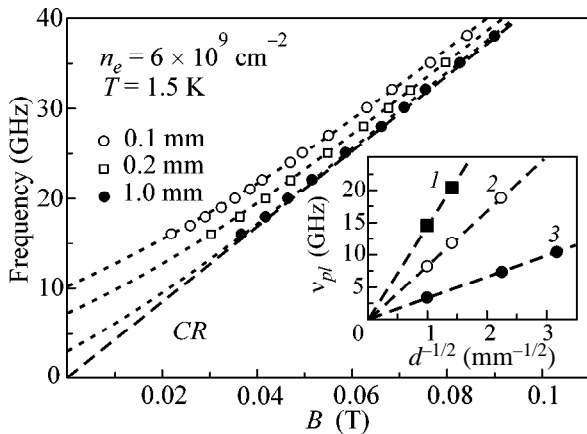


Fig. 2. Experimental magnetic-field dependence of the dimensional magnetoplasma resonance for mesas of different diameters d in the case of a low-density 2D electron system. The inset shows the experimental dependence of the plasma frequency ν_{pl} on the mesa diameter d for three values of the 2D electron density: $n_e = (1) 3 \times 10^{11}$, $(2) 4 \times 10^{10}$, and $(3) 6 \times 10^9 \text{ cm}^{-2}$.

where $\omega_{CR} = eB/m^*$ is the cyclotron frequency and

$$\omega_p^2 = 3\pi^2 n_s e^2 / 4m^* \epsilon_{\text{eff}} d \quad (2)$$

is the plasma frequency of 2D charge carriers with the concentration n_{2D} , where $\epsilon_{\text{eff}} = (1 + \epsilon_0)/2$ is the effective dielectric constant and m^* is the effective mass.

Figure 2 presents the experimental dependence of the resonance magnetic field (for the upper branch of the magnetoplasma resonance) on the microwave excitation frequency for mesas with different diameters. From this figure, one can see that, at a fixed microwave excitation frequency, a decrease in the mesa diameter shifts the resonance toward lower magnetic fields, which corresponds to an increase in the plasma frequency contribution to Eq. (1). Figure 2 also shows the calculated dependence of the magnetoplasma resonance frequency on the magnetic field; the calculations were performed by Eq. (1) for mesas of different diameters with a single adjustable parameter n_s . One can see that, from this approximation of the experimental data, it is possible to determine the plasma frequency ω_p as the value of the resonance frequency in the field $B = 0$. The inset of Fig. 2 shows the experimental dependence of the plasma frequency ν_{pl} on the mesa diameter d for three different concentrations of the 2D electron system. From this figure, it follows that the plasma frequency is proportional to $d^{-1/2}$ [according to Eq. (2)], and the slope of the linear dependence is governed by the electron density. The concentration of 2D electrons that was determined by the method of dimensional magnetoplasma resonance proved to be coincident with the results of transport and magneto-optic measurements, which were possible in the presence of a weak photoexcitation at relatively high 2D electron densities.

Studies of the magnetoplasma resonance not only allow one to accurately determine the charge carrier concentration up to values of about $n_s = 10^9 \text{ cm}^{-2}$, but also provide the measurement of the momentum relaxation time, which characterizes the quality of the structure. For the best samples, the half-width of the reso-

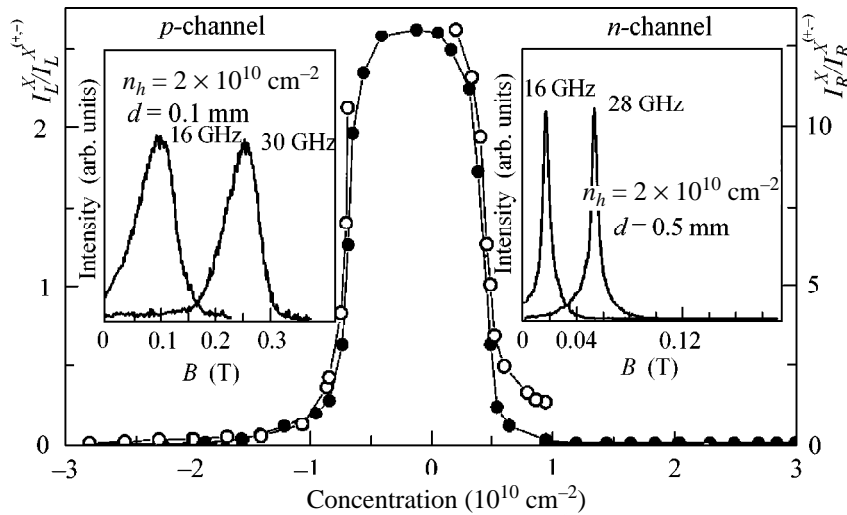


Fig. 3. Intensity ratio of the spectral lines corresponding to free and charged excitons (the X and $X^{(+,-)}$) versus the concentration of electrons (positive concentration values) and holes (negative concentration values) for the measured (\bullet) luminescence and (\circ) reflectance spectra. The insets show the characteristic spectra of the dimensional magnetoplasma resonance for the n -channel (electron resonance) and the p -channel (hole resonance).

nance line was less than 0.0025 T, which corresponds to an electron scattering time of 200 ps. In the case of very low concentrations, the scattering time decreases and the resonance peak broadens; nevertheless, for mesas with a diameter of 0.1 mm, reliable measurements of electron density were possible up to concentrations of about 10^9 cm^{-2} . As the electron density decreased and the transition from the electron channel to the hole one occurred, the intensity of the line corresponding to the electron magnetoplasma resonance decreased and the hole resonance line appeared in the spectrum, the latter line being observed at noticeably higher magnetic fields (see the insets of Fig. 3). In the case of a hole channel, the behavior of the magnetoplasma resonance can also be adequately described by Eq. (1) and allows one to determine both the mass and the concentration of 2D holes.

Figure 3 shows the ratio between the intensities of the lines corresponding to free and charged excitons (the X and $X^{(+,-)}$ lines) versus the concentration of electrons (positive concentration values) and holes (negative concentration values). One can see that the intensity ratios of the X and $X^{(+,-)}$ lines observed for the reflectance and luminescence spectra exhibit a synchronous sharp drop at the same threshold density of charge carriers in the 2D channel. The critical concentrations at which exciton screening occurred in the best structures in our experiment proved to be unexpectedly low: $n_e = 5 \times 10^9$ cm^{-2} for the electron channel and $n_h = 7 \times 10^9$ cm^{-2} for the hole channel. Studies of quantum wells of different quality showed that, as the quality of the structures became lower (i.e., the resonance peak became broader at the same charge carrier concentration), the threshold changes in the exciton spectrum shifted toward higher densities of the 2D system. For

example, in low-quality structures in which the relaxation time decreased by no more than an order of magnitude (down to 10 ps), the threshold density reached values of about $n_e = 5 \times 10^{10}$ cm^{-2} .

The values of the threshold concentration of free charge carriers at which the collapse of excitonic states occurs in the best quantum wells studied in our experiment correspond to the dimensionless interparticle spacing $r_s = 8$. This value noticeably exceeds the critical value $r_s = 2$ obtained for 3D systems. One possible explanation for this result may be that, in the 3D case, it is practically impossible to implement the screening of a single exciton by a charged electron plasma. On the other hand, studies of exciton collapse in these systems have always been performed for an electron-hole plasma with equal concentrations of electrons and holes.

Thus, the study of the reflectance and luminescence spectra showed that the screening of free excitons in a quantum well occurs in a threshold-type manner and at unexpectedly low concentrations of free charge carriers. The method of optical detection of the dimensional magnetoplasma resonance, which was used in our experiments, allowed us to accurately determine the charge carrier density (for both electrons and holes) at which exciton collapse takes place. It was found that the critical concentration corresponding to the screening of excitonic states decreases with improving quality of the structures.

This work was supported by the Russian Foundation for Basic Research and by the INTAS (project no. 99-1146).

REFERENCES

1. T. Rice, J. Hensel, T. Phillips, and G. Tomas, *Solid State Phys.* **32**, 1 (1977); *The Electron Hole Liquid in Semiconductors: Theoretical Aspects. Experimental Aspects* (Mir, Moscow, 1980), p. 127.
2. I. V. Kukushkin *et al.*, *Zh. Éksp. Teor. Fiz.* **84**, 1145 (1983) [*Sov. Phys. JETP* **57**, 665 (1983)].
3. V. E. Bisti and A. P. Silin, *Fiz. Tverd. Tela* (Leningrad) **20**, 1850 (1978) [*Sov. Phys. Solid State* **20**, 1068 (1978)].
4. T. Ando *et al.*, *Rev. Mod. Phys.* **54**, 437 (1982).
5. G. E. W. Bauer, *Phys. Rev. B* **45**, 9153 (1992).
6. G. Finkelstein, H. Strikman, and I. Bar-Josef, *Phys. Rev. Lett.* **74**, 976 (1995).
7. V. Huard *et al.*, *Phys. Rev. Lett.* **84**, 187 (2000).
8. W. Ossau *et al.*, *Physica B* (Amsterdam) **256–258**, 323 (1998).
9. O. V. Volkov, S. V. Tovstonog, I. V. Kukushkin, *et al.*, *Pis'ma Zh. Éksp. Teor. Fiz.* **70**, 588 (1999) [*JETP Lett.* **70**, 595 (1999)].
10. I. Kukushkin and V. B. Timofeev, *Adv. Phys.* **45**, 147 (1996).
11. B. A. Allen, Jr., H. L. Stormer, and J. C. M. Hwang, *Phys. Rev. B* **28**, 4875 (1983).
12. B. M. Ashkinadze *et al.*, *Phys. Rev. Lett.* **83**, 812 (1999).

Translated by E. Golyamina

Suppression of the Local Jahn–Teller Effect in Nanostructures: Self-Trapped Holes and Excitons in AgCl Nanocrystals

P. G. Baranov, V. S. Vikhnin, N. G. Romanov*, and V. A. Khrantsov

*Ioffe Physicotechnical Institute, Russian Academy of Sciences, Politekhnikeskaya ul. 26,
St. Petersburg, 194021 Russia*

* e-mail: Nikolai.Romanov@pop.ioffe.rssi.ru

Received August 22, 2000

A strong decrease in the g -factor anisotropy was revealed by optically detected magnetic resonance for self-trapped Jahn–Teller holes (both isolated and forming self-trapped excitons) in AgCl nanocrystals embedded into the KCl crystal lattice. This is evidence for considerable suppression of the Jahn–Teller effect in nanoobjects. The suggested mechanism of suppression of the Jahn–Teller effect in nanocrystals is associated with an additional deformation field arising in nanocrystals owing to a strong vibronic interaction at the interface.
© 2000 MAIK “Nauka/Interperiodica”.

PACS numbers: 71.35.Aa; 71.70.Ej; 76.70.Hb

Semiconductor nanocrystals introduced into solid matrices (as a rule, glasses or organic materials) are of particular interest for the development of physics of low-dimensional structures and the design of new materials. In recent years, a series of such systems have been fabricated with the use of various materials and technologies (see, e.g., [1, 2] and references therein). The formation of nanocrystals in alkali-halide crystal matrices was recently reported in [3, 4]. An important advantage of such systems is that they provide the possibility of designing systems of oriented nanocrystals.

Silver halides occupy an intermediate position between ionic and semiconductor crystals and possess unique properties that are favorable to widespread use of these materials in photography [5]. Insofar as the band gap in AgCl (3.237 eV) is much narrower than in KCl (≈ 8.7 eV), AgCl nanocrystals in KCl can be considered as a system of quantum dots. Both large-radius states [self-trapped excitons (STEs) and shallow electron centers (SECs)] and strongly localized Jahn–Teller centers [self-trapped holes (STHs)] in bulk AgCl crystals have been well studied to date [6–8]. An STE represents a self-trapped hole capturing an electron to a delocalized $1s$ orbital ($a_B = 15$ Å), with the hole part of the STE retaining the STH properties [6]. The Jahn–Teller effect (JTE) is one of the fundamental local effects in the solid state, which is quite sensitive to internal fields and variations in electron–phonon interactions. Because of this, experimental and theoretical studies of the problem of the influence of nanoparticle size on the JTE are of great interest.

In this work, the method of optically detected magnetic resonance (ODMR) was used to study self-trapped holes, self-trapped excitons, and shallow electron centers in AgCl nanocrystals introduced into a KCl

crystal matrix. It was found that the g -factor anisotropy strongly decreases for self-trapped Jahn–Teller holes (both isolated and forming self-trapped excitons). A mechanism of suppression of the Jahn–Teller effect in nanocrystals is suggested.

KCl:AgCl crystals were grown by the Stockbarger technique. The silver concentration in the melt was 2%. ODMR at a frequency of 35 GHz and temperature of 1.6 K was detected from the luminescence excited by the UV light of an arc deuterium lamp with appropriate light filters. The microwave power in the cavity of an ODMR spectrometer was modulated at a sound frequency, and the microwave-induced changes in the luminescence intensity were detected using a lock-in detector. Samples were cleaved from different parts of a grown crystal and represented transparent single crystals without visible inclusions. Contrary to silver halides, alkali-halide crystals of the NaCl type can easily be cleaved along the $\{100\}$ planes, greatly facilitating sample orientation.

The luminescence spectra (a) and the corresponding ODMR spectra (b) are shown in Fig. 1 for three samples cleaved from different parts of a KCl:AgCl crystal with different silver concentrations. The ODMR spectra were detected from the change in the overall luminescence intensity in the range 450–600 nm for the crystal orientation $[001] \parallel B$ and the microwave power (100 mW) modulated at a frequency of 80 Hz. Curve 1 in Fig. 1b shows the positions of the ODMR lines corresponding to the STHs, STEs, and SECs in the AgCl bulk crystal. Because the tetragonal axes of STH and STE are aligned with one of the crystallographic axes $\langle 100 \rangle$, three types of centers are present. The \parallel and \perp signs label the ODMR lines of the centers whose Jahn–Teller distortion axes are parallel and perpendicular to

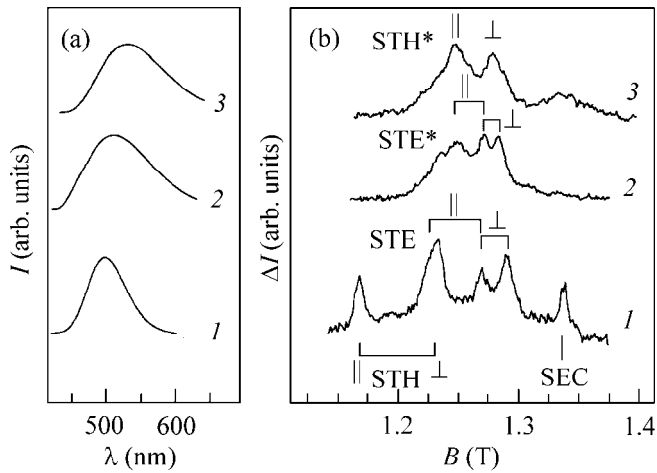


Fig. 1. (a) Luminescence and (b) ODMR spectra of samples 1, 2, and 3 (curves 1, 2, and 3, respectively) cleaved from different parts of a grown KCl:AgCl crystal (2% AgCl in the melt). The spectra were detected from the luminescence intensity under the following conditions: $T = 1.6$ K, $\nu = 35.2$ GHz, $P = 100$ mW, $f_{mod} = 80$ Hz, and $B \parallel [001]$. The positions of the ODMR lines corresponding to self-trapped holes (STH), self-trapped excitons (STE), and shallow electron centers (SEC) in bulk AgCl crystals are shown in the lower part of Fig. 1b. For ODMR spectrum (2), the positions of STE in the AgCl nanocrystals (STE*) are shown. For ODMR spectrum (3), the lines assigned to the STH in nanocrystals (STH*) are indicated. The \parallel and \perp signs refer to the centers whose axes are oriented parallel and perpendicular to the magnetic field, respectively.

the magnetic field B , respectively. The ODMR spectrum of sample 1 virtually coincides with the spectrum recorded under the same conditions for bulk AgCl crystals. It shows the same angular dependence and is characterized by the same parameters, $g_{\parallel} = 2.14$ and $g_{\perp} = 2.04$ for STH and $g = 1.88$ for SEC; for the triplet state of STE, g_{\parallel} and g_{\perp} are equal to the half-sum of the corresponding STH and SEC g factors and $D = -730$ MHz. The fact that the ODMR spectra recorded for the KCl:AgCl crystals with high silver concentration coincide with the spectra of the bulk AgCl crystals allows one to confidently state that KCl:AgCl contains AgCl microcrystals that are embedded into the KCl lattice, exhibit the properties of a bulk material, and are oriented like the matrix crystal.

The ODMR spectrum of sample 2 (curve 2 in Fig. 1b) shows lines corresponding to the triplet state, as well as the superimposed, less strong ODMR signals due to a center with spin $S = 1/2$ and axial g tensor $g_{\parallel} = 2.015$ and $g_{\perp} = 1.973$. These signals are more pronounced in the ODMR spectrum of sample 3 (curve 3 in Fig. 1b). To separate the signals from different centers, the ODMR spectra were recorded at different modulation frequencies of the microwave power.

The lines of the triplet ODMR spectrum are shown in Fig. 1b (curve 2) for two orientations of the tetragonal axis of the centers. The angular dependences of

ODMR spectra of a sample rotated in the (110) plane suggest axial symmetry with the $\langle 100 \rangle$ -type axis and can be rationalized in terms of a triplet spin Hamiltonian with parameters ($g_{\parallel} = 1.99$, $g_{\perp} = 1.96$, and $|D| = 335$ MHz) tangibly different from the STE parameters in bulk AgCl. We succeeded in observing forbidden transitions $\Delta m = \pm 2$ for the $[111] \parallel B$ orientation of this sample, confirming the triplet origin of the spectra. In [4], the triplet ODMR spectrum with the same parameters was assigned to the triplet STEs in AgCl nanocrystals having, according to atomic force microscopy, dimensions on the order of 50–70 Å. The distinctions in the luminescence and ODMR spectra of samples 1 and 2 are likely due to a decrease, from several micrometers to several nanometers, in the average sizes of the AgCl crystals embedded into KCl.

The ODMR spectrum of the aforementioned axial center with $S = 1/2$ may be assigned to the STHs in AgCl nanocrystals. Luminescence and ODMR spectra similar to spectra 3 were also recorded for sample 2 within two months after storing the sample in the dark at room temperature.

Hence, the g -factor anisotropy decreases for the STE and STH by more than half upon passing from bulk AgCl crystals (and large enough AgCl “microcrystals” embedded into the KCl lattice) to nanocrystals. Indeed, in the bulk AgCl crystals, $g_{\parallel} - g_{\perp} = 0.107$ for the STH and 0.054 for the STE. In the nanocrystals, these values are equal to 0.042 and 0.025 for the STH and STE, respectively.

The g -factor anisotropy of the STH 2E state is determined by the effective Zeeman interaction of a Jahn–Teller center and is described by introducing the appropriate electron operators in the basis of the 2E state [9]:

$$\hat{U}_{\theta} = \frac{1}{6}[3\hat{L}_z^2 - L(L+1)]; \quad \hat{U}_{\epsilon} = \frac{\sqrt{3}}{6}[\hat{L}_x^2 - \hat{L}_y^2].$$

As the JTE decreases to zero, the average value of g factor tends to the value corresponding to the isotropic part of the Zeeman interaction, because $\langle \hat{U}_{\theta} \rangle \rightarrow 0$ and $\langle \hat{U}_{\epsilon} \rangle \rightarrow 0$. Therefore, a decrease in the anisotropy of the g factor of the STH ($S = 1/2$) in AgCl nanocrystals is a direct evidence of JTE suppression.

Let us consider the influence of the nanocrystal sizes on the JTE for the STH mainly located on the $(\text{AgCl}_6)^{4-}$ cluster inside the AgCl nanocrystal incorporated into the KCl crystal matrix. Due to partial hole localization on the Ag^+ ion, the doubly degenerate $4d^9$ electronic state of the latter interacts linearly with the e deformations of the cubic environment. This results in the $E \times e$ JTE.

In large AgCl 3D crystals, such that the boundary effect can be ignored, the vibronic $E \times e$ interaction is dominated by the e_c deformations of the $(\text{AgCl}_6)^{4-}$ cluster, with the frequency ω_c corresponding to the quasi-local e vibrations. These vibrations appear because of a

sizable contribution from the high-density short-wavelength phonon modes.

We consider a change in the energies of electron and hole states at the nanocrystal interface as a mechanism governing the JTE in nanocrystals. Let us assume that the nanocrystal size L_{\parallel} in some direction is much shorter than its sizes in the other two orthogonal directions, i.e., that the nanocrystal is shaped like a platelet. It is shown below that this limitation is not stringent, so that this mechanism is valid even for nanocrystals with a rather small shape anisotropy.

It should be noted that the energy gap jump of ~ 5 eV from KCl to AgCl occurs at a distance of $\Delta L \approx a$, where $a \approx 3$ Å is the mean lattice parameter. This results in a large vibronic coupling constant at the interface ($W \approx 1.7$ eV/Å). In the continuous medium approximation, the corresponding contribution U_{int} of the interface potential energy to the potential energy of the nanocrystal can be written as

$$\Delta U_{\text{int}} = \frac{3}{2} W \frac{\Delta L}{L_{\parallel}} U, \quad (1)$$

where U is the active (in our case, tetragonal) quasi-uniform lattice deformation in the nanocrystal. This deformation induces hole state splitting and results in the transition from the JTE to the Jahn–Teller pseudoeffect (JTPE) with ensuing weakening of the vibronic effect. By adding the elastic part

$$\Delta U_{\text{elastic}} = K_0 U^2 / 2 \quad (2)$$

of the potential energy associated with the U vibrations (K_0 is the elastic constant of this vibration) to Eq. (1) and minimizing the sum of Eqs. (1) and (2) with respect to U , one arrives at the following expression for the equilibrium lattice displacement U_{eq} in the nanocrystal:

$$U_{\text{eq}} = -\frac{3}{2} \frac{W \Delta L}{K_0 L_{\parallel}}. \quad (3)$$

Owing to the equilibrium tetragonal lattice distortion, the hole E state splits:

$$\Delta = 3 |WV_E| \frac{\Delta L}{K_0 L_{\parallel}}, \quad (4)$$

where V_E is the corresponding $E \times e$ vibronic coupling constant. Note that $\Delta \propto L_{\parallel}^{-1}$; i.e., the splitting is a smooth function of the nanocrystal size. Let us now take into account that the JTPE (as well as the JTE) is caused by a bilinear coupling between the quasi-local microcluster e_c vibrations and the quasi-homogeneous e vibrations of the nanocrystal in the vibronic interaction of interest. The greatest contribution to the JTPE (JTE) comes from the corresponding difference vibrations with frequency ω_{\perp} and reduced mass μ . Using the JTPE suppression criterion $\Delta \mu \omega_{\perp}^2 \geq (V_E^{\text{eff}})^2$, where

V_E^{eff} is the effective constant of vibronic interaction with the active difference vibrations, one obtains the following formula for the critical size L_c of a nanocrystal:

$$L_c = 3 |WV_E| \frac{\Delta L \mu \omega_{\perp}^2}{K_0 (V_E^{\text{eff}})^2}. \quad (5)$$

The JTPE occurs in crystals with $L_{\parallel} > L_c$, whereas in smaller crystals ($L_{\parallel} < L_c$), the effect is suppressed.

It was assumed above that the nanocrystal shape is essentially noncubic; i.e., the size in the direction of tetragonal deformation is much shorter than the sizes in the perpendicular plane. This assumption does not influence the short-range interaction in the STH nearest surroundings which determines the symmetry of the spin Hamiltonian in the absence of the JTE. However, the JTE may be quite sensitive to the long-range interface field.

Let us discuss the more general case of close nanocrystal sizes L_x , L_y , and L_z in different orthogonal directions. Assume that $L_x \approx L_y \geq L_z = L_{\parallel}$. We will consider vibronic interaction (1) with the whole quasi-acoustic phonon spectrum and include not only the quasi-uniform deformation, but also the whole spectrum of deformations in the range $(\pi/L_{\parallel}) < k_z < (\pi/a)$, $(\pi/L_x) < k_x < (\pi/a)$, $(\pi/L_y) < k_y < (\pi/a)$, where a is the lattice parameter. In this case, Eqs. (4) and (5) obtained for the plate-shaped nanocrystals remain valid upon the substitution

$$\frac{W \Delta L}{K_0 L_{\parallel}} \Rightarrow \frac{2 \tilde{W} a}{\pi \mu_0 V^2 (L_{\parallel} L_{\perp}^2)^{1/3}} \ln \left(\frac{L_{\parallel}}{L_{\perp}} \right), \quad (6)$$

where μ_0 and V are, respectively, the reduced mass and the mean sound velocity for the quasi-acoustic phonons in the nanocrystal; \tilde{W} is the vibronic coupling constant for the interaction between the interfacial electronic states and the deformation tensor corresponding to the quasi-acoustic phonons; and $L_{\perp} = L_x \approx L_y$. One can see that the JTPE suppression effect smoothly (logarithmically) depends on L_{\parallel}/L_{\perp} and is absent for cube-shaped nanocrystals ($L_{\parallel} = L_{\perp}$).

Thus, vibronic coupling at the interface brings about weakening or suppression of the JTPE in sufficiently small-sized nanocrystals. This results in a decrease or suppression of the anisotropy in the EPR (ODMR) spectra of STH; i.e., the difference $g_{\parallel} - g_{\perp}$ decreases. Inasmuch as the STE is formed through electron capture by the STH, the anisotropy of the STE g tensor should also decrease or be suppressed. It is this decrease that was observed for the anisotropy of ODMR spectra in our experiments.

Estimates show that the mechanism considered can explain the JTE suppression effect for the STHs and

STEs in AgCl nanocrystals of sizes $L < 100 \text{ \AA}$. This seems to be reasonable for the system under study and is in line with the data of atomic force microscopy [4].

In particular, for $\omega_- \approx \frac{1}{3} \omega_D$, where ω_D is the Debye frequency,

$\tilde{W} = 5 \text{ eV}$, $V_E^{\text{eff}} \approx V_E = 1 \text{ eV/\AA}$, $a = 3 \text{ \AA}$, $\Delta L = 6 \text{ \AA}$, and $L_x \approx L_y = L_\perp = 125 \text{ \AA}$, one obtains $L_\parallel \approx 96 \text{ \AA}$ for the critical nanocrystal size in the z direction. A critical size of the order of 100 \AA is retained even at $|(L_\perp - L_\parallel)/L_\parallel| \approx 0.1$, as follows from Eqs. (5) and (6).

It should be noted that the suggested interfacial vibronic mechanism of generating inner stress fields in nanocrystals is quite general and may be operative for the other nanostructures and thin films.

Note also that the above-described mechanism of altering the JTE character is not unique. In principle, at least two mechanisms may compete with it. The first one is associated with a change in the phonon spectrum of the nanocrystal. This may result in strengthening of the JTE because of an increase in the density of the JTE-active vibrational modes. The second mechanism leads to the weakening and suppression of the JTE because of the effect of image fields induced by the Coulomb and elastic fields of the Jahn–Teller center (STH in our case). Nevertheless, estimates show that the effect of the interfacial vibronic field described by Eqs. (1)–(6) dominates in the case of interest and leads to the suppression of the JTE.

This work was supported in part by the Russian Foundation for Basic Research (project no. 00-02-16950), the program “Physics of Solid-State Nanostructures” (project no. 99-3012), and the program “Fundamental Spectroscopy.”

REFERENCES

1. L. Bányai and S. W. Koch, *World Scientific Series on Atomic, Molecular and Optical Physics*, Vol. 2: *Semiconductor Quantum Dots* (World Scientific, Singapore, 1993).
2. U. Woggon, *Springer Tracts Mod. Phys.* **136**, 251 (1997).
3. M. Haselhoff and H.-J. Weber, *Phys. Rev. B* **58**, 5052 (1998).
4. H. Vogelsang, O. Husberg, U. Köhler, *et al.*, *Phys. Rev. B* **61**, 1847 (2000).
5. H. Kanzaki, *Photograph. Sci. Eng.* **24**, 219 (1980).
6. M. T. Bennebroek, A. Arnold, O. G. Poluektov, *et al.*, *Phys. Rev. B* **53**, 15607 (1996).
7. M. T. Bennebroek, A. Arnold, O. G. Poluektov, *et al.*, *Phys. Rev. B* **54** (16), 11276 (1996).
8. J. Spoonhower and A. P. Marchetti, *J. Phys. Chem. Solids* **51**, 793 (1990).
9. A. Abraham and B. Bleaney, *Electron Paramagnetic Resonance of Transition Ions* (Clarendon, Oxford, 1970; Mir, Moscow, 1973), Vol. 2, p. 249.

Translated by V. Sakun

Tunneling Spectroscopy of Localized States near the Quantum Hall Edge¹

A. Alekseev, V. Cheianov*, A. P. Dmitriev*, and V. Yu. Kachorovskii

Uppsala University, Uppsala S-751 08, Sweden

Ioffe Physicotechnical Institute, Russian Academy of Sciences, Politekhnikeskaya ul. 26, St. Petersburg, 194021 Russia

* e-mail: sheianov@helene.teorfys.uu.se; dmitriev@vip1.ioffe.rssi.ru

Received August 23, 2000

In this paper, we discuss the experimental results of M. Grayson *et al.* on tunneling I – V characteristics of the quantum Hall edge. We suggest a two-step tunneling mechanism involving localized electron states near the edge, which might account for the discrepancy between the experimental data and the predictions of the chiral Luttinger liquid theory of the quantum Hall edge. © 2000 MAIK “Nauka/Interperiodica”.

PACS numbers: 73.40.Hm

Measuring the tunneling current from a normal metal to a quantum Hall (QH) edge is an attractive way to observe the Luttinger liquid behavior of QH edge states. Scaling invariance of the Luttinger liquid should leave a clear signature in the I – V characteristic of the tunneling current in the form of a power law dependence of the current on the applied voltage [1]

$$I \sim V^\alpha. \quad (1)$$

Moreover, the value of the tunneling exponent α would give knowledge of the decay law of the electron Green's function at the edge, which would provide a direct check of the chiral Luttinger liquid theories of the edge states [1–3].

The predictions of the chiral Luttinger liquid theory of the QH edge states can be summarized as follows.

(1) If a QH state belongs to the principal (Laughlin) sequence of filling factors $\nu = 1/(2p + 1)$ (p integer), it supports one gapless chiral edge mode. In this case, the tunneling exponent is given by

$$\alpha = 1/\nu. \quad (2)$$

(2) In a more general case of incompressible QH states corresponding to Jain filling factors $\nu = N/(2Np + 1)$, there are $|N|$ edge modes and the calculations [1, 2] based on the Luttinger liquid picture predict that

$$\alpha = \min(2/\nu - 1, 3). \quad (3)$$

In [4], an alternative theory was developed that was capable of treating compressible states near the $1/2$ filling. An expression for $\alpha(\nu)$ was obtained which, in the limit of vanishing compressibility, coincides with Eq. (3) for Jain filling factors. This theory predicts that the slope of the tunneling exponent $d\alpha/d\nu$ behaves discontinuously as a function of ν at points $\nu = 1$, $\nu = 1/2$.

Recent tunneling experiments [5] gave the following results:

(1) At low temperatures, the I – V characteristic exhibits power law behavior (1) up to several tens in current. The power law I – V characteristics are observed independently of whether the 2DEG is in a compressible or an incompressible state.

(2) The tunneling exponent α varies continuously with the filling factor ν . The dependence of the tunneling exponent on the filling factor is approximated well by the linear law $\alpha = 1/\nu$.

One can see that the second item is in obvious contradiction to the predictions of the chiral Luttinger liquid theory.

This disagreement puts in doubt the generally accepted theories of the fractional QH edge and needs to be explained either within these theories or by developing a new theoretical approach. That is why a lot of attention has been paid to the problem of late [6–11].

In the discussion below, we restrict ourselves to the incompressible case only. In this case, the QH edge is believed to be described by a chiral Luttinger liquid theory. In its standard form, this theory [1, 2] claims that there are several edge chiral Luttinger modes which can be separated into one charged mode and a number of neutral ones. The charged mode is described by a chiral bosonic field ϕ_0 , while the neutral modes are described by bosons ϕ_1, \dots, ϕ_N and can be both chiral (propagating along the same direction as the charged mode) and antichiral (counterpropagating). The dispersion of charged and neutral modes determines the velocities $s_j(q)$:

$$\omega_j(q) = s_j(q)q. \quad (4)$$

The anomalous exponent α in I – V characteristic (1) is simply related to the asymptotic behavior of the single-

¹ This article was submitted by the authors in English.

particle Green's function of an electron in the QH system [12]:

$$G(t) = -i\langle T\psi(x, t)\psi^\dagger(x, 0)\rangle \sim t^{-\alpha}. \quad (5)$$

An attempt to solve the contradiction between the theory and the experiment was made in [8, 9]. The main idea of these works is that the experimentally observed tunneling exponent is consistent with the chiral Luttinger liquid picture under the assumption that the neutral modes are nonpropagating (or their propagation velocities are negligible). In our opinion, the weakness of this approach is that its central assumption has no sufficient physical justification. In the experiment, the power law $I-V$ characteristic is observed in a broad (about two tens) voltage range. For the picture of [8, 9], it implies that the velocities of the neutral edge modes should differ from the velocity of the charged mode by a minimum of two orders of magnitude. This difference is attributed to the Coulomb interaction, whose contribution to the velocity of the charged mode is evidently larger than to the neutral ones. However, simple analysis shows that, while the neutral modes have linear dispersion (4) with s_j constant, the velocity of the charged mode s_0 has a logarithmic q -dependence (see [10] and considerations below)

$$\frac{s_0}{s_j} \sim \ln\left(\frac{1}{qa}\right), \quad (6)$$

where a is the quantum-well width. The logarithmic factor on the r.h.s of Eq. (6) evidently cannot account for the two-tens difference needed for the picture of [8, 9]. In a real experiment [5], tunneling occurred from a 3D metal contact separated by a $b \sim 100$ Å-thick barrier from the edge. Therefore, the Coulomb interaction must be screened at this distance and ratio (6) saturates at $q < b^{-1}$.

Equation (2) corresponds to the shakeup of the charge relaxation mode at the edge. If one neglects the contribution of other bosonic modes, the experimentally observed tunneling exponent will be regained. This is exactly the way the problem is treated in the framework of the independent boson model (IBM) [6, 11, 12], where a single localized electron electrostatically interacts with the hydrodynamic charged edge mode in the incompressible case [6] or with the bulk charge relaxation modes in the compressible case [11]. Although the IBM gives a correct tunneling exponent, it says nothing about the physical origin of the localized states and its relevance to the experiments is not clear unless the nature of these states is specified. In particular, the understanding of what these states are is important, since the results which can be obtained in the framework of the IBM are very sensitive to the choice of the energy position of the localized state.

In our opinion, the good agreement between the observed universality of the $I-V$ characteristics and the IBM description indicates that, near the edge of the QH liquid, there exist some low-energy electronic states

other than the excitations of the chiral Luttinger liquid. Electrons tunneling from the metal into these states electrostatically interact with the charged mode of the edge collective excitations. Below, we suggest a model of the edge where the tunneling current is transmitted in a two-step process which involves localized states in the bulk at the intermediate stage. We show that these processes give an experimentally observed $I-V$ exponent provided that the intermediate localized states are spatially separated from the edge and their energy distribution function decays exponentially in the gap of the incompressible states, as in the integer quantum Hall regime [13].

The series of well-established plateaus observed in the experiment [5] indicate that in the gaps of incompressible QH states there exists a finite density of bulk localized states $g(\epsilon)$ created by the random impurity potential. An electron may tunnel into the QH edge in a two-step process: first it tunnels into a localized state, where it may stay for some time t^* , and then decays into the edge mode due to a finite hybridization between the edge and bulk states. If the voltage V satisfies the condition

$$\hbar/eV \ll t^*$$

then the second step of the tunneling process does not affect the $I-V$ characteristics.

On the time scale t^* , the tunneling process is described by the IBM model. If the QH system is incompressible, the only contribution to the polarization of the QH medium comes from gapless edge modes. An electron can polarize both charged and neutral modes (because they carry multipole moments).

We first consider the contribution of the charged mode. The corresponding Hamiltonian reads

$$H = \sum_n (\epsilon_n - w_n) a_n^\dagger a_n + \frac{1}{2} \int dx dx' \rho(x) v(x-x') \rho(x'). \quad (7)$$

Here, a_n is the annihilation operator of an electron in the localized state with energy ϵ_n and wave function $\psi_n(\mathbf{r})$, $\rho(x)$ is the charge density operator of the edge plasmon, and $v(r) = e^2/\kappa r$ is the Coulomb potential with the dielectric constant κ . The term

$$w_n = \int dx \rho(x) U_n(x) \quad (8)$$

stands for the electrostatic interaction between the edge plasmon and the electron in the localized state. Here,

$$U_n(x) = \int d^2 \mathbf{r}' v(|\mathbf{r} - \mathbf{r}'|) |\psi_n(\mathbf{r}')|^2 \quad (9)$$

is the potential induced by the localized state at the edge $\mathbf{r} = (x, 0)$. The charge density operator ρ of the edge plasmon is given by

$$\rho = \sum_{q>0} i \sqrt{\frac{vq}{2\pi L}} (b_q e^{iqx} - b_q^\dagger e^{-iqx}),$$

where L is the length of the edge and b_q and b_q^\dagger satisfy the canonical commutation relations.

Hamiltonian (7) is diagonalized [12] by the canonical transformation to the new fermionic operators \bar{a}_n :

$$a_n = \bar{a}_n e^{-i\Phi_n} = \bar{a}_n T \exp\left(-i \int_{-\infty}^t dt' w_n(t')\right), \quad (10)$$

where $\rho(x, t)$ is the charge density operator in the interaction representation and T is the time ordering operator. Introducing the field ϕ , such that $\rho = v/2\pi\partial_x\phi$, and taking into account that in the interaction representation its dynamics are given by Eq. (4), we find that the operators Φ_n in Eq. (10) are given by

$$\Phi_n(t) = \frac{v}{2\pi s_0} \int dx U_n(x) \phi(x, t), \quad (11)$$

where the velocity of the charged mode reads

$$s_0 = \frac{e^2}{\kappa\pi\hbar} v \ln\left(\frac{1}{qa}\right). \quad (12)$$

Green's function (5) of an electron in the n th localized state is given by

$$G_n(t) = -ie^{i\tilde{\epsilon}_n t} (1 - n_F(\tilde{\epsilon})) \langle T e^{-i\Phi_n(t)} e^{i\Phi_n(0)} \rangle, \quad (13)$$

where $\tilde{\epsilon}_n$ is the exact energy of the localized eigenstate dressed by the charge mode relaxation.

The factor

$$\langle T e^{-i\Phi_n(t)} e^{i\Phi_n(0)} \rangle = \left\langle T e^{-i \int_0^t w(t')} \right\rangle \quad (14)$$

is responsible for suppression of the tunneling density of states due to the interaction of an electron with the charged mode. At large times, the main contribution to this factor comes from the long-wavelength limit. In our case, this limit is defined by $qd_n \ll 1$, where d_n is the distance from the edge to the localized state (below, it will be argued that $d_n > l$). The asymptotic form of this factor does not depend on n and is given by

$$\langle T e^{-i\Phi_n(t)} e^{i\Phi_n(0)} \rangle \sim t^{-1/\nu}.$$

In the standard approximation [12], where the dependence of the tunneling matrix element on the energy is neglected, we obtain

$$I(V) \sim \int_0^{eV} d\epsilon g(\mu + \epsilon) (eV - \epsilon)^{1/\nu},$$

where μ is the chemical potential of the QH system and $g(\epsilon)$ is the density of the localized states.

The tunneling exponent α is determined by the behavior of the density of localized states in the vicinity

of the Fermi energy. Since we are considering the incompressible QH liquid, the Fermi level must lie in the gap of the volume excitations. It looks very natural to assume that the density of localized states in the gap decays rapidly with energy (just as in the case of the integer QH effect). If the energy scale Γ of decay is smaller than eV , the tunneling current is given by

$$I(V) \sim \Gamma V^{1/\nu}$$

and $\alpha = 1/\nu$. In the opposite limiting case ($\Gamma > eV$), the tunneling current is given by $I \sim V^{1/\nu + 1}$.

We next discuss the interaction of a tunneling electron with the multipole moments of the neutral modes. This has an analogy with the model of a smooth edge considered in [14], where the tunneling exponent is much larger than $1/\nu$ due to the contribution of the modes carrying multipole moments.

The interaction with the mode responsible for the dipole moment is most important. In contrast to the case of the charged mode, this interaction depends on a particular model of the edge, especially, on the transversal structure of the neutral modes. We take this interaction into account phenomenologically. The model Hamiltonian describing the interaction of localized states with the neutral modes should have the same form as Eq. (7) with two distinctions. First, one should replace $v(|\mathbf{r} - \mathbf{r}'|)$ in Eq. (9) by the dipole interaction $\delta y \partial_x v(|\mathbf{r} - \mathbf{r}'|)$, where the quantity δy is of the order of the width of the edge strip and depends on a particular model of the edge. In what follows, we assume $\delta y \approx l$. The second distinction is that, in contrast to (12), the velocity of the dipole mode does not contain the Coulomb logarithm $s_1 \sim e^2 v / \kappa\pi\hbar$. Taking into account the dipole interaction in the framework of the IBM shows that factor (14) decreases more rapidly at large t :

$$\left\langle T \exp\left(-i \int_0^t w(t')\right) \right\rangle \sim t^{-[(1/\nu) + (l^2/d_n^2)(1/\nu)]}.$$

For the tunneling exponent at $\Gamma < eV$ we get

$$\alpha(d_n) = \frac{1}{\nu} + \frac{l^2}{d_n^2} \frac{1}{\nu}. \quad (15)$$

The tunneling probability decreases as $\exp(-d_n^2/l^2)$ with the tunneling distance, leading to a decrease in the tunneling current. On the other hand, the larger the value of d_n the smaller the value of $\alpha(d_n)$. This leads to I increasing with d_n at small values of the applied voltage. As a result, there exist optimum values of the tunneling distance $d_{opt} > l$ and of the tunneling exponent α_{opt} . The values of d_{opt} and α_{opt} can be determined using the following estimate of the tunneling current related to the n th localized state:

$$I_n(V) \sim e^{-d_n^2/l^2} \left(\frac{eV}{E_0}\right)^{\alpha(d_n)}.$$

Here, E_0 is a large energy ($E_0 \gg eV$), which is of the order of the Fermi energy. From this equation we easily get

$$\alpha_{opt} = v^{-1} \left(1 + \left(\frac{v}{\ln(E_0/eV)} \right)^{1/2} \right).$$

It can be seen that, at small voltages, the optimum tunneling exponent is close to the experimentally observed value $\alpha_{opt} \approx v^{-1}$.

We would like to emphasize that this result is related to the fact that the electron tunnels at a distance larger than the width of the edge strip l . On the contrary, in the model used in [14] it was implicitly assumed that $d_n \sim \delta y$, and the tunneling exponent was found to be much larger than $1/v$.

We conclude that the tunneling process, as a whole, looks as follows. First, the electron tunnels in the localized state and during the time d_{opt}/s_0 polarizes the charged mode. As a result, the positive screening charge e is attracted to the edge in the region of length d_{opt} and the compensating negative charge $-e$ is carried away by the charged mode with velocity s_0 . On time scale t such that $d_{opt}/s_0 < t < t^*$, there exists a dipole formed by the localized electron and the screening positive charge. After the time t^* , this dipole vanishes due to tunneling of the electron from the localized state into the edge.

The authors would like to thank J. Fröhlich for stimulating discussions. V.C. is grateful to B.I. Halperin for important remarks and hospitality at the Lyman Lab. We would like to thank L. Levitov and A. Chang for valuable comments and information about their work.

This work was supported by the Russian Foundation for Basic Research (project nos. 99-02-17093 and 99-02-17002), the INTAS (grant nos. 97-1342 and 99-1705), and the Program "Physics of Solid-State Nanostructures" (grant no. 1001).

REFERENCES

1. C. L. Kane, M. P. A. Fisher, and J. Polchinski, Phys. Rev. Lett. **72**, 4129 (1994); C. L. Kane and M. P. A. Fisher, Phys. Rev. B **51**, 13449 (1995).
2. X. G. Wen, Phys. Rev. B **41**, 12838 (1990); Phys. Rev. Lett. **64**, 2206 (1990); Phys. Rev. B **43**, 11025 (1991); *ibid.* **44**, 5708 (1991); Int. J. Mod. Phys. B **6**, 1711 (1992); X. G. Wen and A. Zee, Phys. Rev. B **46**, 2290 (1992).
3. J. Fröhlich and T. Kerler, Nucl. Phys. B **354**, 369 (1991).
4. A. V. Shytov, L. S. Levitov, and B. I. Halperin, Phys. Rev. Lett. **80**, 141 (1998).
5. M. Grayson, D. C. Tsui, L. N. Pfeiffer, *et al.*, Phys. Rev. Lett. **80**, 1062 (1998).
6. S. Conti and G. Vignale, cond-mat/9801318.
7. J. H. Han and D. J. Thouless, Phys. Rev. B **55**, 1926 (1997).
8. D. H. Lee and X. G. Wen, cond-mat/9809160.
9. A. López and E. Fradkin, cond-mat/9810168.
10. U. Zülicke and A. H. MacDonald, cond-mat/9802019.
11. D. V. Khveshchenko, cond-mat/9710137.
12. G. D. Mahan, *Many-Particle Physics* (Plenum, New York, 1981).
13. F. Wegner, Z. Phys. B **51**, 279 (1983).
14. S. Conti and G. Vignale, Phys. Rev. B **54**, R14309 (1996).

Critical Behavior of Frustrated Systems: Monte Carlo Simulations versus Renormalization Group¹

D. Loison*, A. I. Sokolov**, B. Delamotte***, S. A. Antonenko**,
K. D. Schotte*, and H. T. Diep****

* Institut für Theoretische Physik, Freie Universität Berlin, 14195 Berlin, Germany

** St. Petersburg Electrotechnical University, St. Petersburg, 197376 Russia

e-mail: ais@sokol.usr.etu.spb.ru

*** Université Paris 7, 75251 Paris Cedex 05, France

**** Université de Cergy-Pontoise, 95302 Cergy-Pontoise Cedex, France

Received August 28, 2000

We study the critical behavior of frustrated systems by means of the Padé–Borel resummed three-loop renormalization-group expansions and numerical Monte Carlo simulations. Amazingly, for six-component spins, where the transition is second-order, both approaches disagree. This unusual situation is analyzed both from the point of view of the convergence of the resummed series and from the possible relevance of nonperturbative effects. © 2000 MAIK “Nauka/Interperiodica”.

PACS numbers: 75.10.-b; 64.60.Ak; 64.60.Cn; 05.10.Ln

Frustrated spin systems have been very much studied in their classical and quantum aspects. In particular, the critical behavior of 3D stacked triangular antiferromagnets (STA) has deserved much attention [1–9] since, firstly, it has many physical realizations in rare-earth materials; secondly, it is an archetype for frustrated systems; and, thirdly, it is directly related to the behavior of its 2D zero-temperature quantum counterparts. The frustration in such systems comes from the fact that, for $N > 1$ component spins, the ground state is noncollinear and shows the famous 120° structure. It is thus natural to believe that if the transition is second-order, they belong to a new universality class. Our present understanding of these systems comes, as usual, from the renormalization group (RG) calculations, from Monte Carlo simulations, and from experiments. The most impressive fact is that more than twenty years after the first works devoted to their study, there is still no agreement between these approaches. For instance, a calculation made in $D = 4 - \epsilon$ [3] predicts no stable fixed point for N in the interval $N_{c2} = 2.202 - 0.569\epsilon + 0.989\epsilon^2 < N < N_{c3} = 21.80 - 23.43\epsilon + 7.088\epsilon^2$ and another, made in $D = 2 + \epsilon$, predicts a fixed point for any $N > 2$. Some experiments find a second-order phase transition, and others, a weak first-order transition. Moreover, the different approaches to finding a continuous transition do not find the same exponents, a fact that suggests that the theoretical or numerical approaches may miss some fundamental points (topological defects, breakdown of perturbation theory, etc.).

Our aim in this letter is to shed light on this problem. We rely on the fact that the three-loop RG calculations made in $D = 4 - \epsilon$ with $\epsilon = 1$ and directly in $D = 3$ find a critical value $N_c(D = 3)$ above which the transition is second-order and equal to 3.39 [3] and 3.91 [4], respectively. A very weak first-order transition is expected for $N = 3$ —a situation very difficult to test numerically. Therefore, instead of studying the physical ($N = 3$) spin system directly, we choose to study the following question: whether there is consensus between the results given by the RG approach based on the Landau–Wilson (ϕ^4 -like) model and those obtained by Monte Carlo simulations for the values of D and N , where a fixed point is found.

Note that the reliability of the RG approach for predicting 3D critical behaviors is not generic but has been demonstrated for simplest the universality classes such as $O(N)$. The discrepancy between the perturbative results around $D = 2$ and $D = 4$ is, in fact, common to a wide class of systems, among which there are the dipole-locked phase of ^3He , electroweak phase transition, smectic liquid crystal, etc. Our study is therefore likely to be relevant to a much wider class of systems than frustrated magnets.

To tackle our question, we study in $D = 3$ the largest possible N compatible with numerical possibilities, where the usual recipes should work, since in this case we are far above the line $N_c(D)$, the proximity of which could be the root of all the problems. Being, in principle, in the second-order region, we expect to compute accurately the critical exponents both numerically and from the resummed 3D RG expansions. The compari-

¹ This article was submitted by the authors in English.

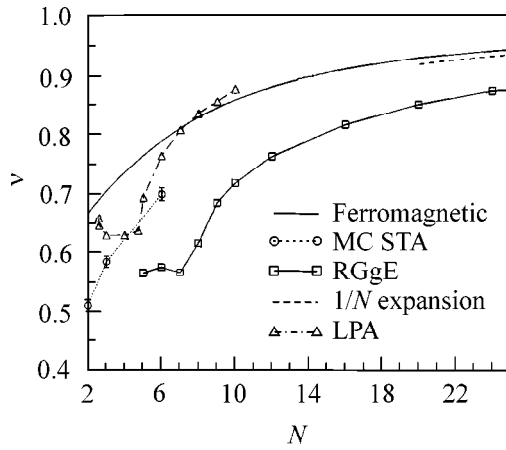


Fig. 1. The critical exponent ν for $N = 6$ calculated by the field-theoretical renormalization-group technique (RGgE), by Monte Carlo simulations (MC STA), and by some other methods (see text).

son between the results obtained by these two methods should be a test of the most powerful theoretical approaches in this nonferromagnetic case. We also choose the value of N such that the corresponding system does not show topological defects, in order to eliminate a possible reason for the breakdown of perturbation theory. It turns out that $N = 6$ is the ideal candidate. Below, we present numerical results for $N = 6$, as well as the analytical ones for various N , including $N = 6$, and compare them.

Renormalization group analysis. The relevant Landau–Wilson Hamiltonian reads [3, 16]

$$H = \frac{1}{2} \int d^3x \left[r_0^2 \phi_\alpha \phi_\alpha^* + \nabla \phi_\alpha \nabla \phi_\alpha^* + \frac{u_0}{2} \phi_\alpha \phi_\alpha^* \phi_\beta \phi_\beta^* + \frac{w_0}{2} \phi_\alpha \phi_\alpha^* \phi_\beta^* \phi_\beta^* \right]. \quad (1)$$

The domain of parameters of interest is $u_0 > 0$ and $w_0 > 0$. The calculations are based on the three-loop RG expansions obtained earlier for the more complicated 3D model with three quartic coupling constants [4]. The Padé–Borel resummation of the RG series is performed, and Pade approximants [3/1] and [2/1] are used for analytical extension of the Borel transforms for the β -functions and critical exponent γ , respectively. The

exponent η is evaluated by direct substitution of the fixed point coordinates into the corresponding expansion.

For $N > 7$, the fixed point, which controls the chiral critical behavior, is found to be a stable node; and for $N = 5, 6, 7$ it is a stable focus. The latter scenario looks quite new; i.e., it is observed for the first time in STA systems, while the former one was already discussed (see, e.g., [4]). The values of critical exponents γ and η obtained from the RG series are used to estimate other exponents via scaling relations. The results of our RG calculations are collected in Table 1 and presented, along with others, in Fig. 1 (RGgE). As is seen, critical exponents as functions of N demonstrate a cusp between $N = 7$ and $N = 8$, which reflects the above-mentioned change in the type of fixed point governing the critical behavior.

Monte Carlo results. We study six-component spins interacting via the Hamiltonian

$$H = \sum_{\langle ij \rangle} J_{ij} \mathbf{S}_i \mathbf{S}_j, \quad (2)$$

where the sum runs over all neighbors of the stacked triangular lattice (STA) and the interaction is chosen to be antiferromagnetic ($J > 0$). In the ground state, the spins are planar, with the three spins at the corners of each triangle forming a 120° structure. We use the standard Metropolis algorithm in combination with the overrelaxation algorithm [10]: one overrelaxation step per one Metropolis step. This reduces the correlation time and improves the statistics. For each size, we use several hundred thousand steps to equilibrate our system and up to five millions steps to thermalize for the larger sizes. We have repeated these simulations for different initial configurations (ordered or random) to make sure that our results do not depend on them. The histogram MC technique by Ferrenberg and Swendsen [11] is used to obtain thermodynamic quantities at T close to T_0 from a simulation done at T_0 . We have studied our system in the finite-size scaling (FSS) region [12], with the simulations done at $T_s = 0.463$. We consider $L^2(2L/3)$ systems, where $(L)^2$ is the size of the planes and $2L/3$ is the number of planes. To find the critical temperature T_c , we use Binder's cumulant, defined as $U = 1 - \langle M^4 \rangle / 3 \langle M^2 \rangle^2$, where the order parameter M is calculated by partitioning our lattice into three

Table 1

N	5	6	7	8	9	10	12	16	20	100
α	0.305	0.275	0.303	0.152	-0.055	-0.157	-0.292	-0.451	-0.553	-0.909
β	0.300	0.302	0.295	0.319	0.354	0.370	0.393	0.418	0.434	0.488
γ	1.095	1.121	1.108	1.211	1.348	1.417	1.506	1.616	1.685	1.935
ν	0.565	0.575	0.566	0.616	0.685	0.719	0.764	0.817	0.851	0.970
η	0.063	0.051	0.042	0.035	0.032	0.030	0.027	0.023	0.019	0.005

sublattices with only collinear spins and by summing each magnetization. We record the variation of U with T for various system sizes and then locate T_c at the intersection of these curves [13]. In Fig. 2, U is plotted as a function of the temperature for different sizes from $L = 12$ up to $L = 36$. Due to the presence of residual corrections to finite size scaling, one actually needs to extrapolate the results of this method for $(\ln b)^{-1} \rightarrow 0$. From these data, we extrapolate the value of T_c (not shown) and obtain $T_c = 0.4636(2)$, while the universal quantity U at T_c is $U^* = 0.6545(15)$. Then we calculate the critical exponents using a log–log fit [12, 14]. The estimate of $1/\nu$ is extracted from $V_1 = \langle ME \rangle / \langle M \rangle - \langle E \rangle$, $V_2 = \langle M^2 E \rangle / \langle M^2 \rangle - \langle E \rangle$ (Fig. 2), while the data for susceptibility $\chi = N \langle M^2 \rangle / k_B T$ and $\langle M \rangle$ (not shown) yield the values of γ/ν and β/ν , which are found to be $1.975(20)$ and $0.513(12)$, respectively. All errors are calculated with the help of the Jackknife procedure [15] and include the influence of the uncertainty in estimating T_c . The final results are summarized in Table 2, with η and α evaluated using scaling relations $\eta = 2 - \gamma/\nu$ and $\alpha = 2 - D\nu$. Note that, contrary to spins with $N = 2$ or $N = 3$, $\eta > 0$. This is due to the fact that, for $N = 6$, the RG flow is attracted by a true stable fixed point and not by a local minimum [6, 8, 9].

Discussion. The predictions of the RG analysis for six-component spins listed in Table 1 do not agree with the Monte Carlo results given in Table 2. The general situation is illustrated by Fig. 1, where our MC and RG results for ν , along with those given by the Local Potential Approximation (LPA) [6] and the $1/N$ expansion [16], are presented; the six-loop RG estimates for the ferromagnetic case [17] are also plotted for comparison.

Since our numerical results are well converged, it seems unlikely that a Monte Carlo study of much larger systems would resolve the discrepancy with the RG predictions. To clear up the origin of this discrepancy, we analyze the structure of the RG series employed. Of prime importance is the vicinity of the chiral fixed point for $N = 5, 6, 7$, when this point is a focus. Contrary to the (unstable) fixed point governing the $O(N)$ -symmetric behavior, the chiral point lies very close to the w axis, being far from the u axis. For the case $N = 6$ of interest, its coordinates are $u^* = 0.0665$ and $w^* = 1.6025$. In this region, the structure of the series of β -functions turns out to be unexpectedly irregular. As an example, we present here two ‘‘cuts’’ of the Borel-transformed expansion for $\beta_u(u, w)$ running through the chiral fixed point, which clearly demonstrate this irregularity:

$$\beta_u^B(u, 1.6025) = -0.3607 + 0.7774u - 0.5004u^2 + 0.0339u^3 - 0.0055u^4, \quad (3)$$

$$\beta_u^B(0.0665, w) = 0.0643 - 0.0132w - 0.1960w^2 + 0.0346w^3 + 0.0010w^4. \quad (4)$$

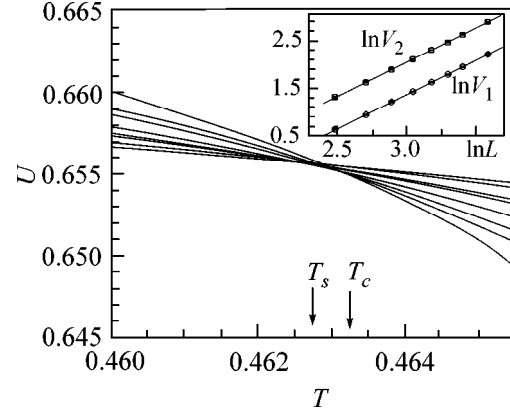


Fig. 2. Binder’s parameter U as a function of the temperature for different sizes L (in the left part of the figure from bottom to top $L = 12, 15, 18, 21, 24, 27, 30, 36$). The arrows show the estimated critical temperature T_c and the temperature of our simulations T_s . In the inset, the values of V_1 and V_2 are shown as functions of L in the \ln – \ln scale at T_c . The value of the slopes gives $1/\nu$, and we obtain $\nu = 0.698(12)$ for V_1 and $0.702(13)$ for V_2 . The smallest size ($L = 12$) is not included in our fits.

The coefficients in Eqs. (3) and (4) do not decrease monotonically with an increase in their numbers, and expansion (4) has coefficients with irregular signs. Hence, the RG series for β -functions would not demonstrate a good summability near the chiral fixed point and are hardly believed to yield precise numerical results. Moreover, the Padé–Borel approximant for β_u , taken at the chiral fixed point, as a function of the Borel variable t , has a pole at $t = 61.8$, which is not dangerous in practice but reflects the poor summability of the series. The difference between numerical results obtained within the RG and MC approaches may be caused by an unfavorable structure of the RG expansions. On the other hand, for all N , the chiral fixed point coordinate u^* given by our series remains positive, preventing the RG expansions from losing Borel summability in the domain of interest. Hence, here we do not face this problem, as occurs when systems with quenched disorder are studied [18]. This keeps calculations of the higher order contributions to the RG functions meaningful and desirable.

Can an account for higher order terms in the RG expansions significantly improve the situation? In principle, yes. Indeed, the true chiral fixed point location may differ substantially from that given by the three-loop approximation and lie in the domain of the RG flow diagram, where the series for β -functions can be properly resummed. The higher order terms may shift

Table 2

N	α	β	γ	ν	η
6	-0.100(33)	0.359(14)	1.383(36)	0.700(11)	0.025(20)

the calculated fixed point coordinates to their exact values, thus making the RG series better summable at criticality. To clear up whether such a situation really takes place, higher order RG calculations have to be performed.

Up to now, there is only a single different theoretical approach that allows quantitative calculations for $D = 3$: the LPA method based on a truncation of the Wilson RG equations. Even when missing the field renormalization, this method is nonperturbative, since it is not based on a weak-coupling expansion. However, although in our case the results obtained within the LPA are closer to the MC data than their RG analogues, they show an unexpected dependence of v on N at small N . Moreover, used around $D = 2$, this approach contradicts the perturbative results obtained from the Nonlinear Sigma ($NL\sigma$) model, which are, in this dimension, well confirmed by simulations [19]. They are, in any case, not accurate enough to draw a conclusion in $D = 3$. Since the LPA is known to be the first order of a systematic derivative expansion, it is desirable that the next order be computed.

Let us now remark that, even if the 3D physics is well reproduced by our analysis, a coherent picture of frustrated system behavior would still require one to understand the discrepancy between the $NL\sigma$ model approach and the Landau–Wilson one. A striking difference between both approaches is that near $D = 2$ the low-temperature expansion of the $NL\sigma$ model predicts that a new “current” term of the form $(\phi^* \nabla \phi)^2$ is relevant [2]. This term appears to be fundamental, since for $N = 3$, it allows one to find a fixed point with an $O(4)$ symmetry. Being highly nonrenormalizable near $D = 4$, it is irrelevant and forgotten. There is thus a scenario other than the numerical unreliability of the three-loop RG approximation; namely, the Landau–Wilson Hamiltonian (1) is incomplete in 3D. As was suggested for the Abelian Higgs transition, this could be interpreted as the necessity to have recourse to the $NL\sigma$ model description, abandoning that of the Landau–Wilson model. Note, however, that it is very doubtful that the analysis made around $D = 2$ can be extended straightforwardly for any N up to $D = 3$, since i) for 3-component spins, the $O(4)$ fixed point found for $D = 2 + \epsilon$ was shown to disappear in a nontrivial dimension strictly smaller than three in a closely related principal chiral model [20] and ii) an $O(4)$ behavior was seen neither experimentally nor numerically for $N = 3$ and $D = 3$. Thus, the perturbative analysis of the $NL\sigma$ model also fails for $D > 2$. However, it remains that a coherent picture of the behavior of frustrated systems for all N and D should include the results of the $NL\sigma$ model and therefore explain why and when the current term starts to be relevant as a function of N and D . If this happens to be around $D = 3$ for $N \sim O(1)$, it could perturb the RG results presented above and explain why otherwise

powerful methods do not work properly here. In any case, we believe that our results for $N = 6$ constitute a clear challenge to the theoretical approaches, which is perhaps not out of reach from higher order RG calculations and improvement of the LPA method.

This work was supported in part by the Alexander von Humboldt Foundation (D.L.), the International Science Foundation (A.I.S., grant no. p99-943), and the Ministry of Education of Russian Federation (A.I.S., grant no. 97-14.2-16). B. Delamotte and D. Loison are grateful to G. Zumbach for discussions.

REFERENCES

1. *Magnetic Systems with Competing Interactions (Frustrated Spin Systems)*, Ed. by H. T. Diep (World Scientific, Singapore, 1994).
2. P. Azaria, B. Delamotte, F. Delduc, and Th. Jolicoeur, *Nucl. Phys. B* **408**, 585 (1993).
3. S. A. Antonenko, A. I. Sokolov, and V. B. Varnashev, *Phys. Lett. A* **208**, 161 (1995).
4. S. A. Antonenko and A. I. Sokolov, *Phys. Rev. B* **49**, 15901 (1994).
5. M. F. Collins and O. A. Petrenko, *Can. J. Phys.* **75**, 605 (1997).
6. G. Zumbach, *Phys. Rev. Lett.* **71**, 2421 (1993); *Nucl. Phys. B* **413**, 771 (1994).
7. H. Kawamura, *J. Phys.: Condens. Matter* **10**, 4707 (1998).
8. D. Loison and K. D. Schotte, *Eur. Phys. J. B* **5**, 735 (1998).
9. D. Loison and K. D. Schotte, *Eur. Phys. J. B* **14**, 125 (2000).
10. M. Creutz, *Phys. Rev. D* **36**, 515 (1987).
11. A. M. Ferrenberg and R. H. Swendsen, *Phys. Rev. Lett.* **61**, 2635 (1988); **63**, 1195 (1989).
12. N. Barber, in *Phase Transition and Critical Phenomena*, Ed. by C. Domb and J. L. Lebowitz (Academic, New York, 1983), Vol. 8.
13. K. Binder, *Z. Phys. B* **43**, 119 (1981).
14. A. M. Ferrenberg and D. P. Landau, *Phys. Rev. B* **44**, 5081 (1991).
15. B. Efron, *The Jackknife, the Bootstrap and Other Resampling Plans* (SIAM, Philadelphia, 1982).
16. H. Kawamura, *Phys. Rev. B* **38**, 4916 (1988); **42**, 2610 (1990).
17. S. A. Antonenko and A. I. Sokolov, *Phys. Rev. E* **51**, 1894 (1995).
18. A. J. Bray, T. McCarthy, M. A. Moore, *et al.*, *Phys. Rev. B* **36**, 2212 (1987); A. J. McKane, *Phys. Rev. B* **49**, 12003 (1994); B. N. Shalaev, S. A. Antonenko, and A. I. Sokolov, *Phys. Lett. A* **230**, 105 (1997).
19. B. W. Southern and A. P. Young, *Phys. Rev. B* **48**, 13 170 (1993).
20. M. Tissier, D. Mouhanna, and B. Delamotte, *Phys. Rev. B* **61**, 15 327 (2000).

Remarks about the Effective Conductivity of Some Three-Color Tessellations in the Plane¹

I. M. Khalatnikov^{1,2,3} and A. Yu. Kamenshchik^{1,2}

¹ Landau Institute for Theoretical Physics, Russian Academy of Sciences, ul. Kosygina 2, Moscow, 117334 Russia

² Landau Network–Centro Volta, 22100 Como, Italy

³ Tel Aviv University, Raymond and Sackler Faculty of Exact Sciences, School of Physics and Astronomy, 69978 Ramat Aviv, Israel

Received August 15, 2000

The asymptotic formula for the effective conductivity of isotropic three-color (three-conductivity) rhombic tessellation in the plane is obtained for the case when one conductivity is much smaller than the other two. The tentative formula for this rhombic tessellation is suggested and discussed. © 2000 MAIK “Nauka/Interperiodica”.

PACS numbers: 72.80.Tm

In spite of the fact that the history of studying the effective conductivity of composite materials is long enough [1], the number of exact mathematical results in this field is rather restricted. From these results, the most important is the duality relation for the effective conductivity of a plane covered by pieces of a medium with different conductivities. This relation was obtained in the seminal paper by Keller [2] and then rederived by Dykhne [3] for the random equal-weighted distribution. Mendelson [4] analyzed the applicability of this relation to the three-color non-equal-weighted structures. For the general isotropic structure of plane tessellation or for an anisotropic structure possessing the main axes, this relation can be written as follows:

$$\sigma_{xx}(\sigma_1, \sigma_2, \dots)\sigma_{yy}(\tilde{\sigma}^2/\sigma_1, \tilde{\sigma}^2/\sigma_2, \dots) = \tilde{\sigma}^2, \quad (1)$$

where $\tilde{\sigma}$ is the arbitrary number of the corresponding dimensionality. Let us stress that Eq. (1) is also true for non-equal-weighted distributions of conductivities. For two-color isotropic equal-weighted structures, the well-known formula $\sigma = \sqrt{\sigma_1\sigma_2}$ immediately follows from the general duality relation (1). For the analogous problem with three colors, one can see that when $\sigma_3 = \sqrt{\sigma_1\sigma_2}$, we immediately get that effective conductivity is equal to σ_3 [3]. Unfortunately, it is of little use for the construction of general formulas for three-color tessellations.

Notice also that the duality relation for three-color isotropic tessellations contains information about the first and second partial derivatives of the effective conductivity with respect to the partial conductivities. Making calculations in the vicinity of the point where

all partial conductivities are equal (for convenience, we choose them to be equal to 1), one can find that

$$\frac{\partial\sigma}{\partial\sigma_i} = 1/3, \quad (2)$$

$$\partial^2\sigma/\partial\sigma_i\partial\sigma_i = -2/9, \quad (3)$$

$$\partial^2\sigma/\partial\sigma_i\partial\sigma_k = 1/9, \quad i \neq k. \quad (4)$$

It is not surprising, because in the first two orders of perturbation theory, the structure is not essential and manifests itself beginning with third order.

In this letter, we would like to investigate some properties of regular three-color (i.e., three-conductivity) structures on the plane. For convenience, we reproduce here the table of the so-called Dirichlet tessellations in the plane [5] (see Fig. 1). From these tessellations, one can get the most interesting equal-weighted three-color structures on the plane.

Besides the exact formulas and relations described above, asymptotic relations which can be obtained for the cases when the conductivity of one component is much smaller than of the others have an important value. Important relations of this kind were obtained by Keller [6]. The key element of this consideration is the calculation of effective conductivity for the corner, which consists of four sectors. A medium with high conductivity σ_a occupies the sector $-\alpha/2 < \theta < \alpha/2$ and the opposite sector, while the two other sectors contain a medium with a very low conductivity σ_b . For such a corner, one has the following formula for the effective conductivity [6]:

$$\sigma(\alpha) \sim (\alpha\sigma_a\sigma_b/(\pi - \alpha))^{1/2}, \quad \text{for } \sigma_a/\sigma_b \gg 1. \quad (5)$$

¹ This article was submitted by the authors in English.

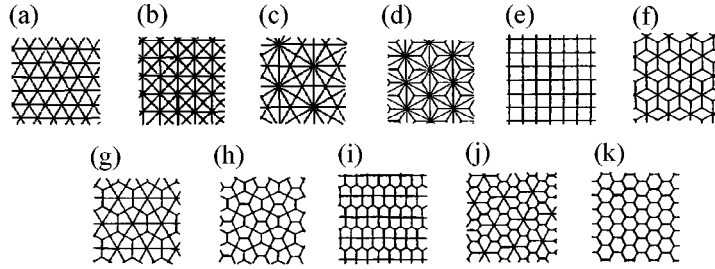


Fig. 1. Eleven topological types of isohedral face-to-face tessellations in the E^2 plane. Notice that the honeycomb structure (k) is the parent and all others can be obtained from it by the contraction of edges or polygons.

This formula was used in paper [6] for the investigation of the effective conductivity of the checkerboard covered by parallelograms and also for the generalization of the asymptotic formulas for two-color three-dimensional parallelepipedal structures studied before in [7].

Here, following the scheme elaborated in [6], we will consider a corner with six alternating sectors (each equal to $\pi/3$), three of which have a very high conductivity, while the others have a very low one. Looking at Fig. 2, it is easy to see that this structure is the basic one for three-color tessellation in the plane by rhombs (see also Fig. 1f).

Thus, we will consider circle of radius 1, where the regions of high conductivity σ_1 occupy the sectors $-\pi/6 < \theta < \pi/6$, $\pi/2 < \theta < 5\pi/6$, and $-5\pi/6 < \theta < -\pi/2$ (see Fig. 3). Orienting the electric field along the axis $\theta = 0$ from left to right, we see that the current flows from the last two sectors to the first one. It is convenient to choose the boundary conditions in the following way: the potential φ on the circumference ($\rho = 1$) is equal to +1 at $-\pi/6 < \theta < \pi/6$ and is equal to -1 at $\pi/2 < \theta < 5\pi/6$ and $-5\pi/6 < \theta < -\pi/2$. Then, an effective con-

ductivity of the corner could be written as

$$2\sigma = \int_{-\pi/6}^{\pi/6} \sigma_a \frac{\partial \varphi}{\partial \rho}(\rho, \theta)|_{\rho=1} d\theta = \sigma_a \int_{-\pi/6}^{\pi/6} \varphi_\rho(1, \theta) d\theta \quad (6)$$

or

$$\sigma = \sigma_a \int_0^{\pi/6} \varphi_\rho(1, \theta) d\theta. \quad (7)$$

We will look for a solution of the Laplace equation for φ satisfying the following boundary conditions:

$$\varphi(1, \theta) = 1, \quad 0 < \theta < \pi/6, \quad (8)$$

$$\varphi_\rho(1, \theta) = 0, \quad \pi/6 < \theta < \pi/2, \quad (9)$$

$$\varphi_\theta(\rho, 0) = 0, \quad (10)$$

$$\varphi\left(\rho, \frac{\pi}{6}-\right) = \varphi\left(\rho, \frac{\pi}{6}+\right), \quad (11)$$

$$\varphi\left(\rho, \frac{\pi}{3}\right) = 0, \quad (12)$$

$$\sigma_a \varphi_\theta\left(\rho, \frac{\pi}{6}-\right) = \sigma_b \varphi_\theta\left(\rho, \frac{\pi}{6}+\right). \quad (13)$$

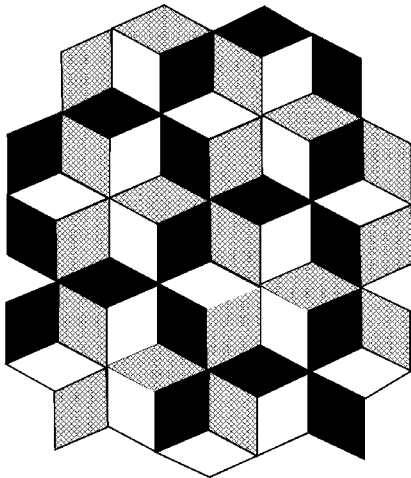


Fig. 2. Three-color rhombic tessellation of the plane.

Here, Eq. (9) reflects the quasi-insulator nature of the second medium, Eq. (10) reflects the symmetry of the current about the axis $\theta = 0$, Eq. (11) reflects the continuity of the potential on the boundary between two mediums, and Eq. (13) describes the continuity of the current through this boundary. Equation (12) reflects the fact that, due to the symmetry of the problem, the line of vanishing potential is $\theta = \pi/3$. (Notice that in the original problem with a four-sector corner such a line was located at $\theta = \pi/2$ [6]).

We will look for a solution of the Laplace equation in the following form:

$$\varphi = A_a \rho^v \cos v\theta, \quad 0 < \theta < \frac{\pi}{6} \quad (14)$$

and

$$\varphi = A_b \rho^v \sin v(\pi/3 - \theta), \quad \pi/6 < \theta < \pi/3. \quad (15)$$

Substituting Eqs. (14) and (15) into Eqs. (11) and (13), one has

$$A_a \cos \frac{v\pi}{6} = A_b \sin \frac{v\pi}{6} \quad (16)$$

and

$$A_a \sigma_a \sin \frac{v\pi}{6} = A_b \sigma_b \cos \frac{v\pi}{6}. \quad (17)$$

Equations (16) and (17) imply

$$\tan \frac{v\pi}{6} = \sqrt{\frac{\sigma_b}{\sigma_a}}. \quad (18)$$

Taking into account that $\sigma_b \ll \sigma_a$, one can easily get

$$v \approx \frac{6}{\pi} \sqrt{\frac{\sigma_b}{\sigma_a}}. \quad (19)$$

Now, using the smallness of v , one can obtain from Eq. (8)

$$A_a \approx 1. \quad (20)$$

Now, using Eq. (7), it is easy to get

$$\sigma = \sqrt{\sigma_a \sigma_b}. \quad (21)$$

Now, we are in a position to apply the obtained Eq. (21) to a regular isotropic structure with rhombi (see Fig. 2). It is easy to see that, if one of the colors corresponds to the vanishing conductivity, such a structure will not conduct, because this color constitutes "traps." One can represent the total rhombic tessellation as a covering of the plane by identical hexagons, each of which represents a plaquette consisting of alternating grey and black rhombi surrounded by isolating white triangles (see Fig. 4).

Now, suggesting that white-colored regions have a small conductivity $\sigma_1 \ll \sigma_2$ and $\sigma_1 \ll \sigma_3$, we see that the flow of current between plaquettes of the type represented in Fig. 4 is realized through two corners of the type represented in Fig. 3. Now, using simple considerations for the network of plaquettes and Eq. (21) for the corners, one can get an asymptotic formula for the effective conductivity of rhombic tessellation:

$$\sigma_{\text{asympt}} = \sqrt{\sigma_1 \sigma_2} + \sqrt{\sigma_1 \sigma_3}. \quad (22)$$

Similar considerations for the case when $\sigma_1 = \sigma_2 \ll \sigma_3$ give

$$\sigma_{\text{asympt}} = \frac{1}{2} \sqrt{\sigma_1 \sigma_3}. \quad (23)$$

A similar result was also obtained by A.M. Dykhne (private communication).

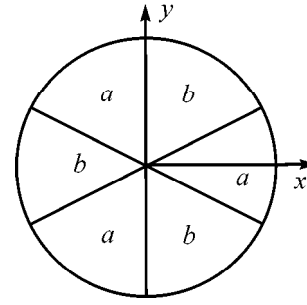


Fig. 3. Basic corner for the rhombic tessellation.

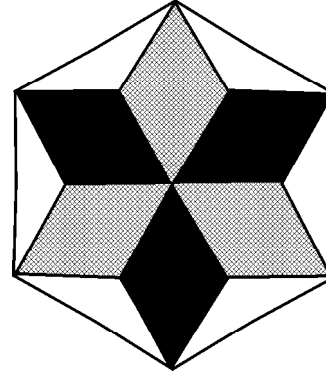


Fig. 4. Basic plaquette for the rhombic tessellation.

Thus, we have an asymptotic formula for rhombic tessellation in the case where there is a great contrast between the conductivities. On the other hand, from our preceding work [8], one can understand that, for a plane covered by isotropic equal-weighted covering of the plane by N colors, the conductivities of which can be written in the form

$$\sigma = 1 + \alpha, \quad \langle \alpha \rangle = 0, \quad (24)$$

where α is some small function on the plane (small contrast), the effective conductivity is²

$$\sigma_{\text{eff}} = 1 - \frac{1}{N} \langle \alpha^2 \rangle + \dots \quad (25)$$

Now we can try to construct the tentative formula for the rhomb tessellation which is self-dual, asymptotically true for the case of large contrast, and true for the case of small contrast up to the second order of perturbation theory:

$$\sigma_{\text{rhomb}} = \frac{\sqrt{\sigma_1} + \sqrt{\sigma_2} + \sqrt{\sigma_3}}{\frac{1}{\sqrt{\sigma_1}} + \frac{1}{\sqrt{\sigma_2}} + \frac{1}{\sqrt{\sigma_3}}}. \quad (26)$$

² Notice that for the multidimensional two-color checkerboard we have the same formula, where N is the dimensionality of space.

Naturally, this formula is only a hypothetical one. However, the check of its validity in the next perturbative approximation [8] can give it more solid grounds.

In the paper [9], the authors, using self-duality and symmetry of the isotropic three-color equal-weighted tessellations in the plane, have suggested that effective conductivities of such tessellations can be described by the cubic equation which represents the simple generalization of the well-known Bruggeman effective medium equation [10]:

$$\begin{aligned} & \sigma^3 + A\sigma^2(\sigma_1 + \sigma_2 + \sigma_3) \\ & - A\sigma(\sigma_1\sigma_2 + \sigma_1\sigma_3 + \sigma_2\sigma_3) - \sigma_1\sigma_2\sigma_3 = 0. \end{aligned} \quad (27)$$

In the Bruggeman equation, $A = 1/3$. The authors have suggested that in this hypothetical equation the constant A is correlated with the geometrical structures. Simple application of this equation to the rhomb tessellation shows that for the case of $\sigma_1 = 0$, the general conductivity is equal to zero and A should be equal to zero. Hence, $\sigma = (\sigma_1\sigma_2\sigma_3)^{1/3}$ for any set of values of $\sigma_1, \sigma_2, \sigma_3$, which obviously contradicts asymptotic result (22), obtained above (square roots instead of cube roots!). Thus, the suggested cubic equation is not universal and is not applicable to the rhomb structure. The source of this mistake lies in the suggestion of the authors [9] that self-duality and symmetry are enough for the resolution of the three-color problem. However, it is not true and it is well known from the theory of exactly solvable statistical models.³ Even in the frame of cubic equations the idea that A is a constant selects only one from an infinite set of possibilities, because it is easy to see that A can be an arbitrary function of self-dual combination of three conductivities. In such a way, the cubic equation with the constant A is not a general equation for symmetric isotropic structures.

³ A. B. Zamolodchikov, V. L. Pokrovsky, private communication.

In conclusion, we would like to make one comment regarding another three-color isotropic structure, a honeycomb structure consisting of hexagons of three colors (see Fig. 11). For such a structure, the numerical simulation was carried out in [9] and the approximate value of the parameter A was found. However, it is obvious that the numerical simulation cannot give proof of the validity of equation. A plausible check of the formulas for effective conductivity could be perturbative calculations, which should be done to at least the sixth order [8].

This work was supported in part by the Russian Foundation for Basic Research, project no. 99-02-18409.

The work of A.K. was also supported by CARIPLO Scientific Foundation. We are grateful to J.B. Keller, who attracted our attention to his paper [6]. We thank A.M. Dykhne for useful discussions.

REFERENCES

1. Lord Rayleigh, *Philos. Mag.*, Ser. 5, **34**, 481 (1892).
2. J. B. Keller, *J. Math. Phys.* **5**, 548 (1964).
3. A. M. Dykhne, *Zh. Éksp. Teor. Fiz.* **59**, 110 (1970) [*Sov. Phys. JETP* **32**, 63 (1970)].
4. K. S. Mendelson, *J. Appl. Phys.* **46**, 917 (1975); **46**, 4740 (1975).
5. P. Engel, *Geometric Crystallography: An Axiomatic Introduction to Crystallography* (Kluwer, Dordrecht, 1986).
6. J. B. Keller, *J. Math. Phys.* **28**, 2516 (1987).
7. M. Söderberg and G. Grimvall, *J. Phys. C* **16**, 1085 (1983).
8. I. M. Khalatnikov and A. Yu. Kamenshchik, *cond-mat/0008012*.
9. L. G. Fel, V. Sh. Machavariani, and D. J. Bergman, *cond-mat/0007022*.
10. D. A. G. Bruggeman, *Ann. Phys. (Leipzig)* **24**, 636 (1935).

Erratum: “High-Efficiency Zn Isotope Separation in a Photochemical Reaction Induced by Two-Photon Excitation” [*JETP Lett.* 71, 12, 481]

P. A. Bokhan, V. V. Buchanov, D. É. Zakrevskii, A. Yu. Stepanov, and N. V. Fateev

PACS numbers: 47.27.Ak; 99.10.+g

In this paper, the caption to Fig. 2 should be the following:

Fig. 2. Luminescence spectrum at a wavelength of 1.3 μm as a function of $\delta\nu_2$ for $\delta\nu_1 = 5$ GHz: (a) $E_1, E_2 = 150 \mu\text{J cm}^{-2}$ and $n = 1.6 \times 10^{13} \text{ cm}^{-3}$; (b) $E_1, E_2 = 150 \mu\text{J cm}^{-2}$ and $n = 2.4 \times 10^{14} \text{ cm}^{-3}$; (c) $E_1, E_2 = 400 \mu\text{J cm}^{-2}$ and $n = 1.6 \times 10^{13} \text{ cm}^{-3}$; and (d) $E_1, E_2 = 550 \mu\text{J cm}^{-2}$ and $n = 1.6 \times 10^{13} \text{ cm}^{-3}$.